

Towards a high-resolution nano desorption electrospray ionization source for mass spectrometry imaging of organoids

Jon Erlend Haavaag

Bioanalytical chemistry
60 credits

Department of chemistry
Faculty of Mathematics and Natural Sciences



Jon Erlend Haavaag

*Towards a high-resolution
nano desorption electrospray
ionization source for mass
spectrometry imaging of
organoids*

© Jon Erlend Haavaag

2023

Towards a high-resolution nano desorption electrospray ionization source for mass spectrometry imaging of organoids

Jon Erlend Haavaag

<http://www.duo.uio.no/>

Print: University of Oslo

IV

Preface

When arriving at the Institute of Chemistry, University of Oslo, my professor Steven Ray Wilson asked me what characteristics I preferred for my upcoming master's project. I view chemistry as a broad scientific field, which includes many different aspects. My answer was I wanted a technical project that would involve tinkering and exploring of machinery and the hardware that makes instruments used in chemical analysis work. My wish was granted.

The journey I would embark on took me down a path of diligent and persistent as well as patient work, and I am proud of what I have achieved. However, it is in such situations of long-lasting and continual endeavors where one discovers one's shortcomings. Therefore, I must give thanks to the people who have aided me during the past two years.

Firstly, my supervisors. Associate professor Hanne Røberg-Larsen, Professor Steven Ray Wilson, and MSc Stian Kogler are exemplary in their capacity to show up and bring productive feedback on short notice. I am also thankful towards the BACH group as a whole for carrying a culture of friendliness and compassion. This project is part of an interdisciplinary initiative called ITOM, to whom I also must give thanks for the opportunity to participate and for the funding.

Principal engineer Inge Mikalsen also deserves my utmost gratitude. His abilities to find solutions to technical and practical problems and work ethics is inspiring. Other staff that deserves a mention are Professor Ola Nilsen, and senior engineer Terje Grønås.

University is also a place for social relationships and new acquaintances. Marius Bull Tuner Inga Mork Aune, Eva Kvalvik, Gustav Mathingsdal Pedersen, Silje Solevåg, Sander Guttorm, Lise Midtøy and others have my appreciation, and have made my everyday study life a fun and meaningful experience. My family, roommates, friends, and church community have also stood by me with loving moral support and for that I am grateful.

Never have I in my life worked towards one and the same goal for a period of 18 months, but this thesis is a result of such an effort. The personal skills and habits I have developed I will preserve and administer the best I can. And, as a higher purpose, I am excited to see how these abilities will be used for God's glory in the future.

Abstract

Imaging is a relatively new way of analyzing cell samples. It can not only identify and quantify the biological molecules they contain, but also reveal their spatial localization within tissues. By analyzing different cell types, differences or similarities in spatial molecular composition can be discovered and used to infer useful information about the cells or cellular models used to mimic them. The goal of this thesis was to build an imaging platform to analyze cellular models, with a goal of further organoid development for use in, e.g., disease development and drug responses research.

An ion source capable of systematically desorbing analytes from a cell sample surface was built. Proof of function for the system was established by successfully desorbing analyte standards deposited on a sample holder. The holder was moved in all three directions using electrical motors to sample from different locations. The ion source consisted of a probe system delivering solvent that desorbed analytes from the surface before the solution was subsequently picked up and delivered to the mass spectrometer. The desorbed analytes were then detected, and a mass spectrum was acquired confirming detection of the wanted analytes. The system was however not successful in desorbing analytes from cell samples.

In this type of imaging, micrometer scale emitters are important for precise and accurate desorption of analytes from a small area of sample, leading to more confident localization. Nano electrospray ionization (nano-ESI) emitters were made using an in-house developed technique involving etching with hydrofluoric acid and atomic layer deposition for solvent delivery and desorption. These emitters were compared against a commercial ESI source and confirmed functional in detecting analytes. Their signal stability was however varying.

To summarize, a functional ion source capable of desorbing analyte standards was built, confirming proof of function for the system. In-house made capillary emitters were successfully implemented and shown to work. The system has yet to be automatized and to successfully desorb analytes from cellular samples. This should be the focus for further work.

Abbreviations

3D	Three dimensional
AdSC	Adult stem cells
AGC	Automatic gain control
ALD	Atomic layer deposition
CRM	Charged residue model
DC	Direct current
DESI	Desorption electrospray ionization
DNA	Deoxyribonucleic acid
ESC	Embryonic stem cells
ESI	Electrospray ionization
HESI	Heated electrospray ionization
HF	Hydrofluoric acid
HRMS	High-resolution mass spectrometry
HSC	Hepatic stellate cells
ID	Inner diameter
IEM	Ion evaporation model
iPSC	Induced pluripotent stem cells
LAESI	Laser ablation electrospray ionization
LC-MS	Liquid chromatography mass spectrometry
LDIDD	Laser ablation/ionization droplet delivery

MALDI	Matrix assisted laser desorption ionization
MDa	Mega Dalton
MS	Mass spectrometry
MSCH	Microcephaly
NCE	Nanospray capillary emitter
OD	Outer diameter
PC	Phosphatidylcholine
PCE	Primary capillary emitter
PEEK	Polyether ether ketone
PG	Phosphatidylglycerol
Ppm	Parts per million
Q	Quadrupole
QqQ	Triple quadrupole
R	(Mass spectrometric) resolution
RA	Retinoic acid
RDX	Royal demolition explosive
RNA	Ribonucleic acid
SFM	Shear force microscopy
SFP	Shear force probe
SIMS	Secondary ion mass spectrometry
TCA	Tricarboxylic acid cycle

TGF- β	Transforming growth factor beta
TIC	Total ion chromatogram
TNT	Trinitrotoluene
UiO	University of Oslo
UV-VIS	Ultraviolet-visible spectroscopy

Table of contents

1	Introduction	1
1.1	Bioanalysis: an essential and versatile branch of science in unlocking biological secrets	1
1.1.1	Bioanalytical method development is done to make sure optimal results are obtained.....	2
1.1.2	Human biological systems can be studied using model organisms	3
1.1.3	Organoids are an up-and-coming model organism	4
1.2	Mass spectrometry	4
1.2.1	Orbitrap mass analyzer: a high-resolution mass analyzer	6
1.2.2	Resolution and mass accuracy are central parameters used in mass spectrometric analysis.....	7
1.2.3	The properties of a high-resolution mass spectrometer and its impact on mass spectrometric imaging	8
1.2.4	Total ion chromatogram variation and automatic gain control are parameters to ensure stable acquisitions	9
1.3	Electrospray ionization offers effective ionization and sensitive analysis	9
1.3.1	Several models explain the course of events in electrospray ionization	10
1.3.2	Electrospray ionization has a vast area of use in many types of sciences.....	12
1.4	Desorption electrospray ionization, a close relative of electrospray ionization	13
1.5	Nano desorption electrospray ionization: its buildup and working principles	15
1.5.1	Nano desorption electrospray ionization is used for mass spectrometry imaging	16
1.5.2	Parameters characterizing high-quality emitters	20
1.5.3	A summarization of the important components of a nano desorption electrospray ionization platform	20
1.5.4	Comparing imaging using nano desorption electrospray ionization to other ionization methods	21
1.5.5	Analysis of cells using nano desorption electrospray ionization imaging is a productive step towards further model development	22
1.6	Production of capillary emitters for nano desorption electrospray ionization mass spectrometry imaging	23
1.6.1	Techniques for in-house production of emitters: pulling and gravity-assisted self-termination etching.....	24

1.6.2	Atomic layer deposition is used to coat emitters, making them electrically conductive	26
1.7	Retinol, retinoic acid, phosphatidylcholine, and phosphatidylglycerol: important compounds in signaling and cell membrane structures.....	27
1.7.1	Retinol, retinoic acid, phosphatidylcholine, and phosphatidylglycerol under the influence of electrospray ionization indicates their behavior in nano desorption electrospray ionization	30
1.8	Hepatic stellate cells and gastruloids can be used as model organisms	32
2	Aim of study.....	34
3	Experimental	36
3.1	Reagents and solutions	36
3.2	Consumables and hardware	36
3.3	Instruments	37
3.4	Software.....	38
3.5	Etching of capillary emitters.....	38
3.6	Atomic layer deposition to make emitters electrically conductive.....	40
3.7	Examination of emitters in electrospray ionization.....	41
3.8	Preparation of analyte standards.....	42
3.9	Direct infusion using a commercial heated electrospray ionization source	42
3.10	Comparison of etched emitters to a commercial electrospray ionization spray interface.....	43
3.11	Assembly of the nano desorption electrospray ionization instrument platform	44
3.12	Direct infusion between emitters to verify an established liquid bridge	44
3.13	Desorption of analytes from a glass slide	45
3.14	Analyte desorption from hepatic stellate cells	45
3.15	Finding masses and molecular formulas using databases.....	45
3.15.1	Chemcalc.org.....	45
3.15.2	Pubchem and chemspider were also used as databases to annotate mass spectrometric signals	46
4	Results and discussion.....	47
4.1	Etching of emitters proved successful	47
4.2	Atomic layer deposition of emitters gave stable electrospray	48
4.3	Direct infusion of retinol, retinoic acid, phosphatidylcholine and phosphatidylglycerol showed their behavior in electrospray ionization	49
4.3.1	Retinol	50

4.3.2	Retinoic acid.....	51
4.3.3	Phosphatidylcholine	52
4.3.4	Phosphatidylglycerol.....	53
4.4	Direct infusion with etched and coated capillaries proved their ability to be used as electrospray emitters	55
4.4.1	Retinol	55
4.4.2	Retinoic acid.....	58
4.4.3	Phosphatidylcholine	60
4.4.4	Phosphatidylglycerol.....	62
4.4.5	Summary of all direct infusions using in-house made emitters	66
4.5	Assembly of the nano desorption electrospray ionization instrument platform.....	67
4.5.1	The base platform was integrated with a nanospray source.....	67
4.5.2	The sample holder motorized stages were implemented on the right-hand side	68
4.5.3	Micro positioners held the articulating arms for fine tune adjustments of emitters.....	68
4.5.4	A modified nano spray voltage source was incorporated on the arm holding the primary capillary emitter.....	69
4.5.5	Two Dino-Lite cameras were incorporated to monitor the liquid bridge from two angles.....	70
4.5.6	Correct and optimal installation of emitters was time consuming and requires practice.....	70
4.5.7	Shortcomings and suggestions for improvements of the current design.....	71
4.6	Direct infusions of standard analytes via liquid bridge	73
4.6.1	Liquid bridge infusion of retinol	74
4.6.2	Liquid bridge injection of retinoic acid.....	76
4.6.3	Liquid bridge injection of phosphatidylcholine	77
4.6.4	Liquid bridge injection of phosphatidylglycerol.....	80
4.6.5	General remarks after direct injection through liquid bridge.....	81
4.7	Desorption of retinol, retinoic acid, and phosphatidylcholine from glass slide	82
4.7.1	Retinol	83
4.7.2	Retinoic acid.....	84
4.7.3	Phosphatidylcholine	86
4.7.4	Phosphatidylglycerol was not analyzed due to problematic liquid bridge.....	89
4.7.5	General remarks after glass slide desorption.....	89

4.8	Hepatic stellate cells were analyzed on the nano DESI platform.....	89
5	Conclusion.....	91
6	References	94
7	Appendix	101
7.1	Elaborating on bioanalytical method development	101
7.2	Expanding on the versatility of model organisms	101
7.3	The development of organoids and its uses in science	102
7.4	A data processing procedure can be used to graphically represent spectra as images	105
7.5	Parameters to determine before using shear force microscopy	106
7.6	Analyte standards dilution table	107
7.7	Elaborating on the suboptimal making of analyte solutions.....	107
7.8	Table showing signal intensity, TIC variation, and AGC target value for 14 tested emitters.....	108
7.9	Analysis of higher concentration phosphatidylglycerol solutions using the commercial heated electrospray ionization source.....	109
7.10	Gastruloids were analyzed using MALDI imaging	110

1 Introduction

1.1 Bioanalysis: an essential and versatile branch of science in unlocking biological secrets

Theodore William Richards, who won the Nobel prize in chemistry in the year 1914 claimed that: “Chemistry holds the key which alone can unlock the gate to really fundamental knowledge of the hidden causes of health and disease” [1]. Our society has risen into modernity largely thanks to medical developments, with discoveries and advances over the course of the 20th century being so many that focus was shifted from hindering people’s deaths to instead making sure they stay fit. Life expectancy, which is often regarded as one of the key pointers on the effect of not only health care, but also of health education, housing, and nutrition, increased by over 23 years for males and 26 years for females from 1901 by the end of the 1980’s. A plethora of developments, especially with regards to drugs and antibiotics to fight infectious diseases, vaccines, endocrinology, imaging, and increased understanding of cellular biology has led to an unprecedented shift in medical treatment alternatives over the 20th century [2]. A fundamental understanding of chemistry was one of the underlying prerequisites to these developments.

The field of bioanalysis makes use of this fundamental understanding. It describes any analyses done to determine the quantitative or qualitative occurrence of biomolecules in a sample, largely based on taking advantage of chemical or physical principles, e.g., as in methods of chromatography, different forms of spectroscopy, mass spectrometry and so forth. More narrowly, it can be regarded as the analysis of a biological fluid, herein blood, plasma, serum, urine, cell or tissue extracts, saliva, or cerebrospinal fluid to assess and quantify a substance or its metabolite(s) [3]. Such analyses can be done as part of many different processes in a variety of fields, including drug development, medicine, environmental sciences, life sciences, or forensic sciences, and often combines many research areas in material chemistry, biological sciences, biotechnology, and electrical engineering [4], just to mention a few.

1.1.1 Bioanalytical method development is done to make sure optimal results are obtained

A bioanalytical method can be categorized roughly into two main steps/components [3, 5]: firstly, the assay development, validation, and sample preparation, and secondly the detection or analysis of the sample(s) and the associated results interpretation and reporting. **Figure 1** gives the general workflow of a bioanalytical method.

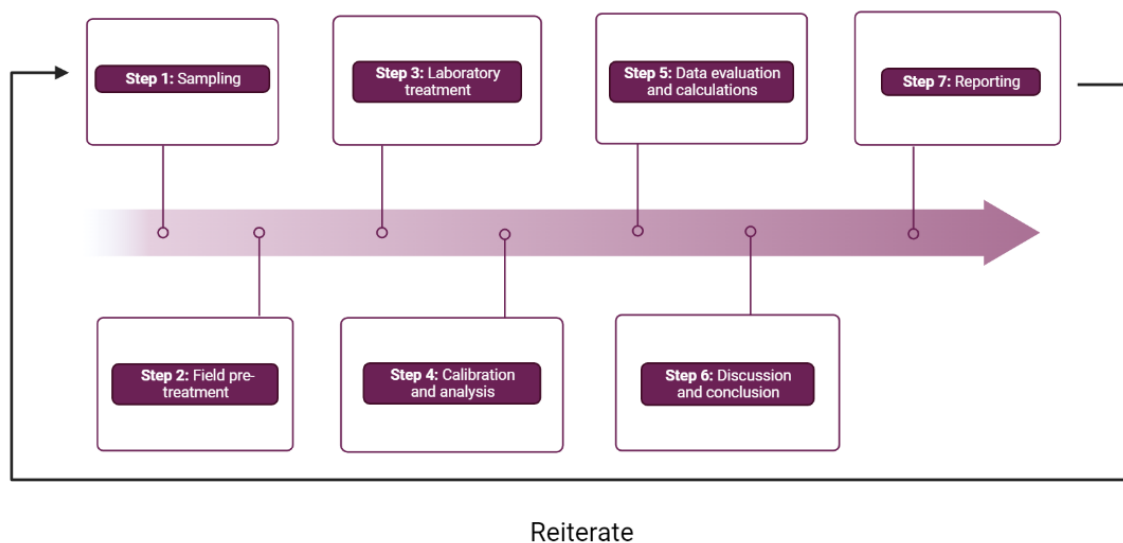


Figure 1. The general workflow in bioanalysis, from start to end. The process is iterated with the newly obtained knowledge in mind, to further optimize the established method. Made using BioRender (biorender.com)

Of utmost importance in bioanalytical method development is assessing the analytes or matrix of interest and developing the method accordingly. Their nature and properties should thus be the deciding factors when undergoing method development.

One case where method development is especially important is in the field of drug development. To evaluate the toxicological, pharmacokinetical, and pharmacodynamical properties of a chemical proposed as a potential drug, bioanalytical methods are developed and applied for validation [6]. This ensures characterization of the analytes themselves, as well as their metabolites and by-products related to all four of the following: adsorption, distribution, metabolism, and elimination [5].

Method development often relies on a validation process to confirm the method's ability to be within certain parameter limits including, but not limited to, the following parameters:

accuracy, precision, recovery, stability, matrix effect, selectivity, specificity, sensitivity, and limit of detection or limit of quantification [7].

For an elaboration on method development in bioanalysis, see **appendix 7.1**.

1.1.2 Human biological systems can be studied using model organisms

Whether developing new drugs for human use, studying the development of human diseases, or in areas of research on human molecular biology and the underlying genetic principles, humans would be the best models. However, this is often not feasible in practice due to ethical reasons with, e.g., the harvesting of tissue and the induction of diseases or genetic manipulation being two examples. Humans would also be costly, as some sort of compensation is often required as an incentive. [8]. Therefore, when conducting research, biological models are often used.

In a broad definition, biological models can refer to any model made to replicate a biological system ranging from a single organism to an entire ecosystem, or to the direct study of a single species. The models help answer questions we may have about other species or even ourselves as humans [9]. Modelling systems are needed for several reasons such as ethics, increased ease of handling, increased financial viability, and the sheer complexity associated with a single biological process in the more developed mammals such as humans. Simpler and more accessible model organisms will then be necessary due to less complexity to infer some useful information which then can be extrapolated to the system for which they serve as models [10]. For instance, worms, rats, and mice, as well as single-cell organisms can be used in development of pharmaceuticals and in the drug industry to conveniently model how the different diseases would affect humans [11]. See **appendix 7.2** for further elaboration on model organisms in general.

1.1.3 Organoids are an up-and-coming model organism

One model that has been implemented more and more over the last 20 or so years is organoids. Organoids are organ-like three-dimensional cellular structures, that can partially replicate the function, identity, and heterogeneity of the authentic human organs [12]. In addition to their histological likeness of regular cells, their ability to self-organize makes them valuable models for studying central underlying mechanisms in human cellular development and organ regeneration, as well as for pharmaceutical drug testing and molecular and biological research [13]. However, organoid technology is still not fully mature, and organoids are not yet exact copies of their endogenous selves. By building an instrument to do a new type of analysis of cellular samples, new information can be revealed to further develop organoids as models. Later, the instrument can be used on organoids within, e.g., disease development or drug responses to reveal information about the system for which they serve as models. For further elaboration on organoids and their development, strengths as model organisms, previous imaging experiments, and examples of its use in scientific research, see **appendix 7.3**.

1.2 Mass spectrometry

Many methods can be used as part of a more comprehensive process within the field of bioanalysis. However, mass spectrometric and chromatographic techniques can be seen in some form or another in almost every bioanalytical research project or routine analysis. In this thesis, mass spectrometry (MS) will be further explored, while chromatography will not be touched. The use of mass spectrometry is due to its intrinsic properties and capabilities of being used in qualitative and quantitative analysis.

MS is an omnipresent method used by practitioners in academia and private sectors alike. Its high sensitivity and superior specificity, combined with concentration detection limits in the pg/mL – ng/mL range, makes it a more desirable instrument compared to other detectors such as UV-VIS, fluorescens and electrochemical detectors [14]. During the late 1990's and early 2000's, MS techniques were the most frequently used, and other detectors like the ones mentioned were almost completely substituted by these setups when hyphenated with a chromatographic system [5]. Mass spectrometry uses an instrument, a mass spectrometer, to distinguish and detect ionized compounds based on their mass-to-charge (m/z) ratio. There are

a wide number of different configurations and working principles, but they all include an ionizing source for ionization and often nebulization of the compounds (e.g., a nano desorption electrospray ionization platform), a mass analyzer for separating the ions based on their m/z -ratio, and a detector to convert the ion current to a meaningful digital signal. The mass analyzer is where the ions are separated in space or in time, and many different physical principles are utilized for the separation in different analyzers. The choice of mass analyzer therefore greatly impacts the obtained results [15]. **Figure 2** shows the general build-up and components of a mass spectrometer.

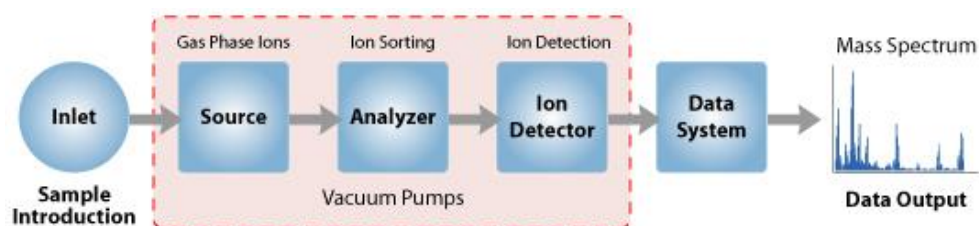


Figure 2. Illustration of the general build-up and components of a mass spectrometer. Practically all mass spectrometers follow this layout. Molecules are introduced in the inlet, before they are ionized in the ion source. The ions are thereafter separated based on their m/z ratio in the mass analyzer, before being sent to the ion detector where a digital signal is produced based on the flow of ions. The data system interprets this signal and gives a readable output [16].

MS is a highly compatible method of analysis for biological samples. Using several chemical, physical, mathematical, and electrical principles, mass spectrometry can detect a particular biological substance among an array of other compounds present in the same sample. The instrumentation itself varies based on manufacturer, cost, and the desired properties such as resolution and mass accuracy. The quadrupole (Q) as a mass analyzer, which is a cheaper alternative with a lower resolution, has been used since the early 1990's due to its ability to separate and characterize low-molecular-weight molecules in biological fluids. However, it poorly separates compounds of very similar masses. Therefore, tandem systems (e.g., a triple quadrupole, QqQ) [5] are used. Here, two or more mass analyzers are coupled in series. This gives the operator the choice to fragment a precursor ion into smaller fragments. These fragments, as well as the precursor ion, can be used for characteristic determination of the compound of interest in methods such as selected reaction monitoring, neutral loss scan, and multiple reaction monitoring. With further development in the field, high-resolution mass spectrometry (HRMS), ion mobility spectrometry, and ion trapping techniques have created a landscape of choices for mass spectrometrists to choose from when conducting analyses, especially in the field of pharmaceuticals and drug development [17].

1.2.1 Orbitrap mass analyzer: a high-resolution mass analyzer

The orbitrap mass analyzer consists of a barrel electrode surrounding an inner spindle electrode, both with very specific geometry [18]. Ions are introduced via the focusing lenses on the outside of the mass analyzer and forced into rotation around the central spindle electrode due to an applied electric potential (DC) which traps the ions in an electric field. To avoid collision with the surrounding barrel electrode in ion introduction, this potential is increased as the ions are introduced to force them into a tighter trajectory around the spindle electrode. This is what is known as squeezing [19]. After squeezing, all ions with identical m/z -ratio travel in packets with slightly different radius to the central electrode and will undergo both axial and radial oscillation in a stable manner due to the geometric configuration of the orbitrap [20]. **Figure 3** illustrates the general structure of an orbitrap.

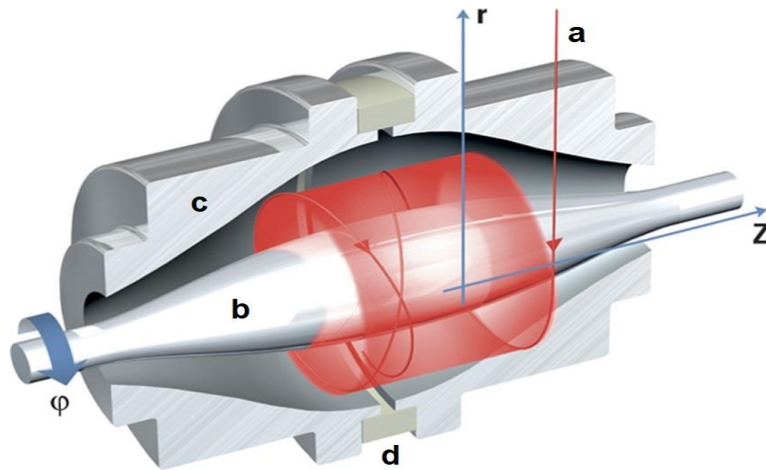


Figure 3. Illustration of the general principles in an orbitrap. After ion introduction (a, red arrow), they rotate back and forth both radially and axially within the field shown in red. The central spindle electrode (b) is shown in the middle, surrounded by the two barrel electrodes (c), which are separated by an insulator (d) [21].

The frequency with which the ions oscillate in the axial direction is given by **equation 1** [22].

$$\omega = \sqrt{\frac{z}{m} * k} \quad \text{Equation 1}$$

Here, z is the ionic charge, m is the ionic mass, and k is a constant field curvature. As can be seen, heavier ions will travel with a lower axial frequency than the lighter ions given they have the same charge.

All moving ions will induce an image current in the outer barrel electrodes, detectable as a measurable electrical current with a frequency corresponding to the frequency of their physical

movement in the axial direction. This signal is then a function of frequency and time, said to be in the time domain. According to **equation 1**, the ions having different exact masses will have a unique oscillation frequency. The total measured signal is therefore a superimposed compilation of the frequencies from all the different types of contributing ions. The spectrum, which becomes increasingly chaotic with the presence of an increasing number of unique ions, is then Fourier transformed from the time domain to the frequency domain. This decomposition reveals the m/z -values of the ions that was present [23]. **Figure 4** shows the process from axial oscillation to determination of the ions' m/z -values.

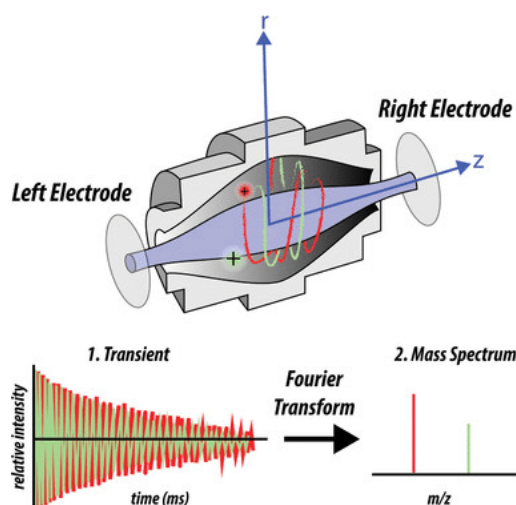


Figure 4. The figure illustrates the series of events in an orbitrap from ion oscillation to a readable mass spectrum. Moving ions induce an image current which leads to a superimposed electrical signal. After Fourier transformation, the m/z -values of all the ions contributing to the superimposed signal is revealed. Reproduced from “A researchers guide to mass spectrometry-based proteomics” with permission [24].

1.2.2 Resolution and mass accuracy are central parameters used in mass spectrometric analysis

During a mass spectrometric analysis, compounds may have the same nominal mass. To separate them prior to them reaching the ion detector, one must have a mass analyzer with a high enough resolution. Resolution can therefore be defined as a mass analyzer’s ability to accurately distinguish two adjacent peaks. In the strict definition, the peaks must have the same height, and the valley between them must not exceed a height of more than 10% of the peak heights. The resolution, R , can then be calculated as given in **equation 2**.

$$\frac{m_1}{m_1 - m_2} = \frac{m_1}{\Delta m} = R \quad \text{Equation 2}$$

Here, m_1 is the m/z -value of the peak with the highest value, while Δm is the difference between them. The formula can be used in two ways: to calculate the resolution achieved by a mass spectrometer, or to calculate what resolution is needed to separate two peaks with 10% valley height. R can also be calculated for a single peak, by using the same formula but letting Δm be the peak width at a specified height, i.e., 50% [25].

A larger R lets the operator distinguish peaks that are closer together. However, even if the mass analyzer can separate compounds of the same nominal mass, instances may arise where they will still often be found very close to each other. Therefore, several options might be viable when choosing which exact peak belongs to the compound of interest. To choose which peak is the most probable one, the mass accuracy can be calculated according to **equation 3**.

$$\frac{(m_{measured}-m_{exact})}{m_{exact}} * 10^6 = \frac{\Delta m}{m_{exact}} * 10^6 = \text{mass accuracy} \quad \text{Equation 3}$$

Here, Δm is the difference between the measured mass and the exact mass of the compound. The m_{exact} is the exact theoretical mass of a particular isotopic variant of the compound. The fraction is multiplied by 10^6 and is thus denoted ppm as it describes how many millionths the measured value is away from the exact value anticipated beforehand. A lower ppm-value indicates a measured value that is closer to the true value and is therefore regarded as a more correct measurement than a higher one, given the instrument is properly calibrated and otherwise maintained.

1.2.3 The properties of a high-resolution mass spectrometer and its impact on mass spectrometric imaging

An orbitrap mass analyzer is often regarded one of the high-end, high-resolution mass analyzers. R is often above 150 000 when coupled to an linear trap quadrupole [18], although other mass analyzers exist with a higher R (over 200 000) [26]. However, this comes at a cost of long scan times, a trade-off when doing high-resolution analyses. The mass accuracy achieved for an orbitrap is normally in the range of 2-5 ppm [27]. In the context of mass spectrometric imaging, one wishes to generate an image showing the spatial localization and quantity of different molecules based on the scans in the mass spectra acquired during an analysis. This can in principle be done by any mass spectrometer if molecules are sampled from

a surface in a systematic fashion. An orbitrap analyzer mass spectrometer is a good choice in imaging because it can, due to its high resolution, separate and determine m/z -values of ions having very similar mass values, and, for imaging purposes, this means more defined and better separated mass spectrometric peaks which leads to more correct quantitation and pixel brightness when visualizing the spatial data. This will lead to better graphical resolution. **Section 1.5.1.** gives a deeper explanation of imaging.

1.2.4 Total ion chromatogram variation and automatic gain control are parameters to ensure stable acquisitions

Whereas the resolution and mass accuracy are parameters for correct molecule annotation, the total ion chromatogram (TIC) and automatic gain control (AGC) are parameters to ensure optimal detection conditions. TIC is a measure of the total amount of ions detected in the MS. TIC variation therefore signifies the difference in total signal intensity from one scan to the next. This value should be as low as possible, e.g., below 10% for Thermo Q Exactive instruments [28], which uses a quadrupole-OrbiTrap tandem MS setup. A low TIC variation value means a stable and reliable ionization and detection system. AGC (automatic gain control) is a measure of how many ions are stored in the C-trap before being sent to the orbitrap and should be equal to the absolute value of the target preset by the operator [29]. This should therefore be at 100%. Reaching the AGC target means a desired number of ions are stored and eliminates space-charge effects and ensures high sensitivity. It may sometimes drop if there is an insufficient number of ions entering the C-trap, which will lead to a lower signal intensity [20].

1.3 Electrospray ionization offers effective ionization and sensitive analysis

For every MS analysis, the sample needs to be on a form that is compatible with the instrumentation. However, biological samples containing the desired analytes does not always meet this criterion and cannot always be directly injected or introduced into an analytical

instrument. In addition to various extraction or pre-separation processes, nebulization and ionization of the compounds is a necessary prerequisite for MS analysis [30].

Compatibilizing methods were therefore invented, one of them being electrospray ionization (ESI) capable of both ionization and nebulization of compounds before they are sent to the mass analyzer for m/z determination. ESI is said to be the most prevalent method of ionization together with matrix assisted laser desorption ionization (MALDI), and has laid much of the foundation needed to transfer the application of mass spectrometry to biological and biomedical sciences [15].

1.3.1 Several models explain the course of events in electrospray ionization

ESI is carried out by pumping the liquid to be analyzed through an electrically conductive emitter, onto which an electrical voltage is applied. This pumping can be done by either a syringe pump, or a chromatographic pumping system. The typical emitter is of stainless steel, with an outer diameter (OD) of 200 μm and inner diameter (ID) of 100 μm . A drying gas, often N_2 , is sent coaxially with the sample to help with the subsequent necessary evaporation of sample liquid and is a central part in the nebulization. The gas also contributes in directing the sample droplets into the MS inlet. Between 2-6 kV of voltage is applied to the emitter as one pole, and the inlet of the MS is used as the opposing pole [31]. **Figure 5** shows the general ESI instrumentation.

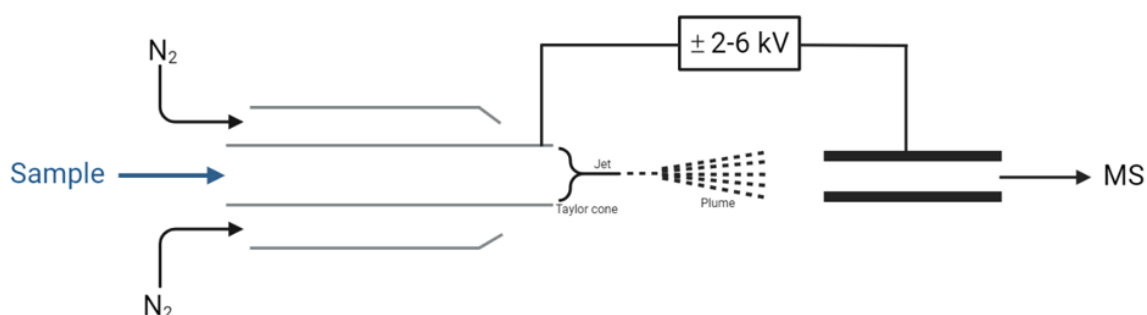


Figure 5. The figure shows the conventional ESI instrumentation. The sample is introduced through the sample emitter, accompanied by a coaxial flow of nebulizing nitrogen gas. Due to the applied voltage, the sample is being pulled in Taylor cone, which subsequently forms a jet of liquid, before exploding into a plume. The sample is thus introduced as a fine ionized spray into the MS. Made using BioRender (biorender.com).

By applying voltage to the system, an electrical field is produced pulling the meniscus of the liquid exiting the emitter. This gives rise to a distinct shape termed the Taylor cone, from which a jet of liquid is propelled. This jet ends in a plume of liquid particles, also depicted in **Figure 5**. From here, as liquid evaporates from the droplets, they disintegrate to smaller droplets, increasing the charge density until the surface tension can no longer sustain the repulsive charges. At this point, the Rayleigh limit is reached [32]. It is thought that the droplet either explodes in smaller droplets through Coulomb explosion [15], or that smaller droplets are continuously ejected from the main droplet's elongated tail, formed because of air drag on the drop [33]. **Figure 6** shows the Coulomb explosion and tail ejection.

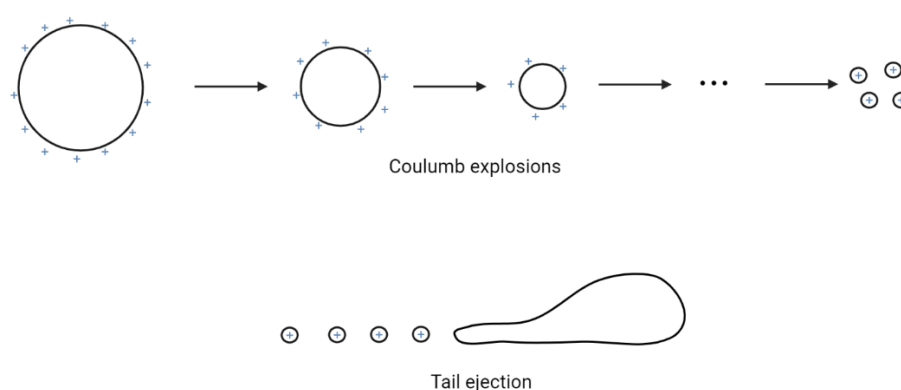


Figure 6. Two models for droplet size decrease. Recurring coulomb explosions due to increased charge density, and continuous tail ejection. Both results are a result of the exceedance of the Rayleigh limit. Made using BioRender (biorender.com).

The discussed mechanisms lead to very small, charged droplets. It is these small droplets that are further subjects to one of two evaporation models for generation of sole ions, either the charged residue model (CRM) or the ion evaporation model (IEM). In the CRM model, Coulomb explosions occur until the droplet contains only one analyte at the end of the cascade. This one analyte is then left with a charge [34]. This model is found to suit smaller lower-mass ions best. In IEM, analyte ion molecules evaporate directly from the highly charged surface of droplets. This happens when the droplets' radii is < 10 nm and subjected to a strong electric field, leading to emission of partially solvated gas phase ions [34, 35]. This model is found to suit higher-mass ions best.

A normal ESI system can be downscaled with respect to emitter dimensions and flow rate, and the domain of nano ESI can be reached. In nano ESI, the emitter is typically between 1-4 μm ID [31], but experiments have been done with sizes up to 50 μm ID. At the higher part of this range however, it is more commonly termed micro ESI [36]. The emitter, made from

borosilicate, are often pulled using a capillary puller, to fit the needs of the user regarding inner diameter. A lower flow rate is also used, but the ranges used and the terms to label them vary from a few tens to a few hundred nL/min. The reduced flow rate has implications on the ionization process as the plume droplets start at a size about 100-1000 times smaller than in normal ESI [31, 36]. This leads to a more effective ionization process because the droplet reduction happens faster, leading to increased signal intensity per sample volume. Another consequence is less spreading of the spray. Because of the reduced flow, increased ease of evaporation, and less spreading no nebulizing gas is required in this format. The shorter time required for ionization also lets the emitter be positioned closer to the MS inlet. Therefore, more of the cone-shaped spray will enter the MS, again leading to higher signal intensity. A better ionization process will also lead to a more stable spray, and therefore a low TIC variation. **Figure 7** gives a general overview of the macroprocesses leading to ionization in a nano ESI source.

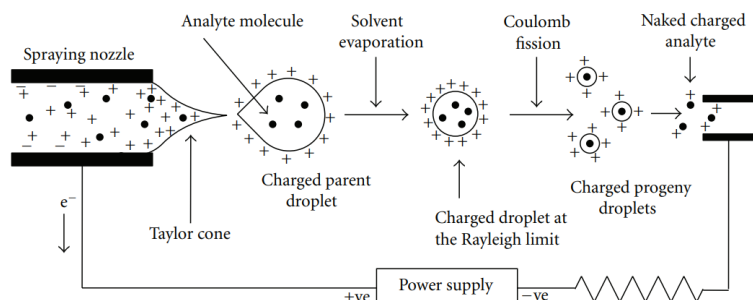


Figure 7. A schematic representation of the processes leading to ionization and nebulization of molecules in a nano ESI source. No nebulizing gas is required, and the droplet reduction happens quicker due to a smaller starting droplet. From “Electrospray Ionization Mass Spectrometry: a technique to access the information beyond the molecular weight of the analyte” [31].

1.3.2 Electrospray ionization has a vast area of use in many types of sciences

ESI as a whole is a widespread, soft ionization technique, meaning the compounds will not fragment upon ionization. It is used within fields of protein and peptide analysis, analysis of small molecules (100-1500 m/z) in drug development, metal complexes, surfactants, oligonucleotides of both DNA and RNA, and oligosaccharides, but also of bigger protein complexes over 1 MDa [15].

ESI is also an ionization method suited for substances prone to obtaining either a positive or negative charge. The ESI needle and MS inlet acting as opposing electrodes can have their polarity switched. For negative mode, the ions entering the MS have negative charge, while the ions have a positive charge in positive mode. For negative mode, the needle is set to be the negative pole, as this will repel all negative ions in the solution to exit the emitter. The negative ions are subject to evaporation according to the models previously explained. For positive mode, the opposite is the case. This freedom of ionization mode is welcomed by many scientists working with different types of substances.

1.4 Desorption electrospray ionization, a close relative of electrospray ionization

Another ionization method, based on many of the same principles found in ESI, is desorption electrospray ionization (DESI). This method works by desorbing the desired analytes in an organic or biological sample into the surrounding volume and into the mass spectrometer as a nebulized gas. The process of desorption and ionization works by spraying a solvent on the sample through an emitter on which an electric potential is applied. The solvent molecules are thus ionized by the electric potential and transfers their charge to the analytes in the sample where the spray hits. Charge transfer usually occurs through protonation and follows the same ionization theory found in literature for regular electrospray ionization (ESI). Droplets containing matrix components, including the analytes of interest, are shot up by the physical forces applied by the spray and evaporates in accordance to the ion evaporation model or the charge residue model [37] described in **section 1.3**. The ionized analytes are then sucked into the MS inlet by the vacuum in the instrument [38]. **Figure 8** shows the general principles of DESI.

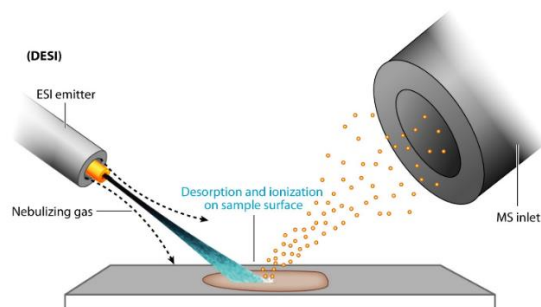


Figure 8. A schematic illustration of the general working principles of DESI. From “Ambient ionization mass spectrometry” [39]. The mechanisms for DESI are the same as those occurring in regular ESI, see Figure 5.

Important parameters in this ionization method are the choice of solvent, the polarity of the solvent mixture, the angle between the spray emitter and the sample surface, and the angle between the sample surface and the MS inlet. The distances between emitter and sample, and sample and MS inlet are also of significant importance [40].

For animal and human analyses, solvents consisting of methanol and water predominates, and makes up about 68% and 46% of the solvent systems chosen for animal and human analyses respectively. Use of other choices and combinations is also described, such as acetonitrile and dimethylformamide [41]. However, one must always assess the analyte of interest when choosing the solvent composition, but the more frequent methods can be a good starting point when conducting optimization. The angles used in the DESI system is also described as a key parameter, often being between 45-55° for solvent emitter to sample, and 10° for sample to MS inlet [42]. However, some experiments show best results with an angle of 58° (positive mode) and 60° (negative mode) between the emitter and sample [43].

Ionization with DESI works with small organic molecules as well as larger biomolecules, and is characterized as a soft ionization technique causing little fragmentation [38]. It has high throughput, and can be used in a diverse range of analyzes, like explosive residues of RDX (cyclonite, or hexogen) and trinitrotoluene (TNT) [44], pharmaceuticals [45], and biological matrices such as urine [46]. Raw, untreated samples of plant [47] and animal [48] tissue has also been subject to analysis. Overall, with its minimal need for preparation, DESI offers many advantages. In many ways, the technique is similar to regular ESI, but the sample is not introduced through the emitter carrying the electric potential. Instead, the sample is placed on a holder in front of the MS inlet and desorbed from there. This gives rise to the distinguishing of the two methods. As the main drawback, one study found the analysis of heavier molecules (over 2000 Da) difficult. Also, for imaging purposes, other methods will give images with

higher resolution as DESI is not able to spray and acquire a signal for a single cell at a time [49].

1.5 Nano desorption electrospray ionization: its buildup and working principles

Nano DESI utilizes the core principles of normal DESI, but with two main differences. Firstly, normal DESI have one emitter while nano DESI utilizes two emitters: one delivering the solvent for desorption of the analytes from the sample, the primary capillary emitter (PCE), and another for transport of the desorbed analytes to the MS-inlet, the nanospray capillary emitter (NCE). Secondly, there is a downscaling of the emitter dimensions. As to the authors knowledge, there is no standardized size categories for when the term “nano” is appropriate. However, regular DESI-emitters often have an ID of $>100\ \mu\text{m}$, whereas nano emitters have an ID $< 100\ \mu\text{m}$, and even below $25\ \mu\text{m}$. A smaller ID of the emitters will miniaturize the analysis, in that a lower flow rate is used. The area subjected to desorption is also smaller. Because of these two aspects, the desorption extracts a smaller number of analytes for detection at any given time. Further consequences of this are elaborated under “Execution of MS-imaging” in **section 1.5.1**.

Between the two capillaries, a small liquid junction is formed called the liquid bridge. When in contact with the sample, analytes are desorbed into the bridge and extracted through the NCE which delivers them to the MS [50]. The bridge can be viewed as the Taylor cone part of the spray coming out of a nano ESI emitter, hitting the sample surface before the full spray gets to form.

An electric potential is applied between the PCE and the MS inlet. The liquid bridge that is maintained through continuous delivery of solvent secures a closed electrical circuit between the PCE and the MS inlet, with the circuit also involving the NCE. In this way, the ionization and nebulization process happen at the end of the NCE by the mechanisms of regular ESI, right before the analytes enter the MS. Similar to normal DESI, a mixture of water and methanol is often used in the nano format [50]. **Figure 9** illustrates the configuration of a nano DESI setup.

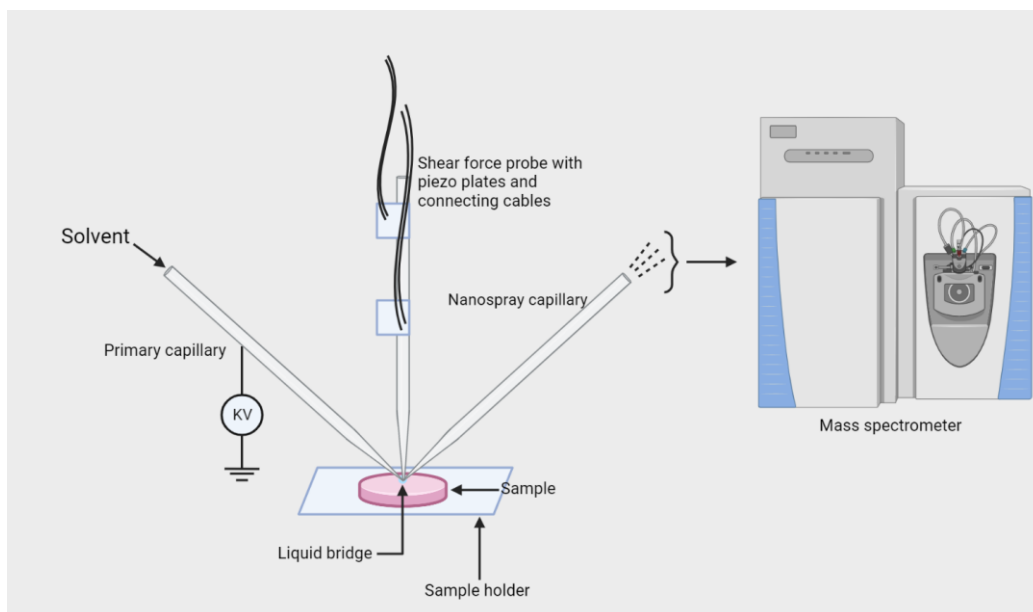


Figure 9. A schematic illustration of a nano DESI-MS. Made using BioRender (biorender.com).

1.5.1 Nano desorption electrospray ionization is used for mass spectrometry imaging

Mass spectrometric imaging (MSI) is the spatial mapping and localization of analytes in a sample, and their quantitative and qualitative determination. Analytes can be mapped untargeted in two dimensions, and thousands of unique molecules can be imaged in a single, label-free experiment [51]. This is an advantage compared to techniques relying on staining. Imaging technology is useful in many ways, and constitutes a potent technique for biological, clinical, and drug-related analysis [50]. Mainly two instrumental features are combined and utilized in imaging. One is the specificity of a mass spectrometer, capable of separating and accurately identifying compounds based on their m/z -ratio. The other feature is an ion source's ability to move either the sample or a system of microprobes in a way that allows the MS to only analyze certain spots at a time in a systematic manner. The intensity of the signal of a given analyte will vary with location due to uneven distribution in a cellular sample, but abundance can be mapped using signal intensities in correlation with the sample's position relative to the probe [52].

One of the first of these kinds of analyses is MALDI-MSI and has been performed since the late 90's, after it was introduced by Caprioli *et. al.* in 1997. It offers high sensitivity, and is capable of mapping the desired molecules in a two-dimensional manner on the sample surface [53]. With improvements through time, the acquired spatial resolution has gone down to 1-2

μm [54], which makes it a desired technique. Here, spatial resolution refers to how many pixels the analyzed tissue can be divided into and is one of the most important parameters when evaluating MSI performance. The more pixels, the lower spatial resolution, and the higher graphical resolution. The main drawback of MALDI-MSI is the requirement for matrix-related sample preparations. Such preparations are diminished to a minimum in nano DESI-MSI, which gives higher throughput and less use of time and resources. However, the resolution achieved with nano DES-MSI is still in a process of development, and resolutions lower than $10\ \mu\text{m}$ are still not often obtained [50].

Mass spectrometry imaging is executed using a probe system that systematically desorbs analytes from tissue samples

Nano DESI-MSI can be executed using the nano DESI microprobe system consisting of the PCE and NCE, which are set on stationary micro positioners. The sample holder on the other hand is set on a computer controlled motorized stage, that can be programmed to change its location with time in all three spatial axes. The sample can thus adjust its position relative to the nano DESI probe, so that the liquid bridge desorbs analytes from the sample in a systematic pattern. In this way, lines of tissue can be scanned sequentially at a given velocity and with a fixed distance between each line. The sequentially desorbed analytes are detected in the MS, and the signal output can be related to the location and quantity of the analytes through the use of software [50]. **Figure 10** gives a graphical summary of the scanning process.

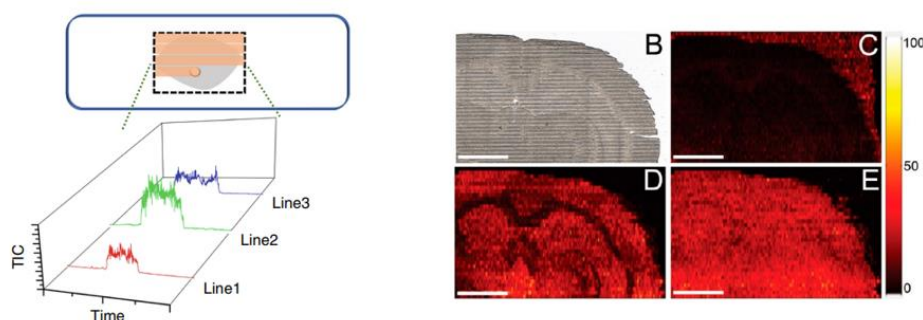


Figure 10. Left: the tissue sample is scanned sequentially in lines. Presence of analytes gives rise to a signal that is proportional to analyte ion count, and changes with location. Figure adapted from “High spatial resolution imaging of biological tissues using nanospray desorption electrospray ionization mass spectrometry” [50]. Right: example of a result obtained by Lanekoff et. al. after using nano DESI-MS for imaging of rat brain tissue. (B) shows a slide of scanned tissue. (C) shows the abundance of solvent, (D) shows the abundance of the $[M+K]^+$ potassium adduct of PC(34:1), and (E) shows the abundance of the $[M+K]^+$ potassium adduct of creatine. This image has a resolution of $\sim 35\ \mu\text{m}$. Figure adapted from “Automated platform for high-resolution tissue imaging using nanospray desorption electrospray ionization mass spectrometry” with permission [55].

Since the desorption of analytes only happens where the liquid bridge is, the size of the liquid bridge is what determines the achieved spatial resolution [50]. The pixels cannot be smaller than this area, and this is one of the main incentives for the downscaling of emitter sizes. However, there are additional factors affecting exactly what the resolution becomes, with different factors influencing how the resolution is calculated in x-direction and y-direction. Each pixel in an image will have its own unique mass spectrum, where the resolution in x-direction is dependent on the distance travelled by the desorption probe per scan of the mass spectrometer as described in **equation 4**.

$$\frac{\text{velocity in } x\text{-direction } (\mu\text{m} / \text{s})}{\text{instrument scan rate } (\text{Hz})} \quad \text{Equation 4}$$

This gives a distance in micrometers, describing how much of the sample in x-direction was covered for a given mass spectrum, and therefore a given pixel. The resolution in x-direction will be lowest with a slow velocity and a high scan rate. In y-direction, the resolution is decided by the width of each scan line and the spacing between them. A lower spatial resolution is achieved by lowering the line spacing distance and decreasing the liquid bridge area, hence why the emitter sizes have a large impact.

A downside of a high graphical resolution is data space, as each line will have more pixels and therefore more spectrums. More lines will also lead to proportionally more spectrums, additionally increasing the data. Therefore, it is not always beneficial to run an analysis with as slow a probe velocity in the x-direction as possible while simultaneously having the highest scan speed or decreasing y-resolution by having as minimal distance between lines as possible.

Overall, a better spatial resolution leads to a more certain characterization of the occurring analytes, both spatially, qualitatively, and quantitatively. However, a smaller total amount of analytes is desorbed with a smaller liquid bridge which will impact the signal intensity as there is a proportional relation between signal intensity and sampled area [40]. Also, signal loss will be problematic if one wishes to execute tandem MS in several generations.

The data processing procedures used to generate images from acquired mass spectra are found in **appendix 7.4**.

Shear force microscopy can be used for height adjustment correcting for varying sample surface topography

When using a probe system for location-dependent analyte desorption and ionization, a set of motorized stages is responsible for the systematic sequential scanning of the sample by movement of the sample holder in the x and y direction. However, to make sure the probe system works consistently a height controlling mechanism is also necessary to achieve low spatial resolution, as there will be topographic microvariations for a cell sample surface. To adjust the height of the emitter system and keep the predetermined probe-to-sample distance, shear force microscopy (SFM) can be used [50].

In SFM, a capillary needle called a shear force probe (SFP) is held at an orthogonal angle to the sample, with the tip of the probe being in physical contact with the sample. This probe is also illustrated in **Figure 9**. Oscillation is then induced in the probe using piezoelectrical materials attached to the needle. These are materials that can carry an electric charge when exposed to physical strain or stress, e.g., when forced to expand or contract. This effect is reversible, meaning that when an electrical charge is applied to the material expansion and contraction are induced at a certain frequency depending on the voltage of the current [56]. For height control in a nano-DESI setup, ceramic piezoplates can be attached to the SFP, and current can be run through one of the plates. This causes the entire probe to oscillate laterally with a fixed amplitude at a given frequency, due to the mechanical movement induced in the piezo material. The oscillation amplitude is reduced when the probe meets physical hinderance, as is the case when it is in contact with the sample. This reduction in amplitude can be picked up by another detection piezoceramic plate, also attached to the SFP. The detection plate can be connected to a computer-controlled closed feedback loop which will correct the height of the entire sample holder, to maintain the constant emitter-to-sample predetermined distance using the oscillation amplitude of the SFP as the decisive parameter. This way, analytes from each part of the cell sample surface will be desorbed in an equal fashion, securing reproducibility across cells and across samples. The system is also able to correct for the opposite scenario, where the amplitude of the oscillation is increased due to total loss of sample contact. Therefore, some contact between the SFP and the sample surface is ideal, and deviations from the specific amplitude causes corrections [50].

For interested readers, more on the practical aspects of SFM are found in **appendix 7.5**.

1.5.2 Parameters characterizing high-quality emitters

The PCE and NCE are essential components in a high-resolution nano DESI setup. The SFP is not an absolute necessity but will largely contribute to the decrease in spatial resolution and increase in analysis consistency. High-quality emitters are of interest, which in this context means having a symmetrically shaped tip of small ID and OD, delivering a small and stable flow of solvent and desorbed sample, not being easily clogged, a long-lasting functionality, and having no material weaknesses or flaws that can cause the emitter to break or fault when in use.

For the PCE and NCE, good quality is wanted to ensure stable deliverance of solvent to the sample and maintaining a small liquid bridge for good spatial resolution. As the size of a Taylor cone in the electrospray produced is generally a product of the emitter OD [57] and not just the ID, a small liquid bridge can only be achieved with a small emitter tip. In addition, careful positional and angular adjustments between emitters as well as solvent flow adjustment between them, contributes to a smaller liquid bridge if done correctly [50]. To ensure optimal positioning of the emitters, microscope cameras are often used for monitoring from several angles as adjustments happens within distances on the micrometer scale. As for the SFP, a small tip is beneficial to ensure a sensitive mechanism in detecting topographic variations on the tissue sample.

1.5.3 A summarization of the important components of a nano desorption electrospray ionization platform

The theory and background behind the nano DESI and its working principles have now been laid out. **Table 1** below summarizes what components or other factors must be included, their use, and if it will be included in this thesis when building the platform.

Table 1. The table lists the necessary components of a functional nano DESI platform, as well as other factors that are used for optimization and testing at the various steps.

Component	Use	Planned included/used in this thesis
Base	Creating the space onto which other components are attached	Yes
Primary capillary emitter	Electrically conductive emitter for delivery of desorption solvent onto sample	Yes
Nanospray capillary emitter	Pick-up of solvent containing analyte for delivery to the MS	Yes
Micro positioners	Fine positioning of emitters	Yes
Microscope cameras	To ensure correct and optimal emitter position	Yes
Sample holder	A frame where glass slides containing sample is put	Yes
Motorized stages	Electrical and programmable stages to move the sample in a predetermined pattern in all three axes	Yes
Control software for sample holder	A computer program to give the three stages instructions on where to move	Yes
Height adjusting mechanism	To ensure constant probe-to-sample distance for optimal results	Yes
Imaging conversion software	Software to convert all the acquired mass spectra to a single image	Yes
Chemical standards	To do testing of the platform at each point of development	Yes
Cellular samples	To test whether the system, when ready, can desorb analytes from cells (organoids, gastruloids, etc.)	Yes

1.5.4 Comparing imaging using nano desorption electrospray ionization to other ionization methods

Other nanoscale techniques used for single cell analysis such as MALDI MS and secondary ion mass spectrometry (SIMS) exist, but these are performed under vacuum and requires specific and sometimes elaborate sample preparations. This makes them more comprehensive techniques. In addition, extensive fragmentation occurs in SIMS, which are often unwanted. It does however have the best preconditions for low resolution [52]. Several atmospheric pressure methods, often referred to as ambient techniques, have been used for single cell analysis [58],

which eliminates the need for high vacuum and the associated complications. It should be mentioned that MALDI can be done at atmospheric pressure [59], but there are still the matrix related preparations. Ambient ablation techniques like laser ablation electrospray ionization (LAESI) and laser desorption/ionization droplet delivery (LDIDD) are also being used [58]. In comparison to the above-mentioned techniques, nano DESI-MS offers high throughput, efficient analysis with little sample preparation, and can be done at atmospheric pressure. The possibility of changing the composition of the solvent for selective desorption of wanted analytes [60] deserves a mention as well. Also, this is a soft ionization technique that will preserve the molecular ion and is suited for both quantitative and qualitative analysis of metabolites, lipids, proteins, and drugs [58]. **Table 2** shows a concise comparison of the different methods, also mentioning some inherent advantages/disadvantages.

*Table 2. A comparison of a selection of imaging techniques. *For laser-ablation ICP-MS.*

Techniques	DESI-MS	Nano MS	DESI-MS	MALDI MS	SIMS	LAESI
Pressure	Atmospheric	Atmospheric		Vacuum/atmospheric [58]	Vacuum	Atmospheric
Preparations	None	None		Matrix preparation and deposition	Surface polishing and coating with metal [61]	None (LAESI)
Fragmentation softness	Soft	Soft		Soft	Hard	Soft [52]
Lowest spatial resolution	150-200 μm [50]	< 10 μm		2-3 μm [50]	< 1 μm	1 μm^*
Other factors	Solvent can contain IS – major advantage [50]	Solvent can contain IS – major advantage		Matrix may interfere with analyte signal High mass range (100 000 Da)	Limited mass range (<1000 Da), but can be used for element analysis	The lowest theoretical spatial resolution is only limited by the laser diffraction limit.
Main source of the method	[52]	[50]		[52]	[52]	[62]

1.5.5 Analysis of cells using nano desorption electrospray ionization imaging is a productive step towards further model development

The collective literature on nano DESI is clear about the potential of the system's ability to analyze cell samples. It can be used to do high-resolution imaging of not only regular cell samples, but also of other model organisms such as organoids, gastruloids, and cancer models,

to monitor the processes that occur within these cells. The qualitative and quantitative occurrence of different biological compounds is a good pointer when determining whether the models are behaving like their counterparts or not. When doing organoid imaging, both the cellular location and the quantity of the analyzed compounds will be revealed if quantitative techniques are used, and the signals can be compared to regular cells. Further development of the organoids with respect to these differences will then hopefully lead to the organoids being better models in the future.

The quality of the results of an imaging analysis will depend on the ionizing analyte desorption system, herein the nano DESI-setup, with the main factor impacting the graphical resolution being the size of the liquid bridge. However, if a good resolution with respect to the nano DESI-system is achieved, a good mass spectrometric system is still needed, also having a high mass resolution and low mass accuracy to take advantage of the high-resolution desorption system. This is ensured through use of a tandem mass spectrometer consisting of a triple quadrupole and an orbitrap.

1.6 Production of capillary emitters for nano desorption electrospray ionization mass spectrometry imaging

Commercial emitters exist for the normal DESI format, but to the authors knowledge no commercial emitters are available for use in nano DESI. The emitters either have a too large ID ($> 10 \mu\text{m}$) or are not coated with an electrically conductive material, such as PepSep's non-conductive polyether ether ketone (PEEK) emitter [63] and Fossil Ion Tech's non-coated emitters [64]. Therefore, emitters are generally produced in-house using a few different techniques.

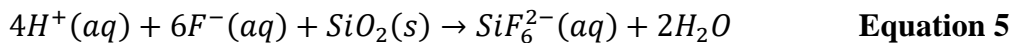
1.6.1 Techniques for in-house production of emitters: pulling and gravity-assisted self-termination etching

Pulled emitters

One of the production techniques, known as pulling, heats the capillary to increase its flexibility before pulling at both ends until wanted ID and OD is achieved [65]. Such emitters have a tapered shape of shrinking ID and OD from the back end to the tip which makes them prone to clogging as large particles can enter on the back end without being able to escape through the tip. Pulled emitters are also known to have reproducibility related issues [66]. The production is nonetheless a quick process.

Gravity-assisted self-termination etching

Another technique termed etching was developed to overcome the weaknesses of a pulled emitter [57, 67-69]. Etching is done by exposing the fused silica to hydrofluoric acid (HF), to let the net reaction given in **equation 5** take place [70].



In previous and pioneering work, Kelly et. al. lowered the tip of a fused silica capillary in a HF-solution. This caused the HF to creep up the outer walls of the capillary due to surface tension forces. The walls would etch away, but the level of HF would decrease due to continuous evaporation creating a tapered emitter tip of decreasing OD. Due to the same surface tension, HF-solution would also creep up the inside of the capillary, increasing the ID in an unwanted fashion [57]. Emmett et. al. avoided this unwanted effect by flowing water through the capillary to keep the HF from entering [71]. This would however lead to dilution of the HF-solution and demanding a higher HF use [69]. Gas flow has also been used to prevent the same unwanted effect [72]. With these methods, the etching process must be stopped manually at the desired OD and ID, to not etch away the entire emitter tip.

Zhu *et. al.* developed a method without the accompanying complications that comes with HF creep. Instead of etching and creating a taper at the capillary tip, they exposed the silica in the middle of the capillary to HF by threading on a small plastic cup with an orifice in the bottom, hanging the capillary with the cup in a vertical fashion, and filling the cup with HF. This reduced the amount of HF needed as there was no dilution, did not increase capillary ID, and would end

the etching process as soon as the outer walls were too thin to withstand the gravitational pull of the cup, the rest of the emitter, and any remaining HF solution. Because of this automatic ending, Zhu et. al. named this technique “gravity-assisted self-termination etching” [67]. Stian Kogler further developed this method and has laid the foundation for the method used for emitter production at the bioanalytical chemistry group, University of Oslo (UiO). **Figure 11** shows an illustration of the etching setup as invented by Zhu et. al.

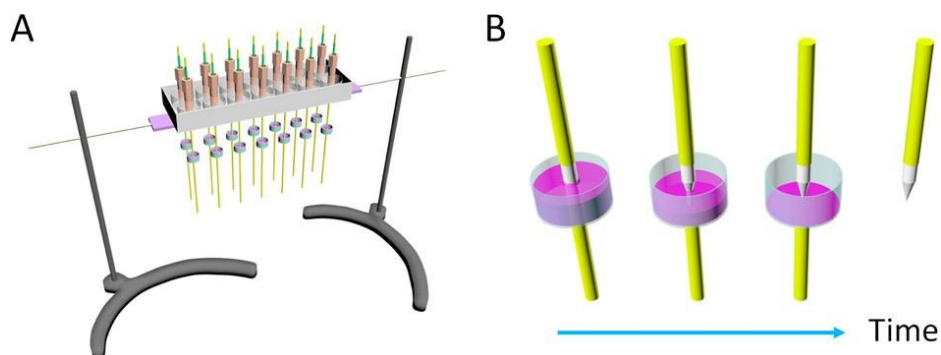


Figure 11. The setup of gravity assisted self-termination etching, as invented by Zhu et. al. A: emitters are hung in an apparatus, with cups containing HF threaded on the capillaries. B: the etching process at different points in time. Adapted from “gold-coated nanoelectrospray emitters fabricated by gravity-assisted self-termination etching and electroless deposition” [67].

One of the biggest contributions of Kogler was implementing round-bottom cups instead of flat-bottom cups. This would lead to more consistent etching, as HF-solution would not be able to gather at the edge of the cups as they would in flat-bottom cups [68]. In producing a good emitter with all the important qualities this implies, Zhu et. al. argues one of the most important parameters is the weight of the cup and added HF. As long as the weight of the cup and the amount of added HF is the same for all emitters, a reproducible result should be expected [67], given the cup is not threaded asymmetrically as this may also give rise to asymmetrical emitter tips [73]. The cups in Kogler’s thesis were made by hand but using 3D-printed cups would be an improvement. Ease of preparation and a presumed increased symmetry are thought the main advantages. Also, when 3D-printing using precise machines, the shape and weight of the cups are thought to be more homogenous when cross-comparing.

Different steps of the etching process using Kogler’s round-bottom cups are depicted in **Figure 12**.

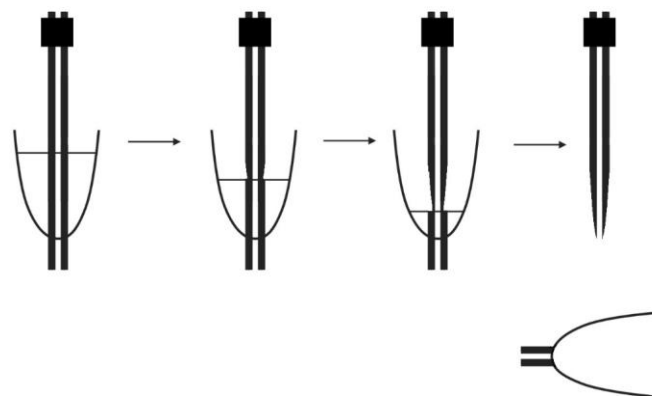


Figure 12. Gravity assisted self-terminating etching of capillary emitters at different time points during the continuous etching process. The tip gets a tapered shape because the HF evaporates over time, exposing the lower parts of the emitter for a longer period. Made using BioRender (biorender.com).

1.6.2 Atomic layer deposition is used to coat emitters, making them electrically conductive

Emitters for use in ESI must be able to carry an electrical current, to ensure the formation of an electrospray [15] as described in **section 1.3.1**. This is achieved through either using a liquid junction, or through an electrically conductive coating on the outside of the ESI emitter. Because nano DESI is dependent upon the formation of an ESI spray at the end of the NCE, these emitters must be coated with a conductive layer.

One of the methods of coating emitters is atomic layer deposition (ALD), where one layer of atoms is deposited on the surface of the emitters at a time. This is done in a reactor through cyclical introduction of precursors, reacting with the surface material. Purging of leftover precursors and unwanted by-products is carried out at the end of each cycle before a new atomic layer is deposited in the next [69].

Because the process follows the rules of chemisorption, new chemical bonds are created between the precursors and surface of the emitters. When no more sites of reaction are available, the process will come to a halt until more precursors are introduced. One can therefore strictly regulate the deposition process, which is said to be self-limiting. This means the morphology of the atomic layers can be controlled to a high degree with respect to thickness and conformality [74]. **Figure 13** shows the general cyclical process of ALD.

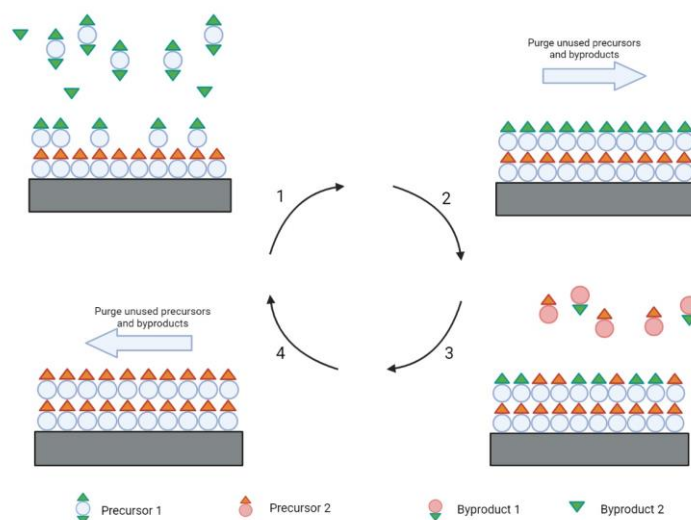


Figure 13. General overview of an ALD process. Precursor 1 and 2 are introduced and deposited on the material surface. This leads to byproducts 1 and 2, which are cyclically purged along with unused precursors. Made using BioRender (biorender.com)

A common approach to coating is by deposition of precursors to form atomic layers of SnO₂. A paper by Cheng *et. al.* claims obtaining such coating is mainly done through two different routes: metalorganic reagents and inorganic reagents. For the inorganic approach, the most common tin precursor is SnCl₄ due to its cost effectiveness, ease of handle, and with a moderate vapor pressure at room temperature. Films using this precursor is also expected to have a higher electrical conductivity. They used H₂O as the other oxidizing reactant to obtain the SnO₂ [75]. According to a review paper by Nazarov *et. al* who compared 10 different inorganic combinations as well as 16 metalorganic combinations precursor concluded the reactants are of importance in coating properties, also claiming SnCl₄ are among the most common tin reactants. For many of the approaches reviewed, H₂O is chosen as the oxidizing reactant [76].

1.7 Retinol, retinoic acid, phosphatidylcholine, and phosphatidylglycerol: important compounds in signaling and cell membrane structures

When researching development of cellular entities, choosing some model compounds that reflect the research aim are of interest. For organoid development, understanding retinol and retinoic acid, as well as phosphatidylcholine and phosphatidylglycerol are of interest because

they play a central role in signaling and membrane constitution. The phospholipids are also common analytes when testing imaging platforms due to their abundance and ease of detection.

The chemical structure of the retinoids retinol and retinoic acid (RA), as well as the phospholipids phosphatidylcholine (PC) and phosphatidylglycerol (PG) are given in **Figure 14**. The retinoids can have different stereoisomeric configurations but given here are the all-trans variants which are the variants in focus for this thesis.

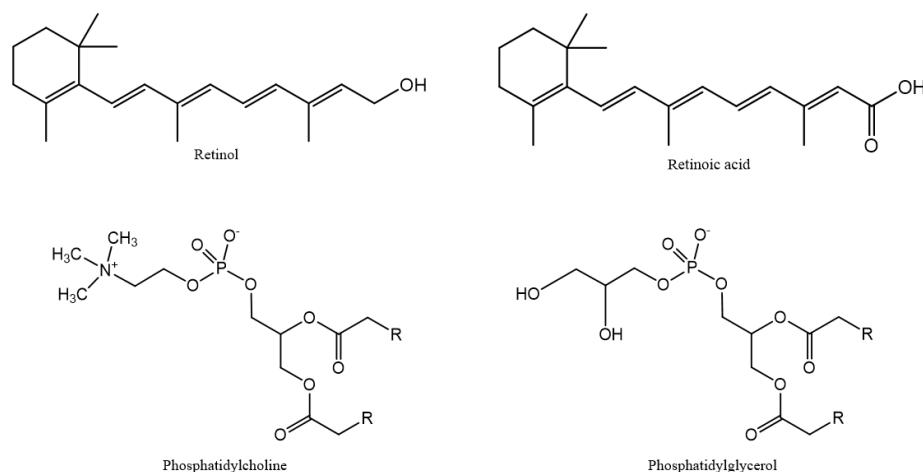


Figure 14. The chemical structure of the four analytes to be analyzed from organoids. Phosphatidylcholine and phosphatidylglycerol have differing fatty acid chains and are generically denoted as R-groups. Made using Chemdraw.

Retinol and retinoic acid

Retinol, also known as vitamin A, is a fat-soluble organic compound and is the anchor substance for the wider group of chemicals called retinoids, which are analogues of retinol. Other substances included in the group are carotenoids, e.g., β -carotene. The carotenoids are mostly found in plants and plant-based foods, while retinol itself is introduced via animal products in the form of retinyl esters [77]. It is responsible for many vital tasks in the human body, playing a role in development and maintenance of vision, helping in cell growth and division, functioning of the immune system, and for development of a healthy baby during pregnancy [78]. The effects of retinol also stretches beyond baby development, and contributes to regulating fertility, controlling neoplastic growth, and preventing neurodegenerative diseases [79].

Retinoic acid is commonly known as a retinoid and is also a vital substance for normal cell development. It is sometimes attributed to be the major active form of vitamin A and binds to several different nuclear receptors to alter gene expression [80]. By slowing the rate of cell division and inducing differentiation of immature and transformed cells towards more developed and potent cells, it contributes to the maintenance of healthy cells in all types of tissues. This all has positive implications on the resistance to cancer cell development and prevention of tumor growth. Other retinoids are also found to effectively reduce the proliferation of rapidly transformed cells [81].

Phosphatidylcholine and phosphatidylglycerol

Phosphatidylcholine and phosphatidylglycerol are both phospholipids and serve mainly as cellular membrane components. The phospholipid class as a whole is the most abundant membrane lipid type making up approximately 50% of the total membrane mass in an animal cell's plasma membrane [82], where PC, together with phosphatidylethanolamine, is the most abundant one [83]. Phospholipids in general constitutes about 60% of the total lipids by number in a mammalian cell, also counting other membrane types like mitochondrial, endoplasmatic reticulum membrane, and Golgi membrane. Here, PC is also of primary significance [84]. It also participates in the formation of lipoproteins which are water soluble complexes responsible for transporting neutral, non-soluble lipids such as triacylglycerols and cholesterol through the circulation system of vertebrates [83, 85]. Thus, PC has both stationary roles in individual cells, but also serves a purpose on the organism level.

Together with PC, PG is one of the most common lipids in nature and may play a role in membrane stability due to its ability to be both a hydrogen bond donor and acceptor [86]. In most animal tissue, PG is generally present in amounts of only 1-2%, but have a higher occurrence in lung of up to 11% [87]. There it acts as a component in a surfactant mixture and is necessary to maintain regular lung function [88]. It is also involved in many membrane protein complexes [89].

Figure 15 shows the general condensation reaction between PC and PG and their fatty acid counterparts. As lipids, their structure is not constant, but will vary depending on the attached fatty acids.

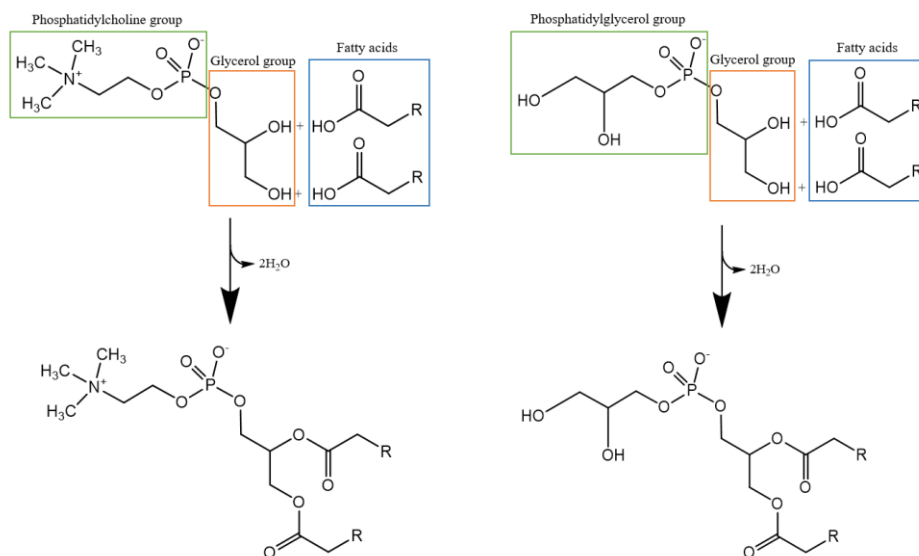


Figure 15. The condensation reaction of phosphatidylcholine (left), and of phosphatidylglycerol (right) leading in both cases to the phospholipid form. The fatty acid R-group will determine the physical and chemical properties of the molecule, such as melting temperature, hydrophobicity, and mass. Made using Cehmdraw.

1.7.1 Retinol, retinoic acid, phosphatidylcholine, and phosphatidylglycerol under the influence of electrospray ionization indicates their behavior in nano desorption electrospray ionization

When using electrospray ionization to analyze retinol, several papers [90, 91] indicate that a loss of water occurs after protonation near the OH-group. Although retinol has a molecular formula of $C_{20}H_{30}O$ and a monoisotopic mass of 286.23, the expected protonated specie of $[M+H]^+$ at m/z -value 287.24 does seldom occur. Instead, the studies show an achieved m/z value of 269 corresponding to the $[M+H-H_2O]^+$ variant. For retinoic acid, the expected ion to be observed is the protonated molecule, $[M+H]^+$, having an m/z -value of $\sim 301,4$ [92].

For PC and PG, the masses depend on the fatty acid chains that are attached. Assessing the most common fatty acids in these two phospholipids is difficult, as composition varies with species. However, PC often occurs as lecithin, which is a mixture of several types of glycerophospholipids and other substances. A study on the composition of soybean lecithin found that the fatty acid composition was predominantly constituted by linoleic acid (18:2), palmitic acid (16:0), and oleic acid (18:1) [93]. For PG, one study found that most of the fatty

acids in lung phosphatidylglycerol from pig, cow, rabbit, and guinea pig were palmitic acid (16:0, 27-37%), oleic acid (18:1, 24-37%), and stearic acid (18:0, 15-21%) [94].

Table 3 gives the monoisotopic masses for PC and PG with these most common fatty acids.

Table 3. The monoisotopic masses of PC and PG with the hypothetically most common fatty acids, and their molecular formulas. These values can be used to predict what m/z -values might be relevant and show up in a mass spectrum when analyzing these analytes.

Carbon and double bond count	Phosphatidylcholine (molecular formula)	Phosphatidylglycerol
16:0/16:0	733.5621 (C ₄₀ H ₈₀ NO ₈ P)	721.5020 (C ₃₈ H ₇₄ O ₁₀ P)
16:0/18:0	761.5935 (C ₄₂ H ₈₄ NO ₈ P)	749.5333 (C ₄₀ H ₇₈ O ₁₀ P)
16:0/18:1	759.5778 (C ₄₂ H ₈₂ NO ₈ P)	747.5176 (C ₄₀ H ₇₆ O ₁₀ P)
16:0/18:2	757.5622 (C ₄₂ H ₈₀ NO ₈ P)	745.5020 (C ₄₀ H ₇₄ O ₁₀ P)
18:0/18:0	789.6248 (C ₄₄ H ₈₈ NO ₈ P)	777.5646 (C ₄₂ H ₈₂ O ₁₀ P)
18:0/18:1	787.6091 (C ₄₄ H ₈₆ NO ₈ P)	775.5489 (C ₄₂ H ₈₀ O ₁₀ P)
18:0/18:2	785.5935 (C ₄₄ H ₈₄ NO ₈ P)	773.5333 (C ₄₂ H ₇₈ O ₁₀ P)
18:1/18:1	785.5935 (C ₄₄ H ₈₄ NO ₈ P)	773.5333 (C ₄₂ H ₇₈ O ₁₀ P)
18:1/18:2	783.5778 (C ₄₄ H ₈₂ NO ₈ P)	771.5176 (C ₄₂ H ₇₆ O ₁₀ P)
18:2/18:2	781.5622 (C ₄₄ H ₈₀ NO ₈ P)	769.5020 (C ₄₂ H ₇₄ O ₁₀ P)

When analyzing organoids or other model organisms looking for phospholipids such as PC or PG using an MS, these masses can be used to predict their expected m/z -values. For positive mode ionization, protonation is expected, and this proton must also be considered. However, there is a self-presenting problem when analyzing lipids. After acquisition of m/z -values, assigning the correct length and saturation of fatty acid chains is impossible unless a tandem MS is used. As can be seen from **Table 3**, PC(18:0/18:2) has the same monoisotopic mass as PC(18:1/18:1) because of their isomery. The same can be seen when comparing PG(18:0/18:2) to PG (18:1/18:1). Therefore, unless tandem MS is used to characterize the lipids according to their fragments of fatty acid chains, these lipids are often given with their total fatty acid chain carbon content, as well as the total number of double bonds, such as PC(36:2) or PG(36:2).

Because PG only has a negatively charged phosphate group, negative mode ionization is the natural choice. One study that analyzed 2 pmol/μL standard solutions of PG in negative mode MS found the following m/z -values for the $[M - H]^-$ ion of PG. A flow rate of 1 μL/min and a

voltage of 4.5 kV was used [95]. These results are given in **Table 4** and indicate that negative mode works best for this analyte.

Table 4. m/z-values detected by MS-analysis of 2 pmol/ μ L PG standards at 1 μ L/min and 4.5 kV voltage [95].

PG(16:0/18:1)	PG(18:1/16:0)	PG(16:0/18:2)	PG(18:0/18:1)	PG(18:1/18:0)	PG(18:0/20:4)
747	747	745	775	775	797

As to the authors knowledge, retinol, retinoic acid, phosphatidylcholine and phosphatidylglycerol have not yet been analyzed from organoids using nano DESI-MS. However, knowing how they behave in an ESI process is productive in predicting their ionization behavior when conducting organoid imaging analyses, because, as described in **section 1.5**, the ionization process is thought to be similar.

1.8 Hepatic stellate cells and gastruloids can be used as model organisms

In **section 1.1.2** model organisms were touched on, and organoids were thereafter stated as an interesting model to study. Although the nano DESI platform can be used for future organoid analysis and further development of them as a model, other models are easier to study when validating its working principles. One such model is hepatic stellate cells (HSC). These are derived from induced pluripotent stem cells (iPSC) and mimic the function of stellate cells in the liver. The cells are dormant in homeostasis, but are activated upon liver damage by, e.g., virus attack and other damaging events. When activated, they produce and secrete an extracellular medium that works as temporary scars protecting from further damage. These cells also have the largest reservoir of retinol among all cells in the human body [96], which, together with other retinoid analogues are released upon activation. This activation can be done in vitro by addition of transforming growth factor beta (TGF- β). The exact mechanism with which this happens, and whether retinol release is the cause or the effect of an activation process is unclear [97]. Because of the high abundance of retinol, these cells can be used as test cells to verify the working principles of the nano DESI platform when testing on biological samples.

Gastruloids are another aggregate of cells that may be studied as a model organism. They are a type of embryonic organoid, grown from embryonic stem cells (ESC), to mimic mammalian embryos [98]. They serve as an alternative to animal models, and manages to recapitulate the complexity and multi-layered nature of a real embryo in its developmental processes for in vitro studies [99].

2 Aim of study

A functional nano desorption electrospray ionization platform will be built, and proof of function established to explore how imaging can be used for further development of organoids, gastruloids, and other biological models.

The most important aim is building the platform, involving the elements listed in **Table 5**.

Table 5. The table lists the necessary parts of a functional nano DESI platform, as well as other factors that are used for optimization and testing at the various steps.

Component	Use	Planned included/used in this thesis
Base	Creating the space onto which other components are attached	Yes
Primary capillary emitter	Electrically conductive emitter for delivery of desorption solvent onto sample	Yes
Nanospray capillary emitter	Pick-up of solvent containing analyte for delivery to the MS	Yes
Micro positioners	Fine positioning of emitters	Yes
Microscope cameras	To ensure correct and optimal emitter position	Yes
Sample holder	A frame where glass slides containing sample is put	Yes
Motorized stages	Electrical and programmable stages to move the sample in a predetermined pattern in all three axes	Yes
Control software for sample holder	A computer program to give the three stages instructions on where to move	Yes
Height adjusting mechanism	To ensure constant probe-to-sample distance for optimal results	Yes
Imaging conversion software	Software to convert all the acquired mass spectra to a single image	Yes
Chemical standards	To do testing of the platform at each point of development	Yes
Cellular samples	To test whether the system, when ready, can desorb analytes from cells (organoids, gastruloids, etc.)	Yes

Besides building of the source, identification of retinol, retinoic acid, phosphatidylcholine, and phosphatidylglycerol in liquid samples will be done to establish the results expected from cellular samples. Imaging of cell samples will thereafter be tried.

The work in this project can be summarized as the graphical abstract given in **Figure 16**.

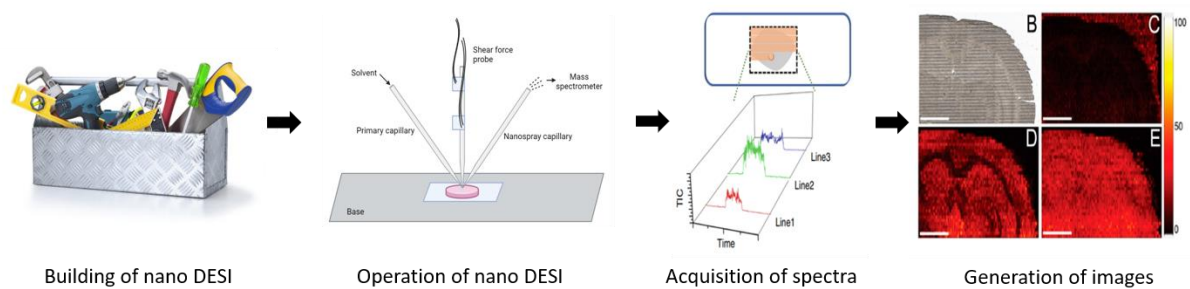


Figure 16. The process of this thesis will follow this workflow. The instrument will first be built, before being used in scanning of cell samples and generation of images.

3 Experimental

3.1 Reagents and solutions

Hydrofluoric acid (HF/H₂O, 49/51%, w/w), calcium carbonate (saturated solution), tin chloride (SnCl₄), retinol (synthetic, ≥ 95% (HPLC)), retinoic acid (synthetic, ≥ 98% (HPLC)), phosphatidylcholine (egg yolk, ≥ 99%), and phosphatidylglycerol (> 99%) were purchased from Merck (Darmstadt, Germany). Type II water was produced using a Merck Elix Advantage 15 (Darmstadt, Germany). Methanol (MeOH) AnalaR (≥ 99.8%), LC-MS grade water (H₂O) and LC-MS grade methanol (MeOH) were purchased from VWR international (Oslo, Norway). Chemicals related to MALDI imaging of gastruloids are given in **appendix 7.10**.

Ingrid Wilhelmsen (Hybrid Technology Hub, University of Oslo) prepared hepatic stellate cells for analysis using nano DESI. Sergei Ponomartcev (Institute of basic medical sciences, University of Oslo) prepared blocks of gastruloids for analysis using MALDI-TOF imaging.

3.2 Consumables and hardware

Polyimide coated fused silica capillary tubes (360 μm OD, 5, 10, and 50 μm ID) were purchased from Polymicro Technologies (Phoenix, AZ, USA). Polyether ether ketone (PEEK) tubing (0.005" and 0.01" ID, 1/16" OD), PEEK screw (1/16" ID), and stainless-steel union (1/16" bolt thread), PEEK union (1/16" ID) with compatible graphite ferrules, stainless steel union (C360UFS2), nut and ferrule (C360NFFS), and six-port valve were purchased from VICI Valco (Schenkon, Switzerland). Facial tissues were purchased from VWR (Oslo, Norway). Automatic pipette (1-100 μL) was purchased from Eppendorf (Hamburg, Germany). Lighter was purchased from a convenience store (nummer1lighter, manufactured by Imperial Tobacco Norway, Oslo, Norway). Capillary cutter was purchased from G&T Septec (Ski, Norway). Formlabs' Clear resin for 3D-printed cups was purchased from Formlabs (Boston, MA, USA). Emitter stand was made in-house. SGE syringes (250 μL and 1mL) were purchased from Trajan

(Melbourne, Australia). Nanoviper tubing (6041.5260, 20 μm ID, 550 mm length) were purchased from Thermo Fisher Scientific (Waltham, MA, USA).

Aluminum 10x20x30 cm cuboid base was made in-house. Nanospray FlexTM ion source was purchased from Thermo Scientific (Waltham, MA, USA). Two inline micro-positioners with micrometers (model XYZ 500 MIM), one motorized inline micro-positioner (model XYZ 500 MIMT), and one microstepping controller (cat. no. 20411) were purchased from Quater research and development (Bend, OR, USA). Four articulating arms (model 2158 universal magic arms) were purchased from SmallRig (Shenzhen, China). Alligator clips and a sample slide holder were 3D-printed in-house. Dual-phase lock-in amplifier with rack mount kit (model SR 865A) was purchased from Stanford research (Sunnyvale, CA, USA). Ultra-flexible microminiature PTFE hook-up wire (cat. no. 2452/30) was purchased from Daburn (Dover, NJ, USA). Piezo ceramic plates (3x3x0.55mm, cat. no. SMPL3W3T05410) was purchased from STEMiNC (Davenport, FL, USA). Silver conductive epoxy adhesive (product no. MR3863) was purchased from Loctite (Westlake, OH, USA). 50 mm travel motorized stage (model T-LSM050A-KT03), 25 mm travel motorized stage (model T-LSM025A), and 25 mm travel motorized stage (model LSM025A-T4-MC04) were purchased from Zaber technologies Inc. (Vancouver, BC, Canada). Microscope slides (product no. 631-1550) were purchased from VWR (Oslo, Norway). Four optical post (76.2 mm height, M-TSP-3), two optical post (50.8 mm height, M-TSP-2), two adjustable angle post clamp (8 mm diameter, MCA-1), right-angle post clamp (8 mm, MCA-1), and two optical post holders (1.75", MSPH-1.5) were purchased from 4Photonics (Mölnlycke, Sweden). Two Dino-Lite microscope holders (model HD-P1) were purchased from Dino-Lite (Almere, The Netherlands).

3.3 Instruments

Etching apparatus made in-house. Formlabs Form 3B 3D-printer purchased from Formlabs (Boston, MA, USA). ALD-reactor made in-house. EASY-nLCTM 1200, Q ExactiveTM Plus Hybrid Quadrupole-OrbitrapTM, Nanospray FlexTM ion source, and a heated electrospray ionization source were purchased from Thermo Scientific (Waltham, MA, USA). Two Dino-Lite cameras (model AM4012PTL) were accessories following mass spectrometric instrumentation. Syringe pump (model Fusion 101) was purchased from Chemyx Inc. (Stafford,

TX, USA). Cryostat (CM 1860UV) were purchased from Leica Biosystems (Deer Park, IL, USA). M3+ sprayer was purchased from HTX Imaging (Chapel Hill, NC, USA).

3.4 Software

Xcalibur™ was purchased from Thermo Scientific (Waltham, MA, USA).

3.5 Etching of capillary emitters

Production of the capillary emitters was done according to procedure previously developed by Zhu et. al. [67], and further improved by Stian Kogler [69]. These procedures will be further explained in this section.

Capillary tubes of 360 μm OD and of both 5 μm and 10 μm ID were cut in 10-15 cm lengths and a portion of the polyimide layer was burned away using a lighter creating a 0,5-1 cm window near one of the ends. The soot was dried off using a paper tissue and methanol, exposing the inner silica.

A model of a small plastic cup was made and 3D-printed by principal engineer Inge Mikalsen using Formlabs' Form 3B printer and their clear resin. The cup had a bridge with an orifice in the opening, and a hole at the bottom. **Figure 17** shows the model for this cup.



Figure 17. Model of an etching cup made using 3D-printing. Made by Inge Mikalsen. The bridge arcs over the opening of the cup and contains an orifice that aligns with the bottom hole, both through which the capillary is threaded during etching. The cup measures 5,2 mm in height, and 4,9 mm at its widest diameter. The cups are made using the Clear Resin from Formlabs.,

After printing, the hole in the bottom was drilled out using a 0,350 mm bore, as this was too small of a feature for the printer to include fully and accurately.

The capillary was threaded through the cup. The end of the capillary farthest away from the exposed window was threaded first through the bottom hole, and then the bridge orifice. The capillary was threaded until the cup was entirely within the exposed window. It then rested on the bottom of the window, where the polyimide layer began. The upper part of the capillary was threaded through a PEEK-tube fastened to a PEEK-screw and screwed into a stainless-steel union. The screw with the capillary inside was tightened to make the two hang together.

The capillary was hung in a designated apparatus, previously made by principal engineer Inge Mikalsen according to Zhu *et. al.*'s design. This apparatus, consisting of a steel base plate, two poles, and a plastic bracket for holding the PEEK-screws, allows in total 12 capillary tubes to hang in a vertical fashion. **Figure 18** shows this setup.

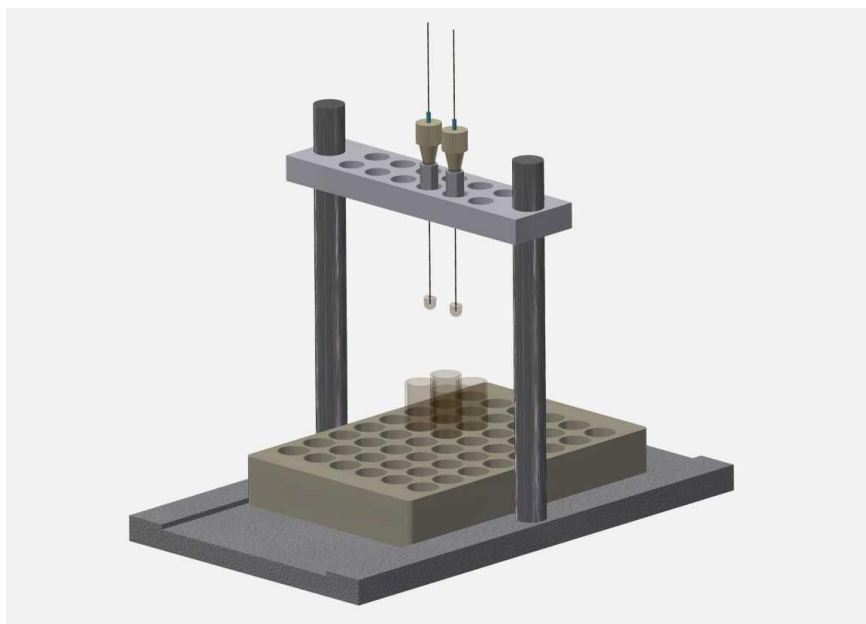


Figure 18. The etching apparatus as made by principal engineer Inge Mikalsen. Two poles holding the bracket was attached to a base steel plate. The capillary tubes were attached using the PEEK-tubes, and the capillaries with their attached cups hang over collection tubes to catch the falling part of the capillary and the cup. Reproduced from “On-line “Organ-in-a-column” liquid chromatography electrospray ionization mass spectrometry for drug metabolism studies” [69]. In the actual experiment a bigger bath is used instead of individual containers.

When hanging, 30 μL HF was pipetted to the cups. When the etching was finished, the capillaries were sprayed with water to rinse off remaining HF and other impurities before being stored in a closed container with the tips suspended in free air.

All emitters were inspected in a 4x magnification light microscope after etching. Their geometrical shape and size were assessed with respect to their symmetry, outer diameter at the tip, length of thinned part, and slope of thinning. Inspection was solely visual, and no calculations were involved.

3.6 Atomic layer deposition to make emitters electrically conductive

The emitters were coated with tin oxide (SnO_2) through ALD. The etched emitters were loaded on an in-house made aluminum stand in a manner that allowed most of the emitter length, including the tip, to be suspended in free air. The emitter stand was put in a larger glass tube. **Figure 19** shows how emitters were mounted in the stand prior to deposition.

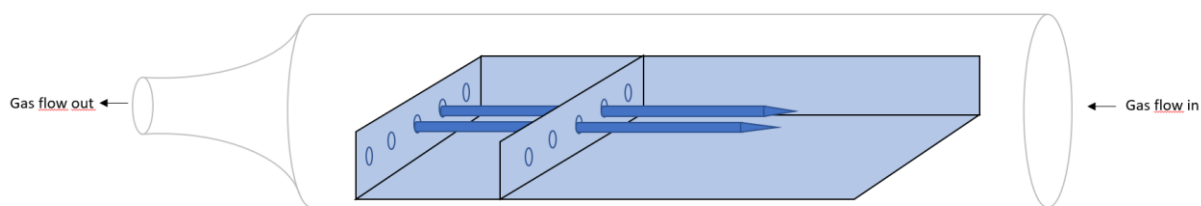


Figure 19. An illustration of the ALD setup. Etched emitters were mounted in an aluminum stand with holes drilled into it. This stand was placed in a glass bottle with a constriction in the gas flow outlet. The glass bottle with the stand was placed in the ALD reactor, followed by subsequent cyclical introduction of reactants.

The stand and glass tube were then put in the ALD reactor, which consisted of a vacuum chamber with surrounding heating elements. The reservoirs for the precursors were opened one at a time, and the vacuum in the chamber forced the precursors to evaporate from liquid form and introduced sequentially.

After proper installation of the stand, the deposition was initiated. SnCl_4 and H_2O was chosen as precursors to form the SnO_2 layer. **Table 6** shows the cyclic procedure, and is based on previous work by Stian Kogler who optimized this method [69].

Table 6. The table shows the order of events including introduction of reactants and purging in between. The time for each event is given in milliseconds.

Precursor/purge	SnCl_4	Purge line	SnCl_4	Purge chamber	reactor	Water pulse	Purge line	water	Full purge
Time (ms)	1000	500		2000		2000	500		2000

This cycle repeats 4000 times. The flow of each reactant was split in two; one of 150 mL/min to bring reactants to the chamber, and one of 75 mL/min to make sure the reactants stay in the reactor and don't leak out to the rest of the system. A temperature of 400°C was used.

3.7 Examination of emitters in electrospray ionization

Emitters having undergone ALD coating were tested to see if a nano ESI spray could be produced. Emitters were coupled to a Thermo EASY-nLC 1200 nano LC pump system and

installed in a Nanospray Flex open ESI source. The coupling was done using Valco steel unions between the pump and the emitter. Both mobile phase solution A and B were a 9:1 methanol water mixture, ran in a 50/50 isocratic manner. Voltage was set to 3 kV, and the flow rate was set to 300 nL/min. Only the pure mobile phase solutions were injected.

The TIC variation and the AGC target were noted and used as parameters for emitter quality.

3.8 Preparation of analyte standards

Powder of retinol (25 mg), retinoic acid (50 mg), and phosphatidylcholine (25 mg) were dissolved in each their own methanol solution. Phosphatidylglycerol (25 mg) was dissolved in water. For retinol, retinoic acid, and phosphatidylcholine the target concentrations were 300 ng/mL. For phosphatidylglycerol, the concentration was 250 ng/mL. All four solutions were diluted to a 9:1 mixture of methanol and water at their end concentrations.

For the full dilution series, see **appendix 7.6**.

3.9 Direct infusion using a commercial heated electrospray ionization source

Analytes were infused to the Orbitrap MS through heated ESI (HESI) source using a syringe and a syringe pump. Voltage was set to 3.0 kV for positive ionization (retinol, retinoic acid, and phosphatidylcholine), and 2.5 kV for negative mode ionization (phosphatidylglycerol). The flow was set to 5 μ L/min for the analytes run in positive mode, and 10 μ L/min for negative mode

3.10 Comparison of etched emitters to a commercial electrospray ionization spray interface

Direct infusion was carried out by using a six-port valve system to connect the nano LC pump to the emitters, with a sample loop installed to hold the standard sample being infused. **Figure 20** shows the setup.

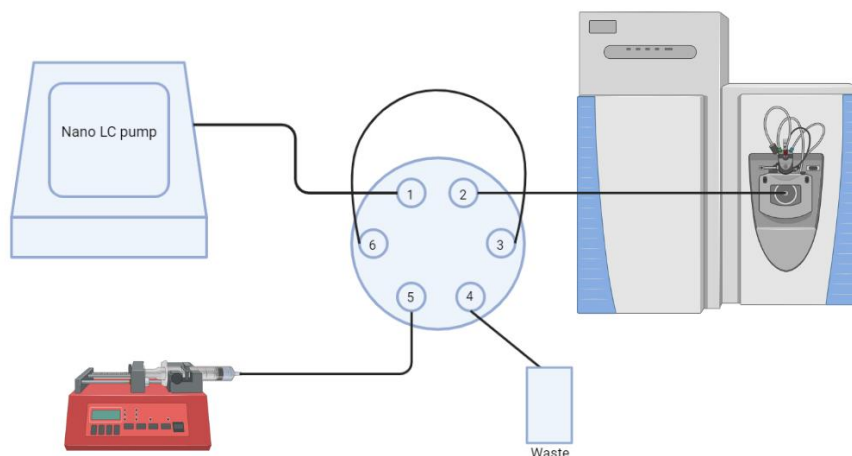


Figure 20. A nano LC pump is connected to a six-port. When in the 1-2 position, the flow from the pump is directed directly to the MS and sample can be loaded in the loop using a syringe. When in the 1-6 position, the flow from the pump goes through the loop, pushing the loaded sample to the MS for detection. Made using BioRender (biorender.com)

The syringe was filled with 100 μL analyte solution and coupled to the port, and the syringe pump started. The sample loop was filled with analyte solution in the 1-2 position. Infusion to the MS happened after turning the port to the 1-6 position, and detection was undertaken.

For these infusions, a flow rate of 500 nL/min was used. Both mobile phase reservoirs were filled with a 9:1 MeOH/water solution, and the isocratic flow was run 50/50 A/B split. Analyte concentration was as given in **Table 22** in **appendix 7.6**. 3 kV of positive voltage was used in positive mode ionization (retinol, retinoic acid, phosphatidylcholine) while 2.5 kV was used for negative ionization (phosphatidylglycerol).

3.11 Assembly of the nano desorption electrospray ionization instrument platform

The nano DESI was assembled according to the protocol published by Yin et. al. [50]. For this assembly, several of the university's workshops and laboratories were consulted. Inorganic materials chemist Ola Nilsen was consulted to help in the ALD process, and the use of his home-made reactor. A hardware workshop helped supply the necessary aluminum framework and other necessary metal components. Terje Grønås at the electronics laboratory helped in configuring the sample holder stage and the involved electronics. In addition, a laboratory at the Hybrid technology hub, Faculty of Medicine, UiO helped prepare and supply the cellular samples to be analyzed. Principal engineer Inge Mikalsen helped with the practical drilling of holes, screwing of screws, and 3D-printing of various necessary parts.

3.12 Direct infusion between emitters to verify an established liquid bridge

An etched 50 μm ID NCE of about 2-3 cm length was mounted in its designated crocodile clip. After adjusting its position to about one millimeter from the MS inlet, a 10 μm ID PCE was connected via a Valco union to the nano LC pump and mounted in the crocodile clip. Aligning of the capillaries was done using the manual micro positioners. The flow was set to 200 nL/min. The voltage supply was also connected to the PCE. 3.5 kV was used for positive ionization, and 3 kV for negative ionization. Two Dino-lite cameras were set up and used to observe the droplet exiting the PCE. When the emitters were aligned, a very small droplet was visible, namely the liquid bridge. Xcalibur was used to look for specific characteristics in the mass spectrum indicating a formed liquid bridge. Direct infusion of analytes was thereafter done. The same six-port system as shown in **Figure 20** was used. The loop was filled in the 1-2 position, and rotation to the 1-6 position started the infusion.

3.13 Desorption of analytes from a glass slide

A 50 μm ID NCE and 10 μm ID PCE was used. The pump flow was set to 200 nL/min, with 9:1 methanol:water solution in reservoir A and B in 50/50 isocratic manner. A 1x1 cm square was made by applying clear tape to a glass slide, and two drops of analyte solution were applied within the square. The sample holder was lifted, and analytes were desorbed from the droplet. Voltage was set to 3.5 kV for positive mode, and 2.5 kV in negative mode.

The sample holder motors were manually controlled, and not program controlled. Continuous movement in the x-direction was started, while the height was continuously adjusted to keep a constant probe-to-sample distance.

3.14 Analyte desorption from hepatic stellate cells

Analytes were tried desorbed from HSC supplied by the Hybrid technology hub, Faculty of Medicine, UiO, derived from human induced pluripotent stem cells derived WTC-11 cells. The cells were embedded on a glass slide, and three different groups of cells were analyzed: one control group, one that were starved of retinol, and one that had added 25 ng/mL transforming growth factor beta (TGF- β). A 50 μm ID NCE and 10 μm ID PCE, a flow rate of 200 nL/min, and a voltage of 3.5 kV in positive mode were used. Only retinol was tried desorbed.

In addition, gastruloids were imaged by using MALDI imaging. For the preparation procedure of these samples, see **appendix 7.10**.

3.15 Finding masses and molecular formulas using databases

3.15.1 Chemcalc.org

Before an analysis, the molecular formula of a substance was entered to get the monoisotopic mass. Mode of ionization, e.g., H^+ , was also entered. After an analysis, the m/z -value of the mass spectrometric peak assumed to have the monoisotopic mass was typed in, along with the

mass accuracy, mode of ionization, and the number of atoms of different elements expected to be in the molecule. A list was then given by the website of possible molecular formulas, along with a mass accuracy value in ppm.

When trying to find the correct molecular formula based on a peak suspected to be a PC variant, only the molecular formulas containing one nitrogen, eight oxygen, and a phosphor were evaluated. Likewise, for PG, only those containing ten oxygen and a phosphor were evaluated. This would drastically reduce the number of alternatives.

3.15.2 Pubchem and chemspider were also used as databases to annotate mass spectrometric signals

When looking at different possibilities of phosphatidylcholine and phosphatidylglycerol type substances for a detected m/z signal, pubchem was used as a database to verify the molecular formula given by chemcalc when typing the m/z -value. Chemspider was also used to find different isomers of some of the oxidated retinoid variants found in some analyses.

4 Results and discussion

4.1 Etching of emitters proved successful

Emitters usable for high-resolution nano DESI imaging experiments were made. After production, they were inspected in a 4x magnification microscope and pictures were taken. Overall, there was somewhat of a variation in length and slope of thinning after etching, but all emitters were satisfying in their geometry. Therefore, all emitters were promoted to ALD.

Figure 21 shows four arbitrarily chosen emitters from the first batch of 10 emitters.

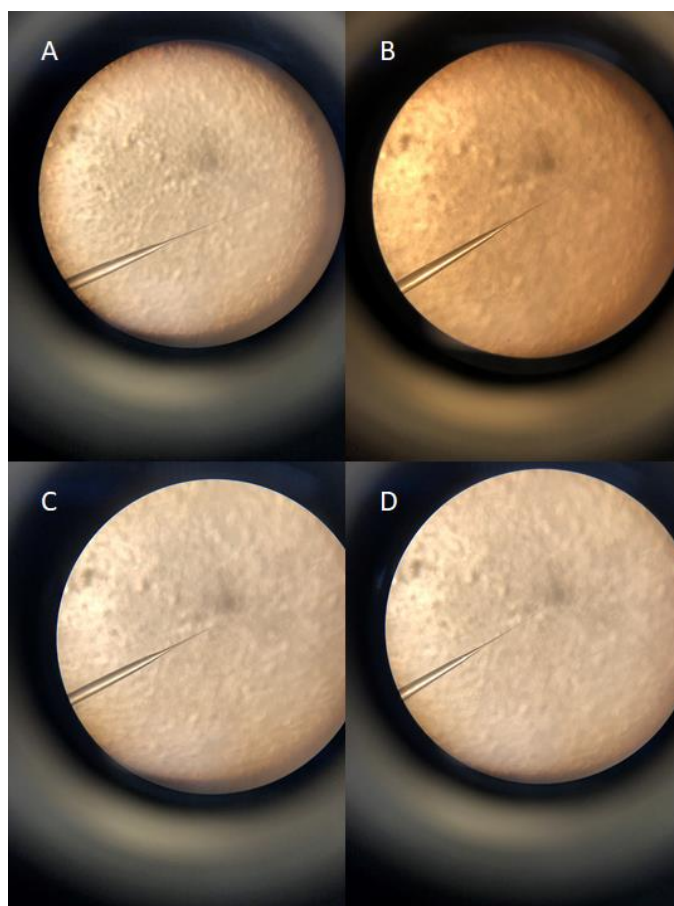


Figure 21. Four arbitrarily chosen emitters out of a batch of ten. Emitters A and B are 5 μm ID. Emitters C and D are 10 μm ID. They're individually symmetric, and their geometry is similar when cross-comparing.

The use of 3D-printed cups seems to eliminate previous concerns regarding identity of emitters, as the cups themselves are similar in geometry and weight. An average weight of 26.4 mg and standard deviation of 0.5 mg for one batch of emitter cups was measured, meaning the

point of etching termination should be within 2% of the total etching time given all other parameters are the same for emitters of the same ID.

Using pulling, the other most common way to produce emitters in-house, 90 minutes is needed to make one PCE and one NCE [100]. Using etching, emitters were collected the day after the etching was started, making same-day experiments with nano DESI unfeasible, especially when taking the ALD process into account. However, for mass production of emitters, this is a good method as several emitters can be made simultaneously, and has scale-up potential in both the etching and ALD.

Emitters were geometrically satisfying, and were promoted to ALD.

4.2 Atomic layer deposition of emitters gave stable electrospray

To verify that a layer of conductive SnO₂ had been laid, emitters were coupled to the nano LC pump and tested in a Nanoflex open ionization source as described in **section 3.7**. According to theory in **section 1.2.4** a TIC variation of under 10% and an AGC target of 100% is desirable for the QExactive Orbitrap. Therefore, these values are used as guidelines for the quality of the emitters. The lower the TIC variation, the better. The AGC should always be at 100%.

In the spray test, 14 out of 20 emitters achieved ESI spray. The remaining 6 was either unable to achieve spray, was presumed clogged due to an increasing pressure in the pump and no liquid coming out the tip, or broke during preparation due to careless handling. For interested readers, the signal intensity, TIC variation, and AGC target of the 14 successfully working emitters are found in **appendix 7.8**.

The emitters all had a signal intensity between 5E6 and E8. Large deviations should be noted when using an emitter at two different experiments. Only one emitter passed the 10% TIC variation threshold of acceptability and could have been used for routine analysis. Three other emitters had varying TIC variation and was sometimes within the threshold, but sometimes not. A high TIC variation may arise from disturbances in the flow through the emitters, caused, e.g., by a non-uniform emitter inside or tip. Irregular voltage supply caused by uneven ALD at the

sub-micrometer level may also be a potential source of TIC variation. Stability tests may be productive. This has largest implications for quantitative analyses but will matter less for qualitative analyses.

For all emitters, the AGC was 100%. This means the orbitrap is being fed the number of ions that it needs to operate functionally. For a low absolute ion intake this value will be less and would be the case if there was a clogging in an emitter, for instance. An emitter achieving a value less than 100% should not be used in nano ESI or nano DESI experiments.

In this test, the voltage was applied very close to the tip of the emitters. Therefore, the emitters had to be cut to about 3,2-3,5 cm in length. Any longer, and the voltage would be applied too far back on the emitter, and neither Taylor cone nor spray would be achieved. Any shorter, and handling of the emitter would become difficult. This gives a strict requirement for the emitters, and different placement of the voltage source may give different results depending on the electrical field generated. The emitters should therefore be cut with care.

14 out of 20 emitters were able to produce electrospray, had satisfying signal intensity and AGC target, but varying TIC variation. Stability tests should be discussed before commencing high-resolution imaging experiments. Emitter fragility strongly requires ease of care.

4.3 Direct infusion of retinol, retinoic acid, phosphatidylcholine and phosphatidylglycerol showed their behavior in electrospray ionization

To have a better understanding of the analyte mass spectra before using the in-house made emitters or the nano DESI platform, standards of retinol, retinoic acid, phosphatidylcholine and phosphatidylglycerol were prepared and directly infused into the QExactive MS instrument using HESI. Specifically, the m/z -values of the analytes and their different adducts as well as their isotope patterns wanted to be characterized. This would make later analyses using the nano DESI more predictable.

The preparation of analyte solutions was suboptimal, and the end concentrations were not quantitatively reliable due to several transfers and large dilution steps. For the solution of

retinoic acid, a miscalculation was made making this solution even less reliable, giving it a concentration of 600 ng/mL instead of 300 ng/mL. This mishap also affects all the later infusions. See **appendix 7.7** for a further discussion on this.

During these and all later infusions, chemcalc.org was used in three ways: finding the anticipated monoisotopic mass based on a known molecular formula, calculating the isotope distribution pattern, and finding the molecular formula of the detected m/z -values with their corresponding mass accuracies. This was used especially frequently when evaluating different types of phosphatidylcholine and phosphatidylglycerol.

4.3.1 Retinol

In **Figure 22**, the mass spectrum of a 300 ng/mL retinol solution is shown.

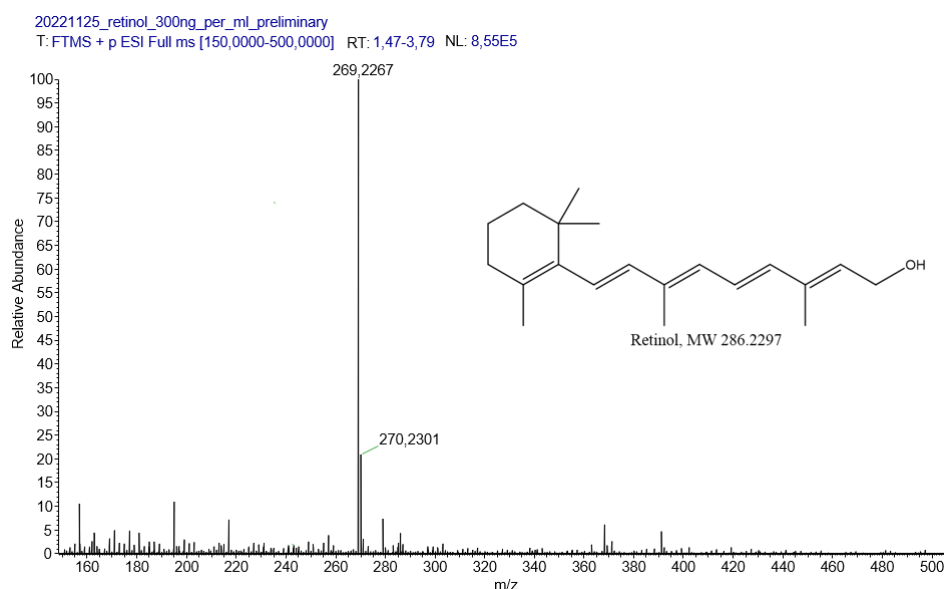


Figure 22. Mass spectrum of retinol. The peak at m/z 269,2267 is the $[M+H-H_2O]^+$ adduct of the molecule. The peak at m/z 270,2301 is an isotope variant of the retinol peak.

The base peak of m/z 269.2267 corresponds to the expected mass of the protonated molecule, minus a water molecule, i.e., $[M+H-H_2O]^+$. This is in accordance with theory given in **section 1.7.1**. Therefore, the ion detected is what should be looked for when analyzing for retinol. Its ^{13}C isotope peak is also visible at m/z 270.2301. Evidently, the $[M+H]^+$ variant at nominal mass

287 is not an ion to look for in HESI experiments, and therefore neither in later nano DESI experiments.

4.3.2 Retinoic acid

After direct infusion of a 600 ng/mL solution, the mass spectrum in **Figure 23** was obtained.

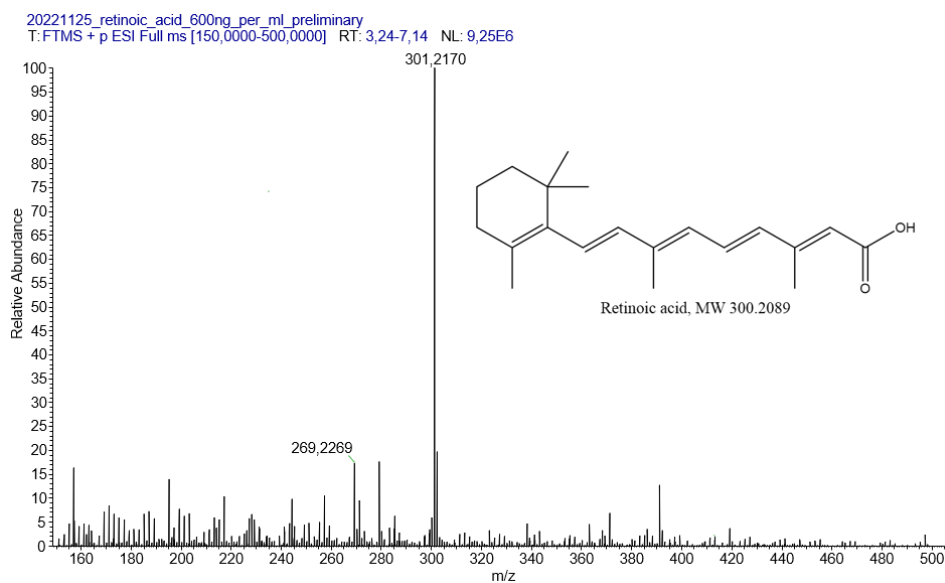


Figure 23. Mass spectrum of direct injection of 600 ng/mL retinoic acid. The base peak at m/z 301.2170 corresponds to the $[M+H]^+$ ion. The peak at m/z 302.2203 corresponds to the ^{13}C isotope peak. A peak at m/z 269.2269 was also seen, which has the same m/z value as protonated retinol having lost a water molecule. A possible reduction might have occurred.

The base peak of m/z 301.2170 corresponds to the protonated $[M+H]^+$ variant of retinoic acid. This is in accordance with theory given in **section 1.7.1**. Its ^{13}C isotope peak at m/z 302.2203 can also be seen. In addition to this, a peak occurs with m/z 269.2269 corresponding to retinol. This may be an indication that some retinoic acid undergoes a reduction, before being detected as protonated retinol having lost a water molecule. Therefore, retinol may also be an analyte to look for when analyzing for retinoic acid. Comparing to the previous mass spectrum, this does not go the other way.

4.3.3 Phosphatidylcholine

Phosphatidylcholine was directly infused in a concentration of 300 ng/mL. **Figure 24** gives the mass spectrum acquired.

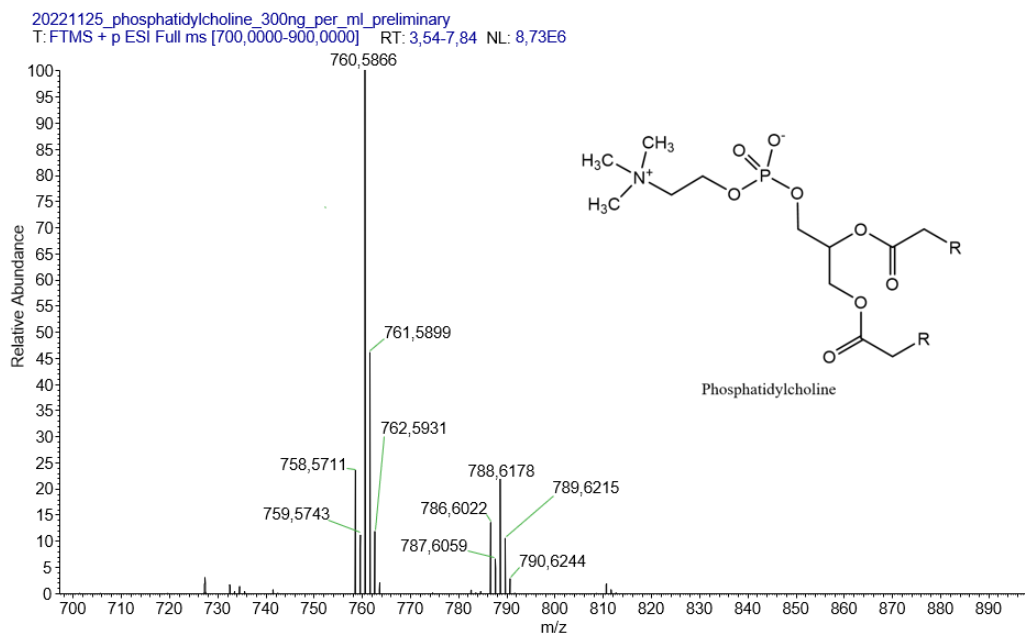


Figure 24. Mass spectrum of direct infusion of 300 ng/mL phosphatidylcholine. Two clusters of peaks appear, around m/z 760 and 788, both having a very similar distribution of peaks. The base peak at m/z 760.5866 corresponds to a PC(34:1) variant. For the higher cluster, the local base peak at m/z 788.6178 is constituted of PC(36:1).

This gave rise to a variety of peaks. An interesting division into two clusters was observed. **Table 7** below summarizes the peaks of interest, and what ions give rise to them. All ions are on the protonated $[M+H]^+$ form.

Table 7. The table provides the m/z values of peaks of interest obtained after direct infusion of a 300 ng/mL PC solution, as well as the ions thought to give rise to them.

m/z -value	Compound	m/z -value	Compound
758.5711	PC(34:2), most likely (16:0/18:1)	786.6022	PC(36:1)
759.5743	^{13}C isotope of PC(34:2)	787.6059	^{13}C isotope of PC(36:1)
760.5866	PC(34:1)	788.6178	PC(36:1), most likely (18:0/18:1)
761.5899	^{13}C isotope of PC(34:1)	789.6215	^{13}C isotope of PC(36:1)
762.5931	Double ^{13}C isotope of PC(34:1)	790.6244	Double ^{13}C isotope of PC(36:1)

The PC(34:1) $[M+H]^+$ molecule, with a molecular formula of $C_{42}H_{82}NO_8P$ was most likely a 16:0/18:1 variant, according to theory given in **section 1.7.1**. The 762.5931 peak could arguably have been a more saturated 16:0/18:0 variant with molecular formula $C_{42}H_{84}NO_8P$. This protonated $[M+H]^+$ molecule would have had an m/z value of 762.6007, but the double ^{13}C isotope of PC(16:0/18:1) had an exact mass of 762.5915 [101] which was closer to the observed value. Therefore, the 762.5931 peak was thought to belong to the doubly isotope.

The peak at m/z 788.6178 most likely belonged to the $[M+H]^+$ variant of PC(36:1), having a molecular formula of $C_{44}H_{86}NO_8P$ which was likely the protonated PC(18:0/18:1) variant. The 790.6244 peak could be thought to belong to PC(18:0/18:0) with molecular formula $C_{44}H_{88}NO_8P$, which would generate a protonated $[M+H]^+$ molecule with mass 790.6320 [101]. However, with a HRMS instrument, this is rather unlikely as the mass discrepancy between the exact mass of the isotope molecule and the observed value was smaller than between the PC(18:0/18:0) molecule and the observed value.

4.3.4 Phosphatidylglycerol

Negative mode was used for analyzing PG, as it was not detected in positive mode. The spectrum in **Figure 25** was acquired after injecting a 250 ng/mL solution.

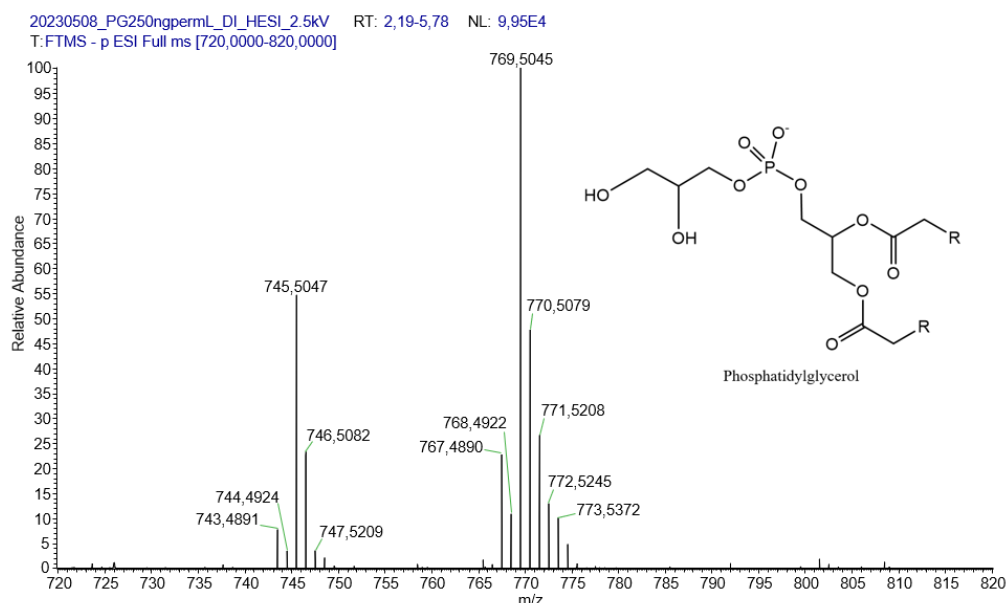


Figure 25. Mass spectrum of a 250 ng/mL solution of PG.

The signal intensity was markedly lower than for the infusion of PC. Therefore, three other solutions were injected the same way, with concentrations 500 ng/mL, 700 ng/mL, and 2500 ng/mL. The spectra and linearity of signal intensity for two chosen peaks are found in **appendix 7.9**. However, as these solutions were prepared after making the stock solution, this meant the 9:1 mixing ratio of methanol and water was no longer retained.

Two clusters of peaks appeared for PG as well. **Table 8** gives the explanation of what compound corresponds to the masses found in the spectra. All peaks are of the $[M]^-$ ion.

Table 8. The exact masses for the compounds detected from a phosphatidylglycerol solution, as well as an explanation for what compounds give rise to them. All ions were detected as the $[M]^-$ ion.

<i>m/z</i> -value	Compound	<i>m/z</i> -value	Compound
743.4891	PG(34:1)	768.4922	Isotope peak of PG(36:3)
744.4924	Isotope peak of PG(34:1)	769.5045	PG(18:2/18:2)
745.5047	PG(18:2/16:0)	770.5079	First isotope peak of PG(18:2/18:2)
746.5082	First isotope peak of PG(18:2/16:0)	771.5208	Second isotope peak of PG(18:2/18:2)
747.5209	PG(16:0/18:1)	772.5245	PG(18:2/18:3)
767.4890	PG(36:3)	773.5372	Isotope peak of PG(18:2/18:3)

Normally, assigning the exact chain length to lipids like phosphatidylglycerol would be a comprehensive task involving fragmentation of the precursor ions. However, for the solution used for PG, the manufacturer provided the relative composition of the different chain lengths present. Therefore, the correct side chains were more easily correctly assigned when analyzing PG. **Table 9** gives the relative composition [102].

Table 9. The relative abundance of the different side chains present in the solution of PG as provided by the manufacturer, Avanti Polar Lipids.

Side chain length	16:0	18:0	18:1	18:2	18:3	Unknown
Relative abundance (%)	12.4	3.6	10.5	65.6	6.3	1.5

Nominal mass spectrometric signals of interest found were 269 for retinol, 301 for retinoic acid, 760 and 788 as well as 758 and 786 for PC and 745 and 769 for PG. These values were decided as focal points for later experiments when verifying proof of function for the nano DESI and can potentially be used for cell model analyses of organoids and, e.g., HSC or gastruloids.

4.4 Direct infusion with etched and coated capillaries proved their ability to be used as electrospray emitters

After setting up the system for direct infusion as described in **section 3.10**, acquisition of mass spectra of the four analytes was carried out using three different emitters per analyte. Because of their small size and lack of compatibility with a conventional ion source, they were coupled to a nano LC pump. The nano LC and six-port system were used instead of just a syringe pump because too high a pressure from the small ID of the emitters would lead to no sample exiting the emitter.

4.4.1 Retinol

For all infusions of retinol, a 300 ng/mL solution was used. The spectra acquired using three different emitters are shown below in **Figure 26**. The top spectrum was taken using a 10 μm ID emitter, and the middle and bottom spectra were taken using 5 μm ID emitters.

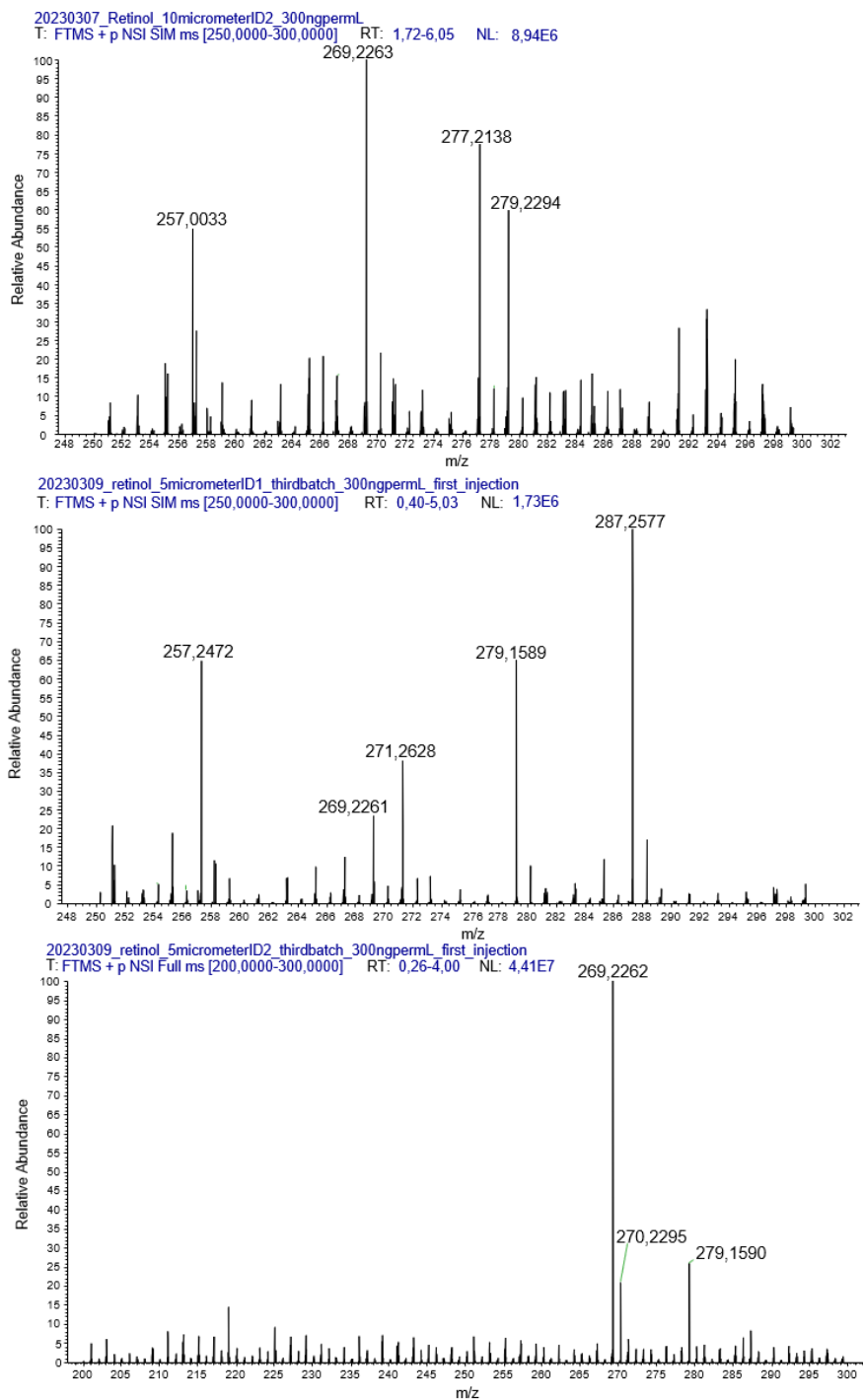


Figure 26. All spectra were acquired after infusion of 300 ng/mL retinol solution. **Top:** a 10 μm ID emitter was used. The peak at 269.2263 corresponds to the protonated $[M+H]^+$ ion of retinol. TIC variation was 5-12%. **Middle:** a 5 μm ID emitter was used. The peak at 269.2261 corresponds to retinol. This time, it was no longer the base peak. The TIC variation was 6-10%. **Bottom:** a different 5 μm ID emitter was used. This spectrum resembles what was achieved using a commercial HESI source, with retinol having a base peak at 269.2262, and an isotope peak at 270.2295. It is unclear what gives rise to the peak at m/z 279.1590. The TIC variation was 3-13%.

For the **top** spectrum taken with a 10 μm ID emitter, the peak of m/z 269.2263 corresponded, to the $[M+H-H_2O]^+$ form of retinol, as stated in **section 1.7.1** and demonstrated through direct infusions in **section 4.3.1** This was also the base peak. Several other peaks were also seen when

using this emitter, than using a commercial HESI source, as displayed in **Figure 22**. The retinol ^{13}C isotope peak was seen at 270.2296 but is not labelled. The TIC variation of this acquisition was roughly between 5-12%, which is acceptable when using a threshold of acceptability of 10%.

For the **middle** spectrum, the average signal for the $[\text{M}+\text{H}-\text{H}_2\text{O}]^+$ ion of retinol fell at only 25% of the base peak height, and at only 4.8% the intensity found in the first infusion using the 10 μm ID emitter. In addition to the low analyte signal, various peaks were seen at m/z 257.2472, 271.2628, 279.1589, and 287.2577. The m/z 279 peak was commonly observed when using plastic tubings, as it is a phthalate ester plasticizer [103]. The TIC variation of this acquisition was roughly between 6-10%.

In the **bottom** spectrum, also taken using a 5 μm ID, the base peak signal of the $[\text{M}+\text{H}-\text{H}_2\text{O}]$ retinol variant was again the most dominant. Its C^{13} isotope peak was also clearly visible at 270.2295. In addition, the plasticizer peak at 279.1590 could also be seen here. The TIC variation of this acquisition was roughly between 3-13%.

Table 10 includes the size of the dataset, average, and standard deviation for the peak signal corresponding to retinol.

Table 10. For the peaks of retinol, the size of the dataset, the average signal intensity, and standard deviation of the signal intensity is given.

n	Average signal intensity	Standard deviation of signal intensity
3	1.78E7	1.89E7

*Overall, the emitters were capable of being used in detecting retinol, although with varying intensity. TIC variations were however much better than for the spray test in **section 4.2**, and all emitters could have been used for nano DESI imaging experiments.*

4.4.2 Retinoic acid

The same 600 ng/mL solution of retinoic acid was infused three times, using the same three emitters as were used when injecting retinol: one 10 μm ID, and two different 5 μm ID ones.

Figure 27 shows the three spectra acquired.

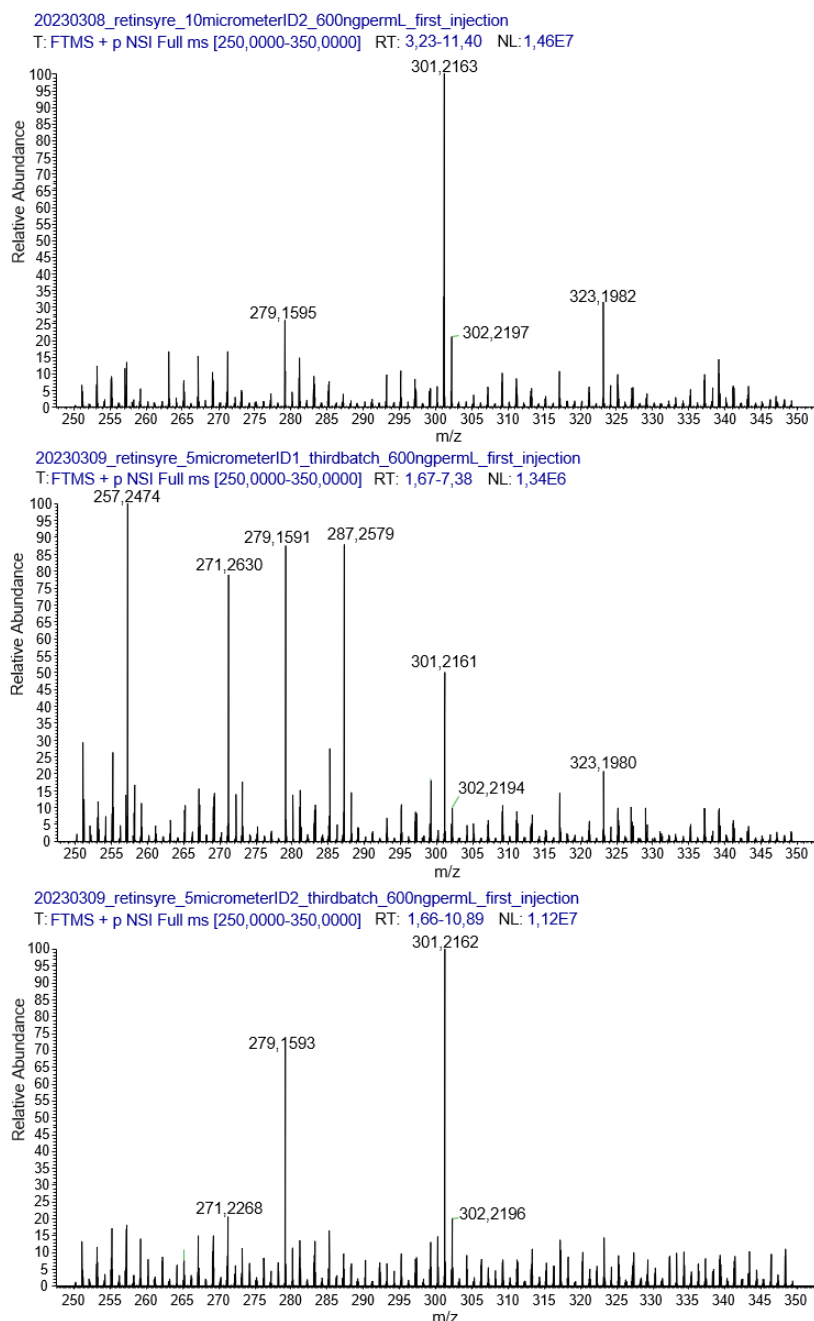


*Figure 27. The spectra acquired after infusion of a 600 ng/mL solution. **Top:** a 10 μm ID emitter was used. Retinoic acid was seen as the base peak at 301.2163, while its ^{13}C isotope peak sat at 302.2197. The peak at 323.1982 was an $[\text{M} + \text{Na}]^+$ sodium adduct. The TIC variation was 5-30%. **Middle:** In this infusion, the retinoic acid peak is only around 6.7E5 signal intensity. This is roughly 4.6% of the intensity achieved in the first infusion. The TIC variation for this infusion was 10-20%. **Bottom:** This emitter shows the highest signal intensity for retinoic acid at m/z 301.2162. Again, we see the peaks at 279 and 271 as we did in the second infusion. The TIC variation for this infusion was 8-13%.*

For the **top** spectrum, the base peak at m/z 301.2163 belonged to the $[M+H]^+$ variant of retinoic acid, as stated in **section 1.7.1** and previously confirmed with direct infusion in **section 4.3.2**. Its ^{13}C isotope was found at m/z 302.2197. Its $[M+Na]^+$ sodium adduct was also seen with an m/z of 323.1982. Comparing this spectrum to the first infusion with this emitter when analyzing retinol (**Figure 26**), there seemed to be fewer impurities. The TIC variation of this acquisition was roughly between 5-30%, which may indicate some instability in the electrospray.

In the **middle** spectrum for the second infusion, the signal intensity of protonated retinoic acid was greatly reduced to about 50% base peak signal intensity, and to only about 4.6% when compared to the first infusion. Its peak at m/z 301.2161 was however still seen, as well as its ^{13}C isotope peak and the $[M+Na]^+$ peak at m/z 323.1980. The other peaks were all similar to those occurring using the same emitter when injecting retinol (**Figure 26**). The TIC variation of this acquisition was roughly between 10-20%, again, above the preferred 10% threshold.

The **bottom** spectrum was also taken using a 5 μm ID emitter. For this emitter, the protonated $[M+H]^+$ molecule forms the base peak. The reoccurring peak at 279.1593 which has been present in all the other spectrums so far is also present here. The TIC variation of this acquisition was roughly between 8-13% and is thus an emitter on the border of being accepted as a routine emitter.

With a dataset size of $n = 3$, the average and standard deviation for the peaks corresponding to retinoic acid signal intensity is given in **Table 11**.

Table 11. For the peaks of retinoic acid, the size of the dataset, the average signal intensity, and standard deviation of the signal intensity is given.

n	Average signal intensity	Standard deviation of signal intensity
3	8.82E6	5.93E6

Although varying signal intensity, all emitters could detect retinoic acid and could have been used in DESI experiments.

4.4.3 Phosphatidylcholine

One 300 ng/mL solution of PC was injected using three different emitters. These were not all the same as for retinol and retinoic acid, because one of the 5 μm ID emitters broke. In all spectra, $[\text{M}+\text{H}]^+$ species were found. Three spectra were acquired, shown in **Figure 28**.

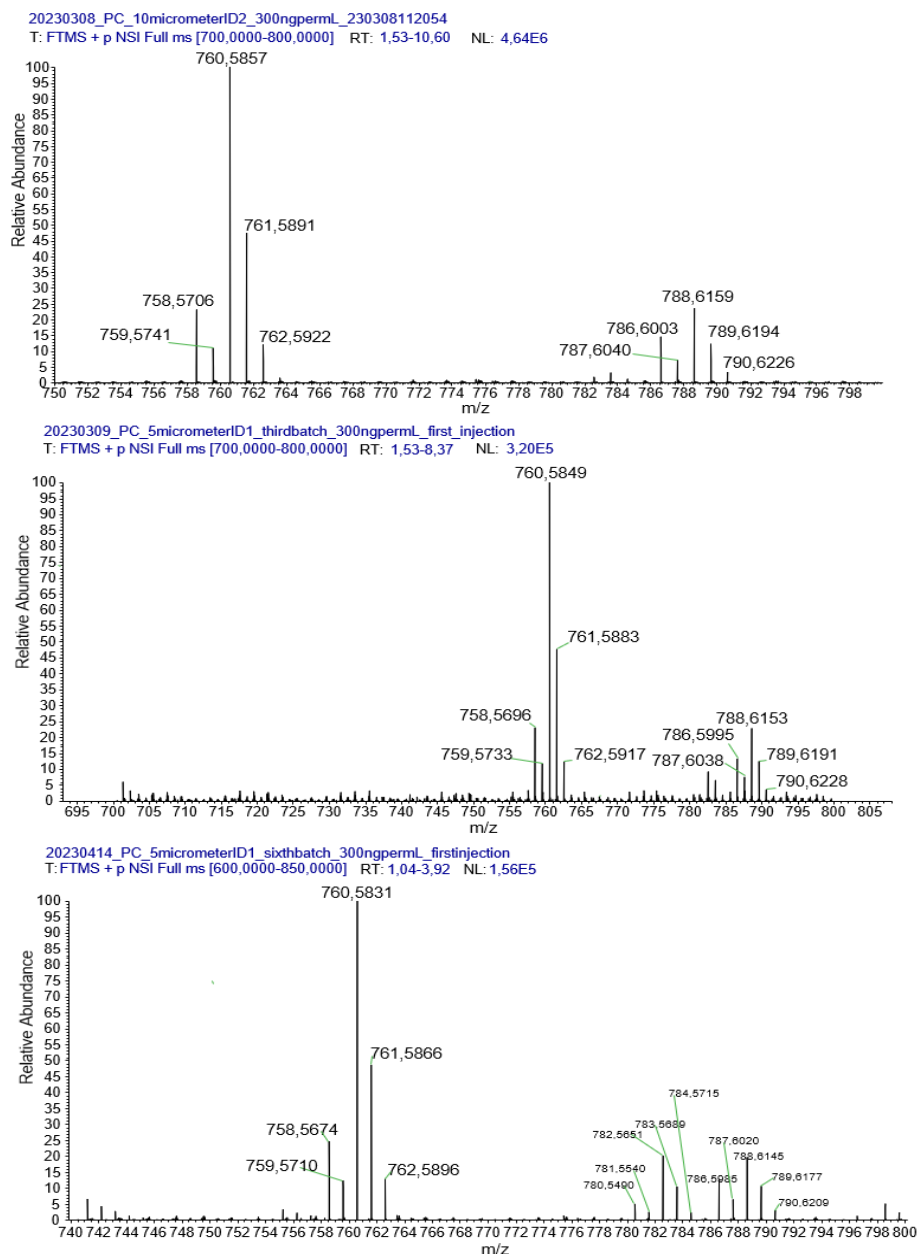


Figure 28. Three infusions were done, all using a 300 ng/mL PC solution. **Top:** Mass spectrum of the first PC infusion, using a 10 μm ID emitter. Two peak clusters were detected. The TIC variation varied between 5-8%. **Middle:** Mass spectrum of the second PC infusion using a 5 μm ID emitter. Two clusters of peaks were also detected here, with a third beginning to appear. The TIC variation varied between 15-40%. **Bottom:** Spectrum obtained after the third infusion of PC using a 5 μm ID emitter. This time, three clusters of peaks were clearly visible and was not previously seen to this extent. The TIC variation was 8-20%.

The **top** spectrum bore resemblance to the one displayed in **Figure 24**, which meant the emitter worked in a similar manner. In total, 10 peaks of interest were obtained, all a form of $[\text{M}+\text{H}]^+$

PC molecules with different length side chains. The base peak appeared at m/z 760.5857, corresponding to PC(34:1), with two following ^{13}C isotope peaks. Below this, a more unsaturated PC variant was found. Another cluster was detected around m/z 788.6159 with a very similar distribution of peaks. The most intense peak was thought to belong to PC(36:1), with two following ^{13}C isotope peaks. Below this cluster, a more unsaturated PC variant was found. The TIC variation was between 5-8%.

The **middle** spectrum agreed with what was achieved in the first spectrum. Again, this second emitter showed a much lower signal intensity, around 6.9% of the signal achieved in the first PC spectrum. This concurs with the findings for retinol and retinoic acid. The peaks around m/z 760.5849 and m/z 788.6153 corresponded to the protonated molecules of PC(34:1) and PC(36:1) respectively. These were both followed by two ^{13}C isotope peaks. The peak at m/z 758.5696 corresponded to PC(34:2) with a ^{13}C isotope peak at m/z 759.5733. PC(36:2) gave rise to the peak at m/z 786.5995, also having a ^{13}C isotope variant at m/z 787.6038. The TIC variation was between 15-40%. The AGC for this injection was below 40%. Based on both these parameters, this is a poor emitter and should not be used for nano DESI experiments, especially when the signal intensity was low.

In the **bottom** spectrum, the signal intensity dropped further, to only 3.3% of that obtained in the first spectrum. A gradual relative increase in the signal intensity of the cluster around m/z 782.5551 across the three emitters was seen. However, the reason for this cluster to remain somewhat more stable than the other two was not understood. The lowest mass cluster was, as before, centered around PC(34:1) at m/z 760.5831. The middle cluster was centered around a peak at m/z 782.5651, thought to be protonated PC(36:4). A more unsaturated protonated PC(36:5) was found at 780.5490, and a more saturated protonated PC(36:3) was found at m/z 784.5715. The highest mass cluster was centered around protonated PC(36:1) at m/z 788.6145. A more unsaturated variant, PC(36:2), was found at m/z 786.5985. All odd numbered m/z values were thought to be ^{13}C isotope variants of the peak to their left, except for m/z 762.5896 and 790.6209 which were thought to be doubly ^{13}C isotopes of PC(34:1) and PC(36:1) respectively. The TIC variation was 8-20%. The AGC was only between 50-70%, indicating a poor emitter here as well.

Table 12 lists an explanation of what ion gave rise to each peak in all the three acquired spectra using their nominal mass.

Table 12. The table explains the peaks shown in **figure 26**. For all the suggested molecules, it was the protonated molecule that was detected. Decimals are not given for these m/z -values because three different spectra were used in explaining the peaks.

m/z -value	Compound	m/z -value	Compound	m/z -value	Compound
758	PC(34:2)	780	PC(36:5)	786	PC(36:2)
759	¹³ C isotope variant of PC(34:2)	781	¹³ C isotope variant of PC(36:5)	787	¹³ C isotope variant of PC(36:2)
760	Base peak. PC(34:1)	782	PC(36:4)	788	PC(36:1)
761	¹³ C isotope variant of PC(34:1)	783	¹³ C isotope variant of PC(36:4)	789	¹³ C isotope variant of PC(36:1)
762	A double ¹³ C isotope variant of PC(34:1)	784	A double ¹³ C isotope variant of PC(36:4)	790	A double ¹³ C isotope variant of PC(36:1)

Table 13 gives the average signal intensity and standard deviation of PC(34:1) and PC(36:1), having a dataset with the size $n = 3$. These analytes were chosen due to their high abundance.

Table 13. The average signal intensity and intensity standard deviation is given for the peaks at m/z 760 and 788 for the three infusions.

	n	Average signal intensity	Signal intensity standard deviation
PC(34:1)	3	1.71E6	2.08E6
PC(36:1)	3	4.15E5	5.10E5

The emitters also showed varying signal intensity for PC but were nevertheless capable of qualitatively detecting the analyte. The emitters not displaying 100% AGC target should not be used for further experiments. Only the first emitter thus qualified for further use.

4.4.4 Phosphatidylglycerol

One 700 ng/mL solution of PG was injected for all three of the tested emitters. For these infusions, negative mode ionization was used and the $[M]^-$ ion was detected. One 10 μ m ID and two 5 μ m ID were used. **Figure 29** shows the three spectra acquired.

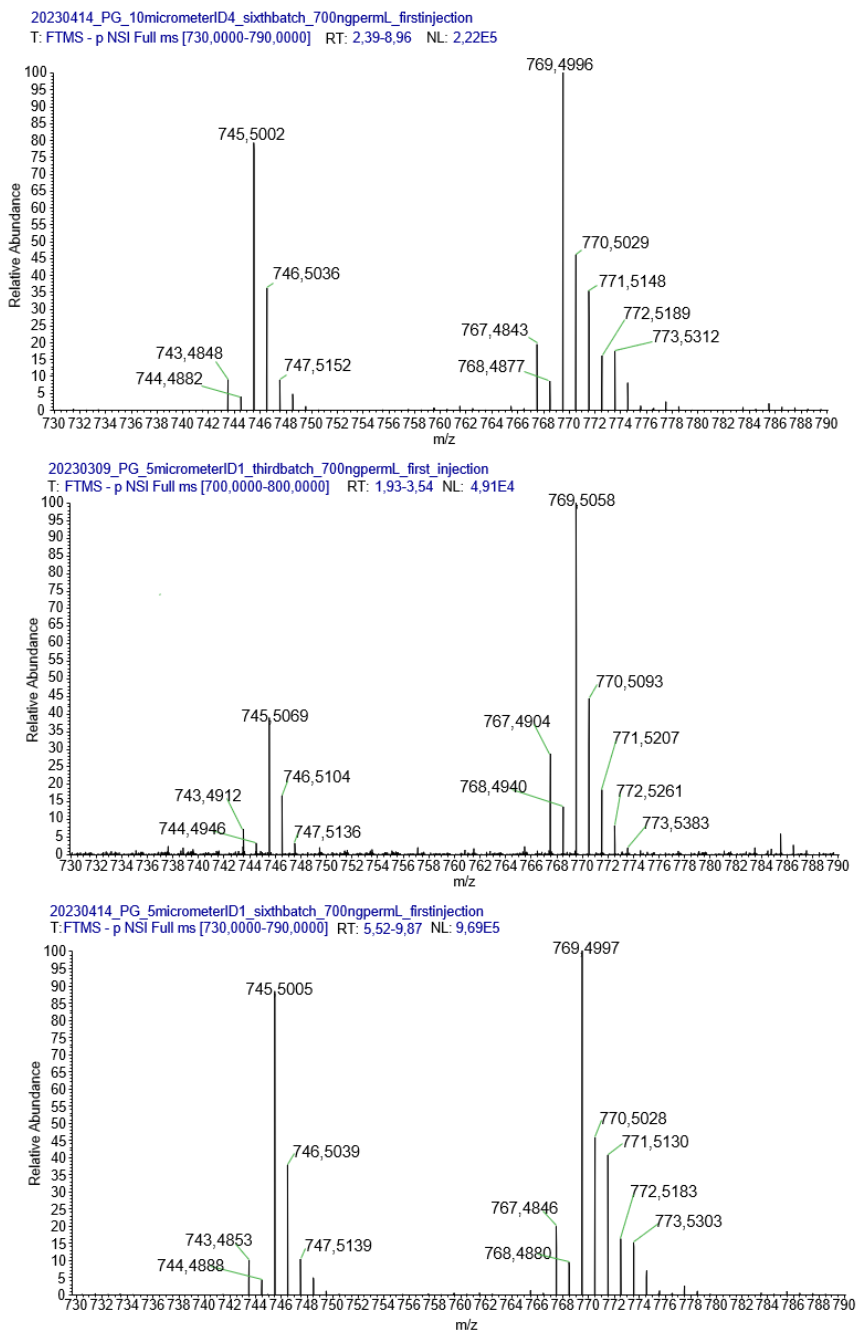


Figure 29. The three spectra acquired after injection of 700 ng/mL PG solution using three different emitters. **Top:** spectrum acquired using a 10 µm ID emitter. The TIC variation was between 20-100%, and the AGC target under 10%. **Middle:** the spectrum was acquired using a 5 µm ID emitter. The TIC variation was 30-70%. **Bottom:** this spectrum was also acquired using a different 5 µm ID emitter. The TIC variation was 10-40%, AGC target was between 10-20%.

In the **top** spectrum, the characteristic peaks of PG were found, as expected according **Table 3**. Two clusters of peaks were visible, resembling those found in infusion of PG standard using Thermo’s commercial HESI source. One cluster was centered around m/z 745.5002 (the PG(16:0/18:2) anion), with its ^{13}C isotope peak following at m/z 746.5036. The peak at m/z 747.5152 was the more saturated PG(16:0/18:1) anion. A more unsaturated PG anion, PG(16:0/18:3), was found at m/z 743.4848 with a ^{13}C isotope peak at 744.4882. For the higher

cluster, the base peak at m/z 769.4996 corresponded to PG(18:2/18:2) followed by a ^{13}C isotope peak at m/z 770.5029. PG(18:1/18:2) was found at m/z 771.5148, followed by a ^{13}C isotope peak at m/z 772.5189. PG(18:2/18:3) was found at m/z 767.4843, with its ^{13}C isotope peak at 768.4877. Lastly, the PG(18:0/18:2) and/or PG(18:1/18:1) anion was found at m/z 773.5312. The TIC variation was between 20-100%, a large variation compared to other emitters. The AGC target was also poor, with a value below 10%.

In the **middle** spectrum, the peak at m/z 745.5069 corresponded to PG(16:0/18:2). PG(16:0/18:1) was found for m/z 747.5136. The more unsaturated PG(16:0/18:3) appeared at 743.4912. For the higher cluster, m/z 769.5058 corresponded to PG(18:2/18:2), while m/z 771.5207 and m/z 773.5383 were PG(18:1/18:2) (with some contribution from PG(18:0/18:3)), and PG(18:0/18:2), respectively. However, as have been seen with all the other infusions, this emitter repeatedly gave very low signal intensity. Therefore, the peak at, e.g., m/z 773.5383 was almost not visible. The TIC variation was between 30-70%.

The **bottom** spectrum shows the same two similarly distributed clusters of peaks, one centered around m/z 745.5005 and one around m/z 769.4997. 745.5005 corresponded to a PG(16:0/18:2) anion, with its ^{13}C isotope peak following at m/z 746.5039. The ion giving rise to m/z 747.5139 was the saturated PG(16:0/18:1) anion. A more unsaturated PG variant, PG(16:0/18:3) was found at m/z 743.4853, with an isotope peak at 744.4888. For the higher cluster, the base peak at m/z 769.4997 corresponded to PG(18:2/18:2), followed by one ^{13}C isotope peak, and PG(18:1/18:2) at m/z 771.5130, with a ^{13}C isotope peak coming in at m/z 772.5183. 773.5303 could be both the PG(18:0/18:2) and PG(18:1/18:1) anion. PG(18:2/18:3) corresponded to the peak found at m/z 767.4846, followed by its ^{13}C isotope peak at m/z 768.4880. Compared to the top spectrum, a very even distribution between PG(16:0/18:2) and PG(18:2/18:2) were seen, as opposed to in the second infusion. In all, the similarities between emitter 1 and 3 are quite substantial with respect to base peak intensity and relative intensities and are thus comparable. The TIC variation varied between 10-40%. The AGC target was as low as 10-20%.

The even-numbered peaks in the three spectra were PG variants, and the following odd-numbered peaks were thought to be ^{13}C -isotope variants. This is confirmed by both their mass accuracy as well as their relative peak intensity, which was about 40-45%. **Table 14** summarizes the peaks of interest from the three spectra of PG acquired giving their nominal masses, and explaining what ion gives rise to them.

Table 14. The table lists the m/z -values of the peaks of interest and explains what ionized molecule gives rise to each of them. Decimals are not given for these m/z -values because three different spectra were used in explaining the peaks.

m/z -value	Compound	m/z -value	Compound
743	PG(16:0/18:3)	768	^{13}C isotope variant of PG(18:2/18:3)
744	^{13}C isotope variant of PG(34:3)	769	Base peak: PG(18:2/18:2)
745	PG(16:0/18:2)	770	^{13}C isotope variant of PG(18:2/18:2)
746	^{13}C isotope variant of PG(16:0/18:2)	771	PG(18:1/18:2) and PG(18:0/18:3).
747	PG(16:0/18:1)	772	A ^{13}C variant of PG(18:1/18:2)
767	PG(18:2/18:3)	773	PG(18:0/18:2) and PG(18:1/18:1)

As pointed out in section 4.3.4, the manufacturer of this phosphatidylglycerol solution had already given the relative abundance of the different types of side chains. Therefore, the m/z values found was confidently used to assign the exact chain length based on the mass of the main body, and the individual masses of the chains. However, for the peak at m/z 771 in each spectrum, some of the peak intensity is undeniably from the PG(18:0/18:3) variant, as this molecule has the exact same mass, but with a lower specified abundance. The same goes for the peak occurring at m/z 773, which is mostly PG(18:0/18:2) due to the high relative abundance of 18:2 fatty acids but is also some PG(18:1/18:1).

Table 15 gives the average signal intensity for peaks at m/z 745 and 769, as well as their standard deviation using $n = 3$. These analytes were chosen due to their high abundance.

Table 15. The average signal intensities and standard deviation of signal intensities across three spectra, using PG(16:0/18:2) and PG(18:2/18:2) as model analytes.

	n	Average signal intensity	Standard deviation of signal intensities
PG(16:0/18:2)	3	3.24E5	3.25E5
PG(18:2/18:2)	3	4.13E5	3.99E5

Although the emitters could detect PG species, their TIC variation and AGC target values were poor. As PG was the last analyte, wear may be the cause of the unwanted AGC target. Such emitters should not be used neither in further testing nor in real nano DESI experiments.

4.4.5 Summary of all direct infusions using in-house made emitters

The spectra of twelve infusions of retinol, retinoic acid, phosphatidylcholine, and phosphatidylglycerol have so far been presented showing their most important peaks, along with the average and standard deviation of the signal intensities across emitters. In **Table 16**, the relative standard deviation of each analyte's signal intensity is given.

Table 16. Relative standard deviation of signal intensities within each set of direct infusions

	Retinol	Retinoic acid	PC(34:1)	PC(36:1)	PG(16:0/18:2)	PG(18:2/18:2)
RSD (%)	106	67	121	123	100	97

There are large variations in these emitters, and a different result can be obtained due to different emitters. However, it is worth noting that these differences seem repeatable. If internal standards or calibration curves are used in a series of analyses without changing emitters, a quantitatively reliable result should still be obtained. Compared to infusion using HESI source, general conclusions are hard to make as each emitter behaved differently. The second infusion of each analyte generally have a more polluted spectrum with lower intensity, while the third emitter has a higher intensity than HESI for retinol, but not for the other analytes. This means each individual emitter used will not represent the others, and reproducibility is poor. In this particular case, there was likely a fault in the 5 μm emitter used to obtain the second spectra, and this particular one and others portraying similar behavior ought not to be used as a PCE or NCE in imaging experiments

Emitters tested with all four emitters showed very variable results, and a stronger case for a stability studies has been established, with both signal intensity and TIC variation in mind.

4.5 Assembly of the nano desorption electrospray ionization instrument platform

The ionization platform was assembled when all the necessary parts were acquired. These are the parts listed in **Table 1**. The aspects considered when assembling was the size of the base, its attachment compatibility with the MS, its weight, distances between the components to be placed on the base, and the propagating vibrations from the MS. When these factors were satisfactory, the nano DESI was ready to be used for infusions and cell sample analyses.

4.5.1 The base platform was integrated with a nanospray source

The base consisted of an open-ended 10x20x30 cm aluminum cuboid shape. A Nanospray flex open ion source interface (Thermo Fisher) was taken apart and attached to the base. Only the frame and the rails underneath were kept. This makes the nano DESI attachable to a QExactive MS instrument. **Figure 30** shows the base and the attached interface.



Figure 30. The pictures show the open-ended aluminum cuboid shape used as a base for the ion source. A Nanospray flex interface was taken apart and mounted onto the base for easy mantling and dismantling of the ion source onto the mass spectrometer.

4.5.2 The sample holder motorized stages were implemented on the right-hand side

On the right side of this base, three electrical motor adjustable stages were attached, one to move in each spatial direction. Between the Y stage and X stage, a metal piece was included to angle the X stage in a horizontal fashion. The sample holder was set on an extender on the X-stage. All three stages were interconnected via 4-pin male to female M8 cables. Connection from the stage setup to a computer via a USB cable will enable the operator to use a LabView program to run the stage motors to move the sample holder in a predetermined pattern, according to theory given in **section 1.5.1**. **Figure 31** shows the three attached stages, as well as the extender on the X-stage holding the sample holder.

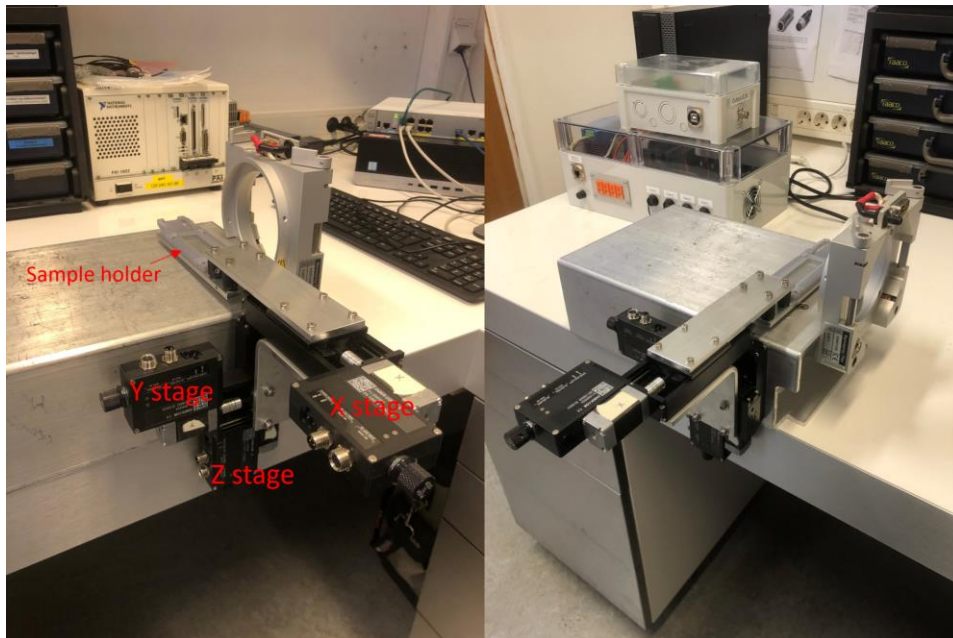


Figure 31. The stages controlling the position of the sample holder were mounted on the side. A small metal piece was included to orient the X stage in the right direction. The sample holder was 3D-printed to fit a glass slide onto which the sample can be put.

4.5.3 Micro positioners held the articulating arms for fine tune adjustments of emitters

In front of the sample holder, two manually adjustable micro positioners were mounted, each with an articulating arm attached through a 3D-printed piece. Each arm consisted of two two-jointed pieces, connected via a 3D-printed connector. A 3D-printed crocodile clamp was

fastened on the end of both arms to hold both the primary capillary emitter and the nanospray capillary emitter. **Figure 32** shows how these capillary-holding stages were mounted.

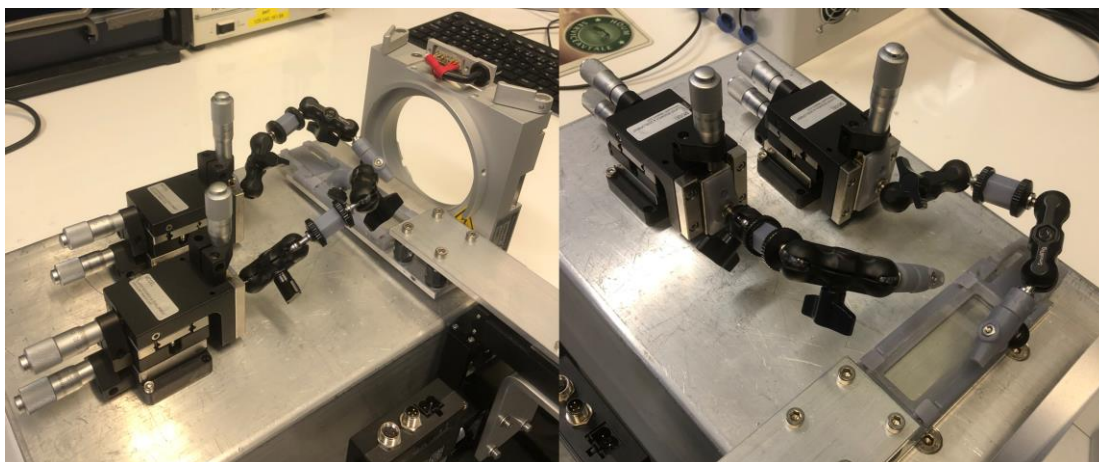


Figure 32. Two adjustable micro positioners were mounted on the base. To each micro-positioner, two two-jointed arms with a 3D-printed connector piece and a crocodile clamp attached at the end for holding each capillary emitter were installed

4.5.4 A modified nano spray voltage source was incorporated on the arm holding the primary capillary emitter

A modified voltage source originally belonging to the Nanospray flex open ion source was connected to the crocodile clamp holding the PCE in one end, and to the voltage outlet of the ion source in the other end. This is in accordance with the illustration depicted in **Figure 9**.

Figure 33 shows how the cable was attached.

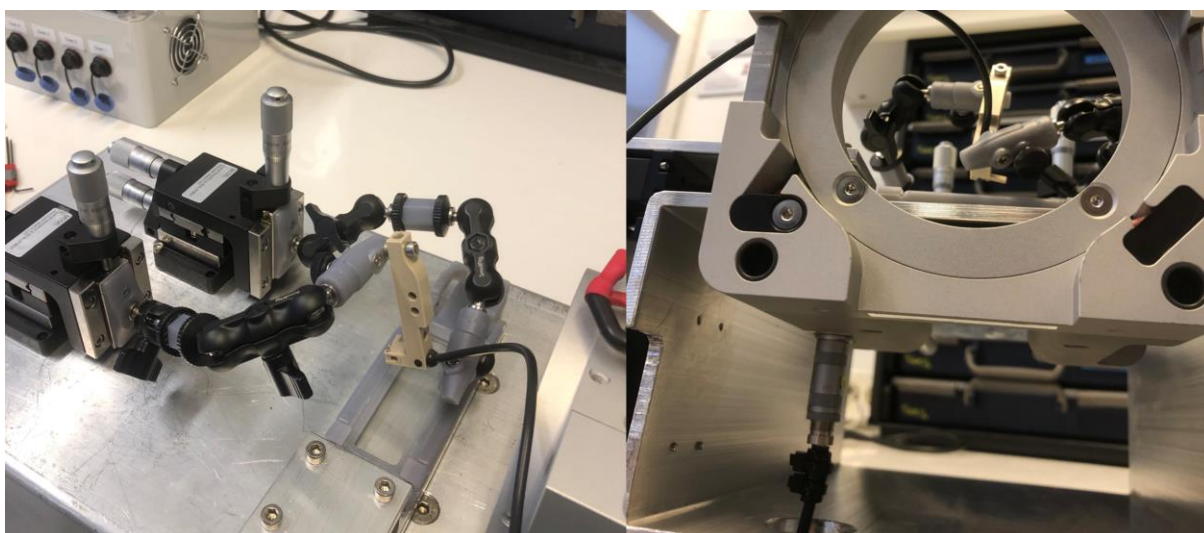


Figure 33. The pictures show how the voltage supply was incorporated. Using a screw, it was attached to the crocodile clamp holding the primary capillary emitter in one end, and to the voltage outlet of the ion source in the other end.

4.5.5 Two Dino-Lite cameras were incorporated to monitor the liquid bridge from two angles

To best monitor the fine tuning of emitters when trying to obtain a liquid bridge, two Dino-Lite cameras were set up, one on either side of the micro positioners. One camera was set up to monitor the two emitters from above, while the other monitors the emitters from the side. In this way, the fine tuning of the emitters' position and angle can easily be adjusted to make contact at their tips. **Figure 34** shows their mounting and angling towards the emitters.

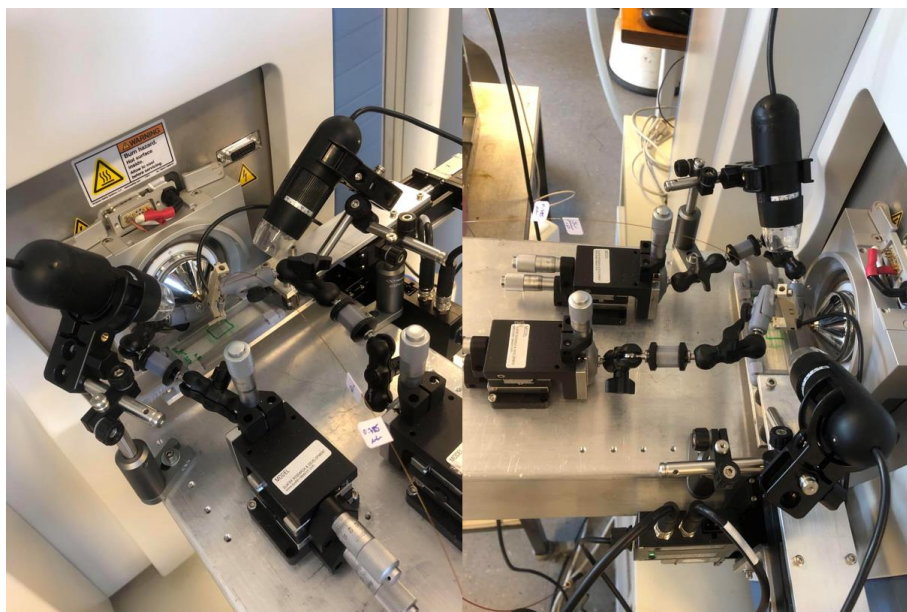


Figure 34. Two Dino-Lite cameras were set up, one on either side of the micro positioners. The left camera points down from above, while the other points more from the side. This way, fine adjusting the emitters becomes an easier task.

4.5.6 Correct and optimal installation of emitters was time consuming and requires practice

When trying to attach the capillaries, it was quickly discovered that the NCE should be set up first, as this is the one closest to the MS inlet. Setting up the PCE first would leave very little room in the already restricted space to set up the NCE. After attaching the NCE in the crocodile clip it was roughly aligned with the MS inlet using the articulating arm alone.

The best way found to mount the PCE was first attaching it to the capillary leading the solvent from the nano LC pump via a Valco union. It was then put in the crocodile tip, before being put under the magnetic lid of the voltage supply. Using the articulating arm, its position was roughly

adjusted so its tip was as close to the NCE as possible. After setting up both emitters, their position was fine adjusted using the micro positioners.

Figure 35 shows the setup with the emitters installed. The Dino-Lite cameras were used to observe the emitters' positions and are of absolute necessity when fine tuning over as small distances as just a few micrometers.

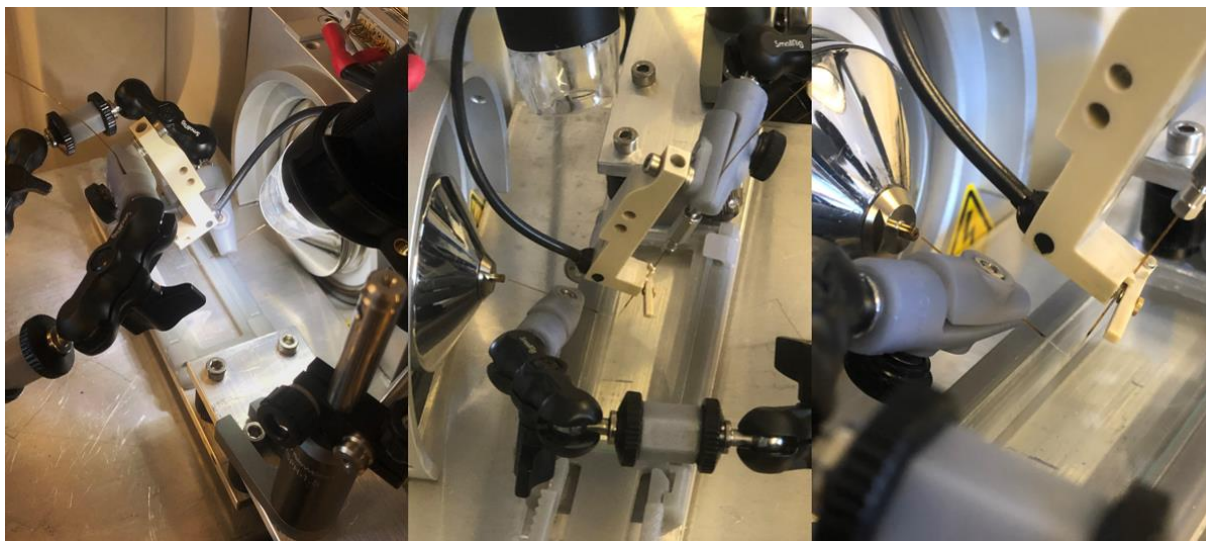


Figure 35. The figure shows how the emitters were best found mounted. The NCE was mounted first due to practical reasons. The PCE was first connected to the solvent delivery capillary, before being put in the crocodile tip. It was then put under the lid of the voltage supply. Their positions were roughly adjusted using the articulating arms, and fine tuned in the end using the micro positioners. A Dino-Lite camera was also incorporated to monitor the relative position and distance between the two emitters.

After having set up the emitters, the nano DESI platform is fully assembled, and ready to use.

4.5.7 Shortcomings and suggestions for improvements of the current design

This design covers the main uses of the platform and should suffice for imaging purposes. However, there are some drawbacks to this specific design when analyzing in hindsight. Most notably is the difficult process of correct rough positioning of the NCE, and the large spatial fingerprint the micro positioners, articulating arms, and emitters leave. The NCE is hard to adjust correctly both with respect to distances and angles. This will take some practice by the operator. A design where the position and angles could more easily be changed without having

to dismantle the emitter from the crocodile tip would be an improvement. This could be achieved by having an articulating arm that one can easily attach and detach from the micro positioner, i.e., by using a clip mechanism instead of screwing the arm into the positioners. If only a small adjustment must be made to the emitter's position, most of the form of the arm wants to be kept. However, if the arm needs to be unscrewed, this is hard to do.

As the emitter does not have to be moved after first having been set up correctly, a holder that lets the operator set up the emitter the same way each time is beneficial. To avoid the arm altogether, some form of emitter holder may be 3D printed and slid onto a permanently installed track on the platform. If the holder has a slit with grooves at a fixed optimal angle with a screw for tightening, the emitter can be preinstalled in the holder before its slid in place. This makes much of the adjustment process easier as the combination of finding the perfect angle and distances is reduced to only a distance adjustment. **Figure 36** gives a principal sketch of what this emitter holder could look like.

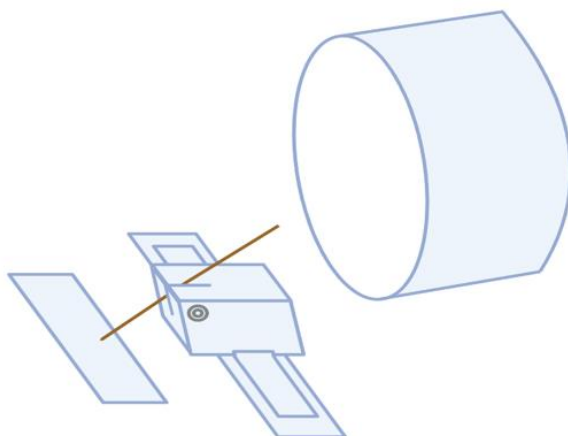


Figure 36. The nanospray capillary emitter may be put in a 3D-printed permanent holder, having a slit with grooves that are at the optimal angle for easy setup. A screw on the side is used to tighten the emitter. Made using BioRender.com.

Depending on the platform design there may not be enough room between the sample holder and the MS inlet, but a similar idea might be used.

Another issue is the spatial footprint, which is large. Making small adjustments to the system thus becomes difficult, as one must be very careful not to bump into anything. This could be solved by having a wider platform so the micro positioners can be attached on either side of the inlet instead of directly in front of it. Such an approach would also decrease the force felt by the point of attachment to a shorter distance away from it. An illustration of such a platform is given in **Figure 37**.

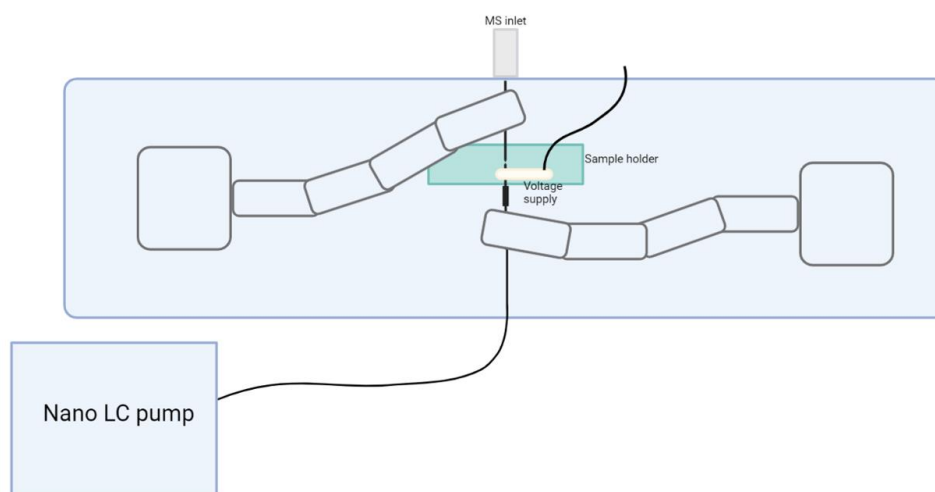


Figure 37. Alternative platform design, with a presumed lower spatial fingerprint.

Installation of a static NCE holder such as the one suggested will also reduce the spatial fingerprint.

However, in this configuration, the stages controlling the sample holder will have to be incorporated from underneath or from the front, as there is little room for them on the side. This will also be instrument dependent, as some instruments have a panel that bulges outwards. Several practical considerations must thus be taken.

With the implementation of the shear force probe, more room is needed. As the progression of this project didn't go as far as to introduce this mechanism for fine steering sample holder height, SFM was not introduced. Therefore, this is not considered in this alternative design.

In all, the platform was successfully built to the point where proof of function could be tested. Some weaknesses have although been found, and corrective measures proposed.

4.6 Direct infusions of standard analytes via liquid bridge

To assess the formation of a liquid bridge, a pure background and a solution background was acquired. The pure background is the result of no desorption solvent being introduced to the MS, while the solution background is the signal from the matrix of the sample without the analyte being injected. For this, a liquid bridge must be in place. Signs to look for is firstly the

signal intensity, which is increased about a hundred-fold. Secondly, more ions are detected with a high signal intensity in the lower mass end of the spectrum. These are both signs that the liquid bridge is acquired. **Figure 38** shows the pure background versus the solution background.

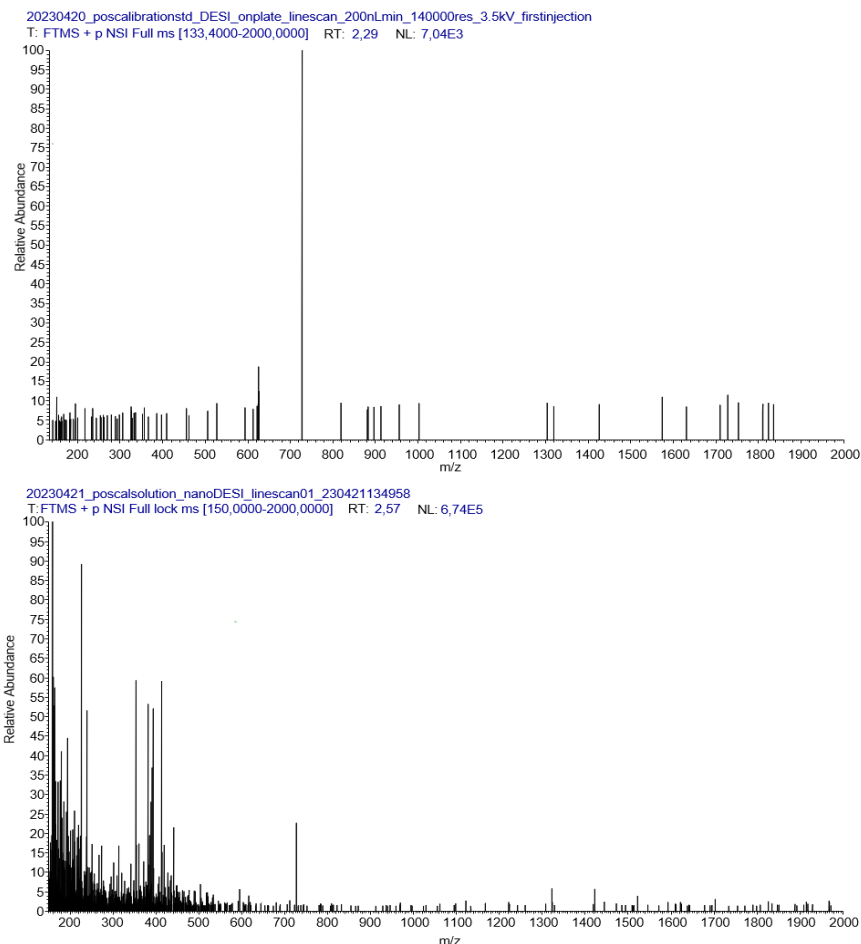


Figure 38. Two spectra showing the differences for when the liquid bridge is absent versus achieved. **Top:** low intensity background signal of no solution. A liquid bridge is not assumed formed. **Bottom:** high intensity background signal. Solution is assumed transferred from the primary to the nanospray capillary emitter, via the formed liquid bridge, but containing no analyte.

4.6.1 Liquid bridge infusion of retinol

The four analytes were directly injected through the liquid bridge, according to description in **section 3.12**.

First, a 300 ng/mL solution of retinol was analyzed. **Figure 39** gives the TIC and mass spectrum obtained.

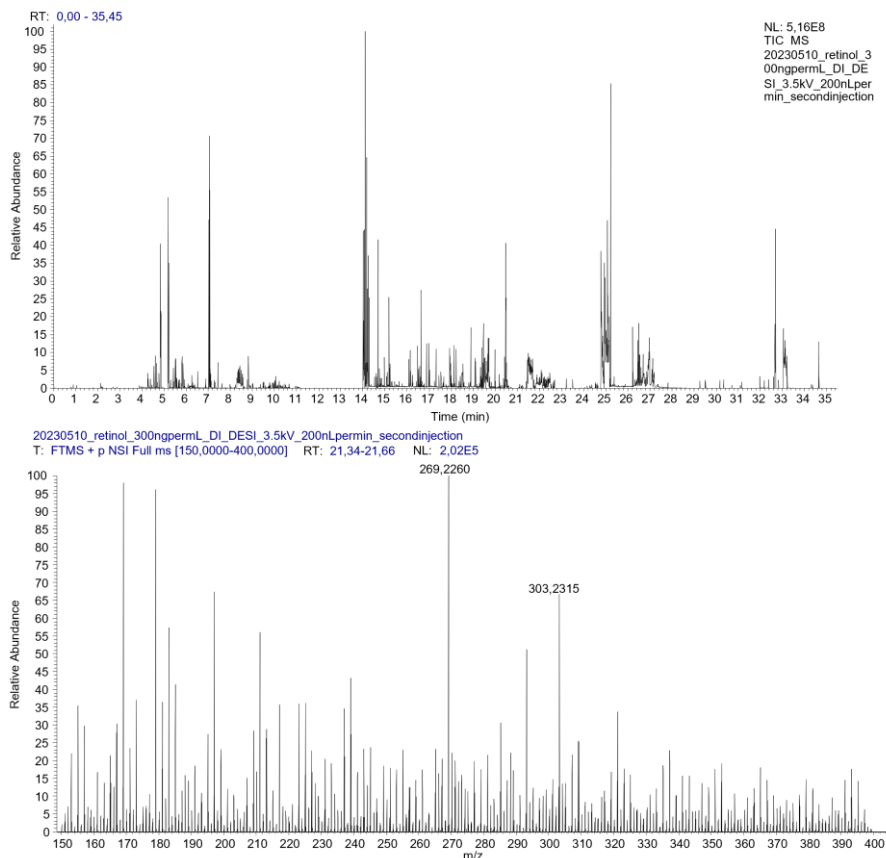


Figure 39. **Top:** the TIC obtained when injecting a 300 ng/mL retinol solution. **Bottom:** the mass spectrum acquired between 21.34 and 21.66 minutes into the injection.

The TIC in this injection is shown to be very unstable. This can be seen by the sudden spikes or peaks. Preferably, the TIC should be a straight horizontal line as this would indicate an even flow of solvent with a constant supply of analytes. For this spectrum, the TIC variation value was not noted, but is expected to be above 100%. This impacted the signal of retinol which consequently came in bursts and could be completely gone from one scan to the next, indicating an uneven flow of solvent and therefore the analyte from the PCE to the NCE. However, there were also longer time intervals where a background solution signal was achieved, but where there was no analyte signal. An uneven flow will not clearly explain this, as it was expected that the analyte would show up whenever a flow was assumed.

As for the mass spectrum, retinol was found mainly as the $[M-H_2O+H]^+$ adduct at m/z 269.2260, with a mass accuracy of -1.40 ppm. Another compound was found in its protonated $[M+H]^+$ state at m/z 303.2315 with a molecular formula $C_{20}H_{30}O_2$, thought to be a hydroxyretinol, which is also a retinoid. The detection had a mass accuracy of -1.18 ppm. **Figure 40** gives the structure of a hydroxyretinol, specifically the 3-hydroxyretinol. Note that the position of the OH-group can vary, and the exact annotation is therefore difficult.

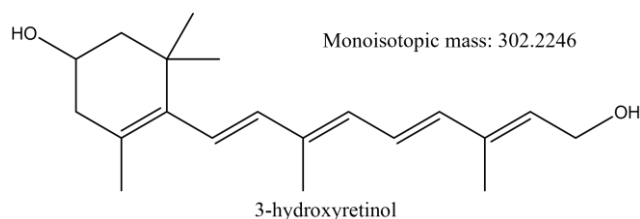


Figure 40. The structure of a 3-hydroxyretinol, a retinoid found in its protonated state at m/z 303.2315.

The analyte was detected during infusion through the liquid bridge indicating successful ionization and nebulization, although the TIC had a very high variation and the detection stability was low.

4.6.2 Liquid bridge injection of retinoic acid

The 600 ng/mL retinoic acid solution used in previous infusions was also used here. **Figure 41** gives the TIC and the spectrum obtained.

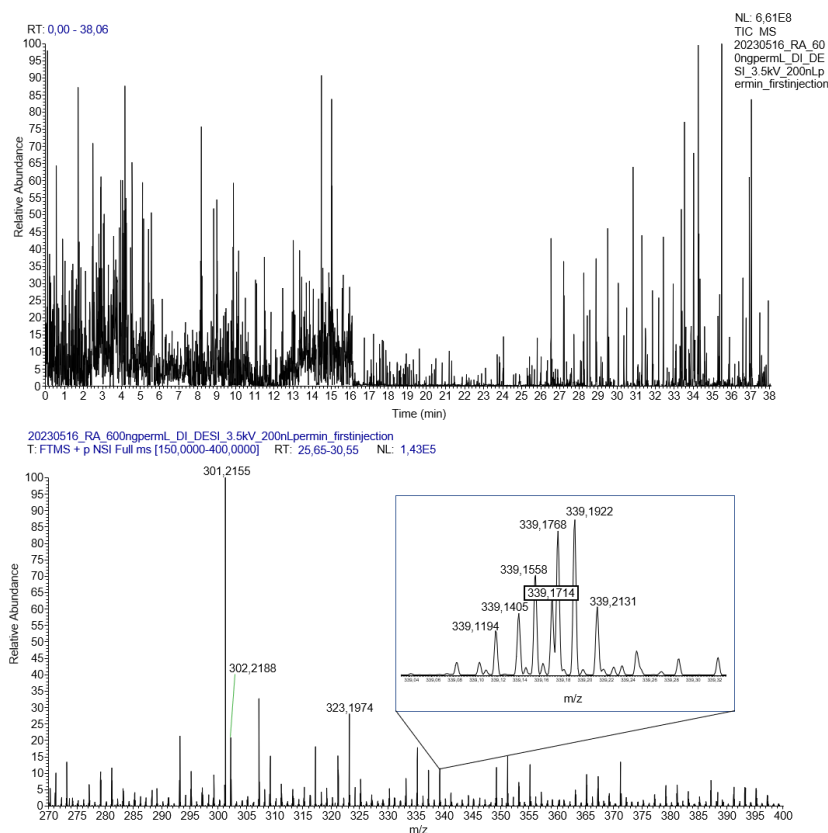


Figure 41. **Top:** TIC of a 600 ng/mL retinoic acid solution. A large variation of intensity is observed. **Bottom:** mass spectrum obtained, chosen in the time interval 25.76-30.59 minutes. Many ions were detected, among them the $[M+H]^+$ at m/z 301, $[M+Na]^+$ at m/z 323, and $[M+K]^+$ at m/z 339.

This TIC also showed a large variation in ion intensity, as the TIC of retinol. The periodical bursts of ions, some with the analytes and others without, was also characteristic of this infusion. The source of the sudden increase in TIC signal was not due to the analyte, and thus difficult to characterize.

The mass spectrum shown was the average of spectra found within an almost 5-minute time interval of the TIC. However, in most intervals the analyte was not to be found but would periodically appear. This was also characteristic of the injection of retinol, and the reason for this phenomenon is probably the same but remains unclear.

The analyte ions found were the protonated $[M+H]^+$ retinoic acid specie at m/z 301.2155, with a mass accuracy of -2.35 ppm. Another ion, the $[M+Na]^+$ adduct of retinoic acid, was also found at m/z 323.1974 with a mass accuracy of -2.32. A cluster of ions at nominal mass 339 is highlighted because of the presence of a peak resembling a $[M+K]^+$ adduct. The ion at m/z 339.1714 has a mass accuracy of -2.03 from this adduct.

The correct ion was detected, indicating successful ionization and nebulization. Different adducts previously not seen were found in addition to the predicted protonated retinoic acid.

4.6.3 Liquid bridge injection of phosphatidylcholine

A 300 ng/mL solution of phosphatidylcholine was directly infused into the MS. The following TIC and mass spectrum were obtained.

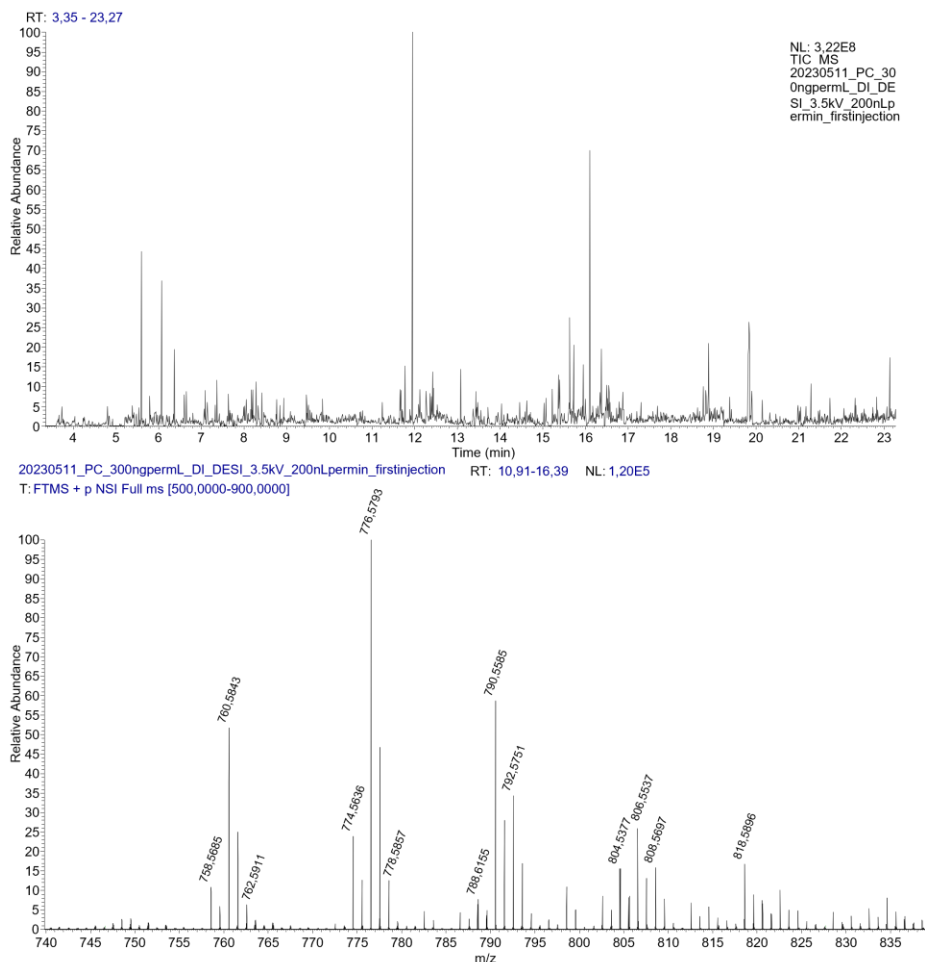


Figure 42. **Top:** the most relevant time interval of the TIC obtained after injection of a 300 ng/mL phosphatidylcholine solution was selected. **Bottom:** the mass spectrum obtained from the most relevant time interval, where PC-like peaks were observed. The peaks of highest interest were selected, and their m/z given. Isotope peaks are not labeled but exists at every odd-numbered m/z value following the even-numbered ones.

The characteristic TIC bursts return for this analyte, suggesting a non-even flow into the MS. About five different clusters were detected, all having a somewhat similar distribution to the ones previously found, indicating their PC-relatedness.

In this spectrum, the top 10 highest intensity peaks were selected for review. Three other peaks, namely 758, 762, and 788 were also selected due to their presence in previously obtained spectra. **Table 17** explains the peaks found, with their mass accuracy in ppm. The mass accuracy was included because some values were high and may indicate a wrong annotation.

Table 17. The table provides the nominal masses of the compounds found when directly injecting the PC solution. A possible explanation is also given, as well as the mass accuracy (ppm). Many of the compounds have very high mass accuracy for an orbitrap analysis.

<i>m/z</i> -value	Compound	Mass accuracy (ppm)	<i>m/z</i> -value	Compound	Mass accuracy (ppm)
758.5685	PC(34:2)	-1.23	790.5585	PC(37:7)	52.08
760.5843	PC(34:1)	-1.03	792.5751	PC(37:6)	26.90
762.5911	PC(34:0)	-12.63	804.5377	PC(38:7)	-19.99
774.5636	PC(35:1)	-47.94	806.5537	PC(38:6)	-19.50
776.5793	PC(35:0)	-47.75	808.5697	PC(38:5)	-19.02
778.5857	PC(36:6)	61.10	818.5896	PC(39:7)	24.64
788.6155	PC(36:1)	-1.12	-	-	-

The most striking difference to previous injections was the number of relevant peaks found. One spectrum that might have been comparable was the bottom spectrum in **Figure 28**, which had a similar base peak signal intensity but without the peaks at *m/z* 774, 776, 778, and 792. These were previously not seen at all in any spectra but were prominent here. Also, one of these happened to be the new base peak, namely 776. The relative intensity between the peaks was also very different. Firstly, the 760 peak was no longer the base peak. Secondly, 788 used to be at about 20% relative intensity of 760 but now falls to about 7%. Thirdly, the 790 peak increases from about 3% in **Figure 28** to about 55% of base peak intensity and is even of more abundance than the 760 peak. In all, large shifts in unique species and their intensities were detected.

Another observation made is the consistently low ppm values of the previously most abundant PC types, namely PC(34:2), PC(34:1), and PC(36:1). This speaks of a correct mass-to-charge detection for these compounds. The species showing higher abundance in this injection has an unexpectedly high ppm-value and the annotation is therefore unsure. For an orbitrap, a mass accuracy below 5 ppm would be expected. The sudden finding of these other substances, as well as their high ppm-value, makes their origin hard to assess. One reason for a high mass accuracy is a poorly calibrated mass spectrometer. However, with the consistent low ppm-value of some of the species also found in previous analyses, poor calibration is unlikely.

Clusters resembling those previously found when analyzing PC were also found here, but in a higher number. The peaks in them can be correlated to PC, but with a high ppm-value indicating they're not really species of PC. Three species, PC(34:2), PC(34:1), and PC(36:1), were found with acceptable ppm-values.

4.6.4 Liquid bridge injection of phosphatidylglycerol

A 700 ng/mL PG solution was injected. The TIC obtained and the mass spectrum within a chosen time interval are given in **Figure 43**.

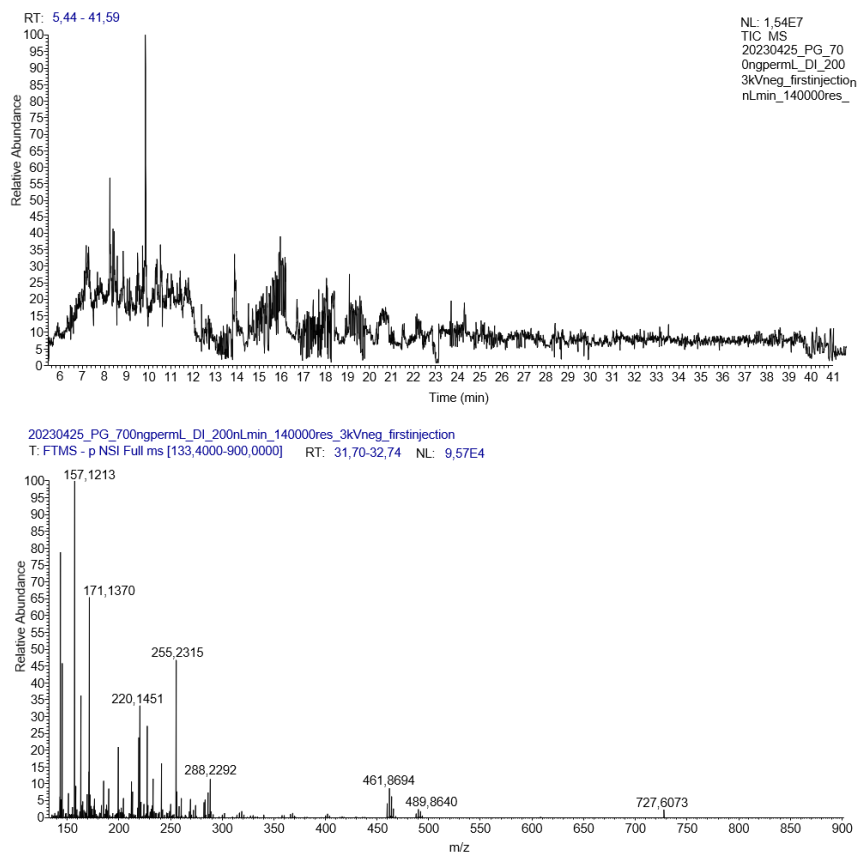


Figure 43. Top: the TIC of a chosen time interval after injecting the 700 ng/mL PG solution. Bottom: mass spectrum of an arbitrarily chosen time interval. No meaningful analyte signals were found.

The TIC obtained was much more reliable in this injection and stabilizes after about 25 minutes. Therefore, no bursts of desorption solvent were thought to occur here.

However, as can be seen in the mass spectrum, no meaningful analyte signals were found. Although the overall signal intensity was low, and even lower than the solution background signal portrayed in **Figure 38**, this was an indication that a liquid bridge was in fact formed as the spectrum did detect some background ions. Why the PG species was not detected is unknown, but repeated infusions showed much the same result.

4.6.5 General remarks after direct injection through liquid bridge

The detection of the infused molecules in positive mode has several important implications. Firstly, it indicates that a liquid bridge was indeed formed, and that emitters made in-house using the gravity-assisted self-termination technique and subsequent coating of SnO₂ using ALD can be transfer analytes through them. Secondly, it suggests that the voltage supply works, and that the system is capable of ionization of compounds and nebulization through electrospray for detection.

Unstable TICs were obtained for the three positive injections. Because an even flow was assumed out of the PCE, the problem most likely lies somewhere after it in the flow order. However, whether the cause is due to a low-quality liquid-bridge or a faulty NCE is unknown and hard to tell. Before using the platform for research purposes, this instability ought to be resolved. Trying emitters with slightly larger ID or other flow rates, as well as removing vibrations induced to the platform from the operating instrument by, e.g., vibrational insulation, is worth looking into. In addition, Ingela Lanekoff's group at Uppsala university, Sweden, has developed a pneumatically assisted nano DESI for enhanced detection. In pneumatically assisted nano DESI, the NCE is put in a device that flushes nitrogen gas coaxially out together with the analytes subjected to electrospray before the MS inlet. This gives improved suction forces into the NCE due to a lower pressure on the back end, allowing a longer distance between the NCE and the MS inlet because of lower dependence on the MS vacuum. Therefore, the analytes have more time to nebulize, resulting in increased S/N by more than a thousand-fold. It also broadens the range and composition alternatives for what solvents to use and may also resolve the high instability of the TIC [104].

Another observation made was the ease of achieving a liquid bridge in positive mode compared to negative mode. Enlightenment may lie in the similarities between the nano DESI system and the water thread experiment. Because the two are similar, some of the theory may be transferable. According to one article on theory surrounding the experiment first conducted by the English engineer Lord Armstrong [105], two closely positioned containers of chemically pure water will have a bridge of water suspended in free air between them when there is a current applied to both containers. The two emitters can be treated as two containers and the liquid bridge as the suspended water thread between them. In the article by Marín *et.al.* it is stated that there is a flow of liquid in both directions between the containers. However, no

pattern could be observed. In another article [106], there was usually observed a transfer of water from the anode side to the cathode side. This lines up with the results achieved in this thesis. In positive mode, when the emitter is the anode and the MS is the cathode, a function liquid bridge is easily achieved. However, when switching polarities, the system is flipped. The difficulties in achieving the liquid bridge at this point may arise from opposing forces which stops the liquid from going into the MS in negative mode.

Elaborating on the process of trying to obtain a liquid bridge in negative mode ionization might support this explanation. In positive mode, once the emitters were in place, the flow of liquid became visible through the NCE at the exact moment the voltage was turned on. Therefore, there seemed to be two forces contributing to liquid flow: the vacuum inside the MS, but also some hydroelectrical effects. However, it frequently occurred that when reversing the polarity, the liquid bridge was lost instantaneously, without changing any other parameter. One hypothesis is therefore that when switching polarities, one of the previously cooperating forces starts acting the opposite way, and the hydroelectrical effect hinders the liquid from flowing to the MS. This would align with the theory of a flow from the anode to the cathode in the water thread experiment. To the authors understanding, this is the best explanation found. With that said, as there does not seem to be a unanimous opinion on the direction of flow among researchers, much uncertainty remains. The liquid used was also not chemically pure as there were charged analytes in the matrix but may have been pure enough to maintain a liquid bridge, or a water thread in this context, of micrometer scale.

It should be noted that although difficulties were experienced, the bridge was still achieved to at least some extent as can be seen from **Figure 43**.

4.7 Desorption of retinol, retinoic acid, and phosphatidylcholine from glass slide

Because the liquid bridge was assumed formed, the next natural step was to verify if molecules could be desorbed from a surface underneath. Therefore, the analyte standards previously used were deposited on a glass slide, and the sample holder was lifted until contact with the liquid bridge was visible through the Dino-lite cameras. Spectra were acquired to see if any of the

deposited analytes were desorbed and detected. If yes, the desorption of analytes from cellular samples should also be possible.

When first trying to apply the analytes in the concentrations previously used for direct infusions, no signal was found for any of them, only the solution background signal. This was also the case when analyte solution was deposited on slides and let to dry. Therefore, a higher concentration of 0.025 mg/mL was used for all analytes and applied to a glass slide as described in **section 3.13**.

4.7.1 Retinol

Figure 44 gives the TIC and spectra obtained after analyte desorption of a 0.025 mg/mL retinol solution applied to a glass slide.

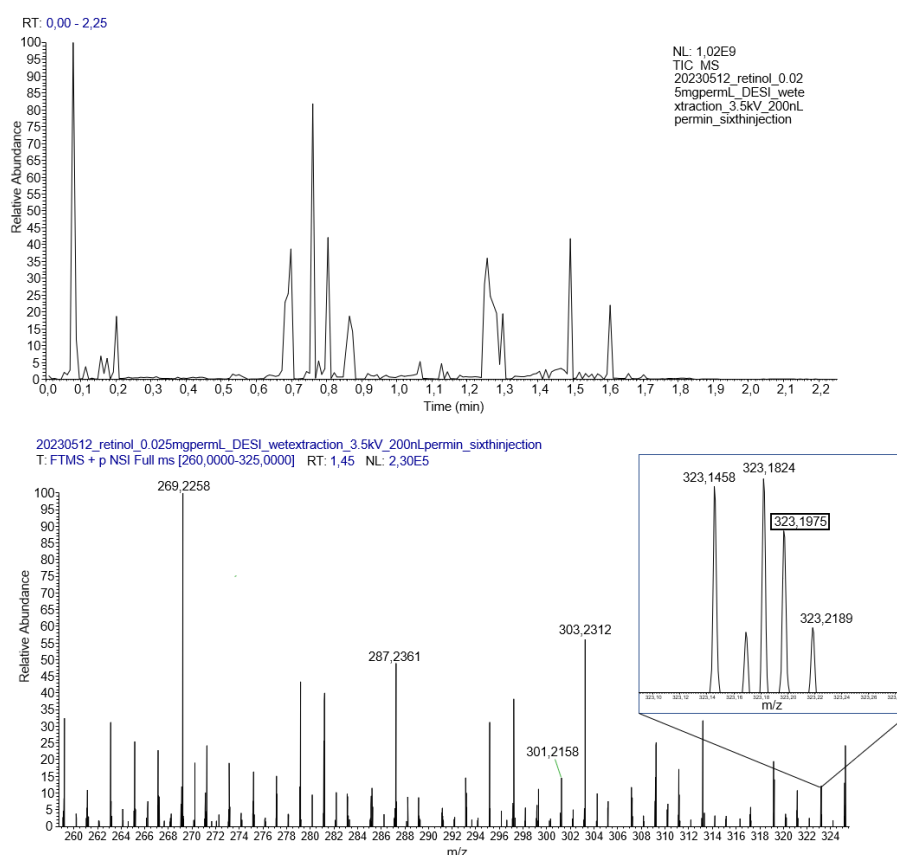


Figure 44. Top: the TIC acquired during desorption of a 0.025 mg/mL retinol solution from a glass slide. Bottom: mass spectrum after desorption of the same solution. The spectrum chosen is from only one single scan, because the analytes were only found sporadically.

The TIC acquired resembled that of the direct injection through the liquid bridge in its sudden burst in ion intensity. The analytes were not found at the highest ion peaks, but rather near the base line. The spectrum shown was the sixth acquired, but analytes were found in at least three of the previous experiments as well.

The base peak intensity resembles that found for direct infusion through liquid bridge. In the mass spectrum, five masses are labeled, all thought to be different forms of protonated retinoids. In **Table 18**, the nominal masses of these five retinoids are given, as well as a probable explanation for the type of retinoid and their mass accuracy in ppm.

Table 18. The table contains the nominal mass, molecular formula, name and type of ion, and the mass accuracy of the ions found when desorbing retinol solution from a glass slide.

<i>m/z</i>	Molecular formula	Compound	Mass accuracy (ppm)
269.2258	C ₂₀ H ₂₈	Protonated retinol minus water, [M+H-H ₂ O] ⁺	-2.14
287.2361	C ₂₀ H ₃₀ O	Protonated retinol, [M+H] ⁺	-2.93
301.2158	C ₂₀ H ₂₈ O ₂	Protonated retinoic acid, [M+H] ⁺	-1.35
303.2312	C ₂₀ H ₃₀ O ₂	Protonated hydroxyretinol, [M+H] ⁺	-0.85
323.1975	C ₂₀ H ₂₈ O ₂	Sodium adduct of retinoic acid, [M+Na] ⁺	-2.01

As shown, different forms of retinol were found. There seems to be an oxidation process, as retinoic acid and hydroxyretinol were found with a large certainty when looking at their mass accuracies. The sodium adduct of retinoic acid was found in a cluster of peaks around *m/z* 323, and the one with the lowest mass accuracy was annotated as the [M+Na]⁺ peak.

Although in only singular scans, retinol was detected. Other species previously not seen was detected as well, indicating some unknown oxidation process.

4.7.2 Retinoic acid

Figure 45 gives the TIC and mass spectrum obtained after desorbing a 0.025 mg/mL retinoic acid solution applied to a glass slide.

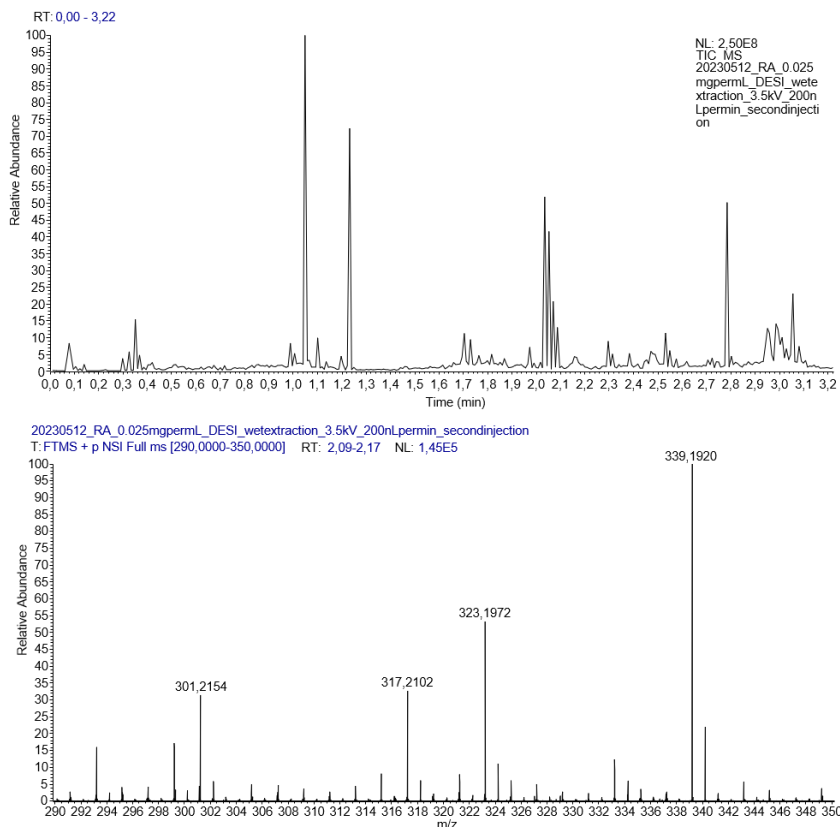


Figure 45. **Top:** the TIC obtained after desorption of retinoic acid. **Bottom:** mass spectrum obtained. Several species of retinoic acid and its variants were detected.

Once again, the TIC showed a behavior indicating sudden pockets of liquid being desorbed and ionized. This time, analytes were found in a couple of the bursts with adduct abundance resembling that in **Figure 41**, specifically those between 2.0 and 2.2 minutes.

The mass spectrum given indicates that at least four different types of retinoic acid ion variations were found. Their nominal masses, molecular formula, and a probable explanation of the type of ions is given in **Table 19**, along with their mass accuracy.

Table 19. The table contains the nominal mass, molecular formula, name and type of ion, and the mass accuracy of the ions found when desorbing retinoic acid solution from a glass slide.

<i>m/z</i>	Molecular formula	Compound	Mass accuracy (ppm)
301.2154	C ₂₀ H ₂₈ O ₂	Protonated retinoic acid, [M+H] ⁺	-0.81
317.2102	C ₂₀ H ₂₈ O ₃	Protonated X-hydroxyretinoic acid	-2.90
323.1972	C ₂₀ H ₂₈ O ₂	Sodium adduct of retinoic acid, [M+Na] ⁺	-2.94
339.1920	C ₂₀ H ₂₈ O ₂	Potassium adduct of retinoic acid, [M+Na] ⁺	58.71

The detected signal at m/z 317.2102 may have different origins with regards to compound. In general, a hydroxylated retinoic acid variant seems likely, but its position of hydroxylation remains uncertain. More than one isomer is possible. When typing the molecular formula in ChemSpider, some of the alternatives shown are 18-hydroxyretinoic acid and 4-hydroxyretinoic acid and demonstrate the type of viable stereoisomers. Their structures are given in **Figure 46**.

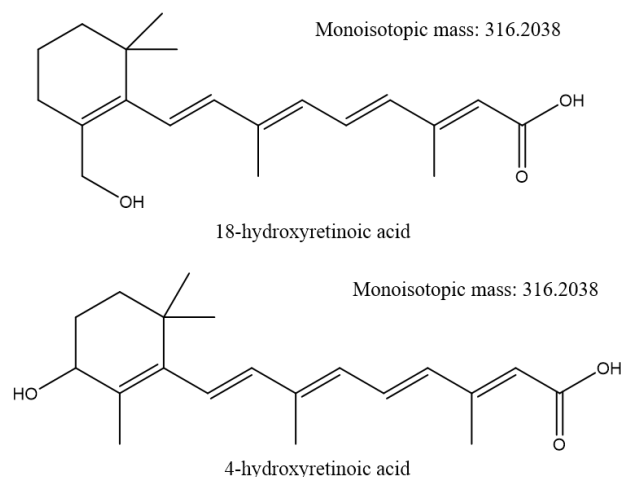


Figure 46. Two alternatives that may give rise to the detected signal in the mass spectrum at m/z 317.2102. Other hydroxylated variants and stereoisomers of retinoic acid might also occur.

The potassium variant detected is of high mass accuracy, and its annotation is uncertain. It is nevertheless included here because it was detected in previous injections with lower ppm-value.

Retinoic acid was desorbed and detected, along with other ion adducts and some hydroxylated variants.

4.7.3 Phosphatidylcholine

Figure 47 gives the TIC and mass spectrum obtained after desorption of a 0.025 mg/mL phosphatidylcholine solution from a glass slide.

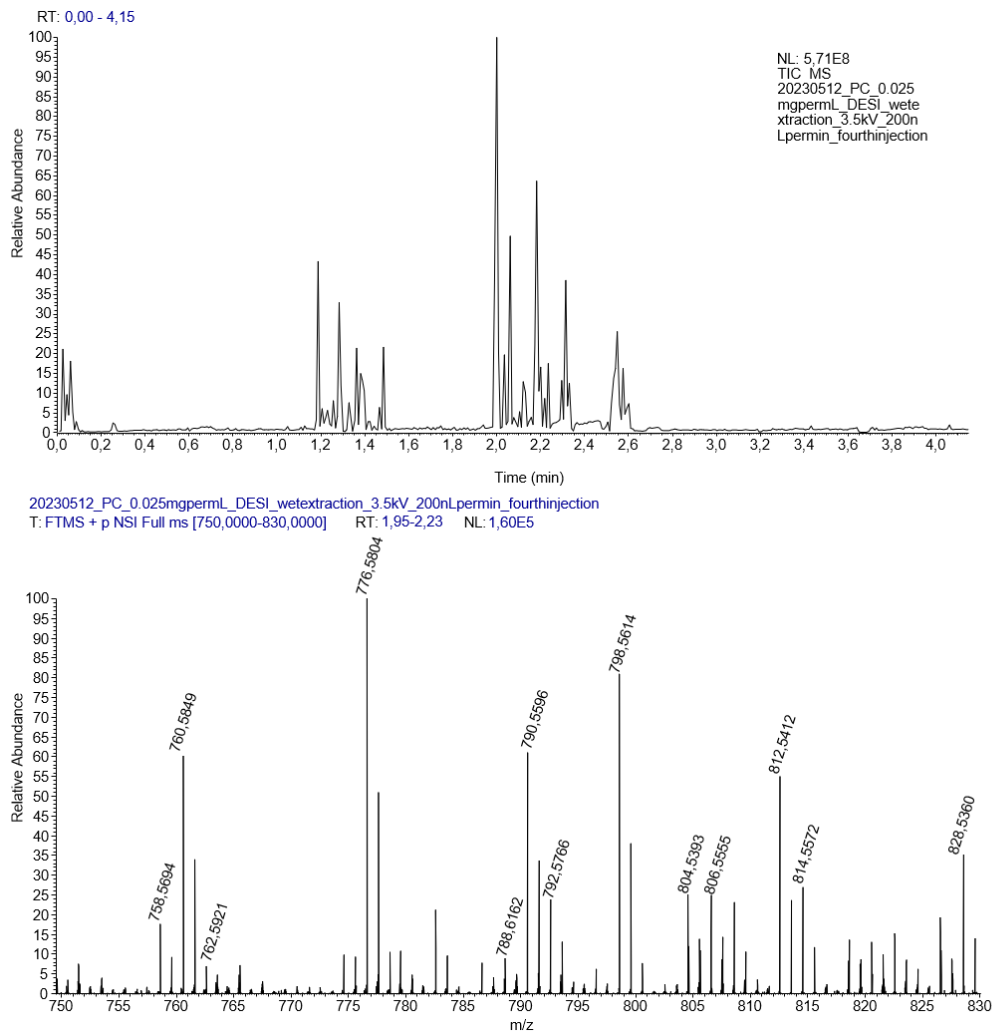


Figure 47. **Top:** the TIC obtained after desorption of a phosphatidylcholine solution from glass slide. **Bottom:** mass spectrum obtained. Several species of PC were detected. The top ten highest intensity peaks were included, along with m/z 758, 762, and 788 because they occurred in previous direct injections as well. Only the even-numbered peaks are labeled,

The TIC resembles those found from previous glass slide desorption experiments, with PC only found sporadically.

In the mass spectrum, the m/z of the ten highest intensity signals are given in addition to the peaks at m/z 758, 762, and 788 because of their importance and occurrence in previous direct

injections. **Table 20** lists the peaks of interest with their nominal masses, the most probable explanation, and their mass accuracy in ppm.

Table 20. The table contains the nominal mass, molecular formula, name and type of ion, and the mass accuracy of the ions found when desorbing phosphatidylcholine solution from a glass slide. Unless otherwise stated, the species are assumed protonated.

<i>m/z</i>	Compound	Mass accuracy (ppm)	<i>m/z</i>	Compound	Mass accuracy (ppm)
758	PC(34:2)	-0.03	798	PC(34:1)+K ⁺	25.59
760	PC(34:1)	-0.24	804	PC(38:7)	-18.00
762	PC(34:0)	-11.32	806	PC(38:6)	-17.27
776	PC(35:0)	-46.33	812	PC(35:1)+K ⁺	-18.97
788	PC(36:1)	-0.23	814	PC(37:0)+K ⁺	-18.49
790	PC(35:4)+Na ⁺	30.20	828	PC(38:6)+Na ⁺	-18.56
792	PC(37:6)	28.79	-	-	-

Many of the ions that were seen when injecting through the liquid bridge were also seen here. That is, they only appear when the liquid bridge is used.

Most of these compounds fell outside the mass accuracy range that the orbitrap normally delivers. Therefore, the identity of all the compounds that were above 5 ppm are questionable. For the ion at *m/z* 776.5804, another plausible solution would be an oxidated PC(34:1) variant, with molecular formula C₄₂H₈₂NO₉P. This would have a mass accuracy of 0.52 ppm.

However, PC(34:2), PC(34:1), and PC(36:1) followed consistency and were once again found with acceptable ppm-values. The source of the other compounds is unknown but may be due to some inherent effects of physical contact between the liquid being desorbed, and the emitter subjected to 3.5 kV.

PC(34:2), PC(34:1), and PC(36:1) were found with high confidence. Other compounds were questionable. Focus should be given mainly to these compounds in future analyses of cellular samples.

4.7.4 Phosphatidylglycerol was not analyzed due to problematic liquid bridge

From previous direct infusion through liquid bridge difficulties were experienced. This was thought to be because the negative mode ionization had some inherent disadvantages in the current system. Therefore, only the analytes ran in positive mode were subjected to desorption experiments.

4.7.5 General remarks after glass slide desorption

The analytes of interest were found when desorbing from the glass slides in all three experiments. However, it was done through manually steering the sample holder, which meant no consistent height adjustment. This may be the cause for the sudden change in TIC intensity, as the probe is only briefly positioned at the optimal height for analyte desorption.

Many other compounds not previously seen appeared during desorption. This indicates some inherent and repeating side effects of the system not yet clarified. One source may be the physical contact between the liquid being desorbed, and the emitter subject to 3.5 kV. This may cause some derivatizations in the analytes. Whether the method may still be called soft is also hard to tell, as the degree of fragmentation was not investigated.

4.8 Hepatic stellate cells were analyzed on the nano DESI platform

Hepatic stellate cells were analyzed to see if retinol could be desorbed, as these cells are retinol rich. Three groups of cells were analyzed: a control group, cells starved to deplete retinol, and cells fed TGF- β to increase secretion of retinol. It was expected that the TGF- β cells were the ones with the highest chance of displaying retinol.

No signals of any forms of retinol were found in any of the cell groups. As was seen when doing droplet desorption of retinol, a signal intensity of $\sim E5$ was found for a 0.025 mg/mL solution, which is a very high concentration. As to the author's knowledge, the concentration of retinol

in these cells are not known, and therefore, a theory is the concentration is too low for detection. Another reason may be the inherent ability of the nano DESI to desorb analytes. Other research groups use a flow of 500 nL/min, which will have a better desorption effect due to more solvent available. However, for this system with smaller ID emitters, using a flow of 500 nL/min was not tested. The failure may also arise from inaccurate steering of the probe, as it was manually operated.

Gastruloids were also planned analyzed by nano DESI. They were however imaged using MALDI, and the images are presented in **appendix 7.10**.

5 Conclusion

The capillary emitters produced were of satisfactory geometric size and shape when inspected in a light microscope. The methods used for production have up-scaling potential, and many emitters can be produced in parallel in both etching and ALD. When tested, all emitters were capable of ionizing analytes, giving a high signal intensity, and mostly hitting the 100% AGC target. This was also the case for experiments using the nano DESI platform. They did however have unstable TIC variation values.

Table 21 recapitulates the areas of focus when building the nano DESI platform, as given in **section 1.5.3**. An extra column is included stating what was implemented during this project, and what wasn't.

Table 21. The table lists the necessary parts of a functional nano DESI platform, as well as other factors that are used for optimization and testing at the various steps. It also shows what was implemented during the work of this thesis.

Component	Use	Planned	included in this thesis	Implemented
Base	Creating the space onto which other components are attached	Yes		✓
Primary capillary emitter	Electrically conductive emitter for delivery of desorption solvent onto sample	Yes		✓
Nanospray capillary emitter	Pick-up of solvent containing analyte for delivery to the MS	Yes		✓
Micro positioners	Fine positioning of emitters	Yes		✓
Microscope cameras	To ensure correct and optimal emitter position	Yes		✓
Sample holder	A frame where glass slides containing sample is put	Yes		✓
Motorized stages	Electrical and programmable stages to move the sample in a predetermined pattern in all three axes	Yes		✓
Control software for sample holder	A computer program to give the three stages instructions on where to move	Yes		✗
Height adjusting mechanism	To ensure constant probe-to-sample distance for optimal results	Yes		✗
Imaging conversion software	Software to convert all the acquired mass spectra to a single image	Yes		✗
Chemical standards	To do testing of the platform at each point of development	Yes		✓
Cellular samples	To see whether the system, when ready, can desorb analytes from cells (organoids, gastruloids, etc.)	Yes		✓

The instrument was assembled to the point where it could be steered manually and successfully desorb analytes deposited on a glass slide. Software for systematically controlling the sample holder, a height adjusting mechanism, and image conversion was not implemented. These are however not necessary to establish proof of function but will be necessary for organoid analysis, or analysis of other cell samples because of increased precision.

The desorption of analytes from hepatic stellate cells was tried but proved futile. Based on other work, it is believed possible.

Figure 48 graphically shows the parts of the project achieved and those excluded.

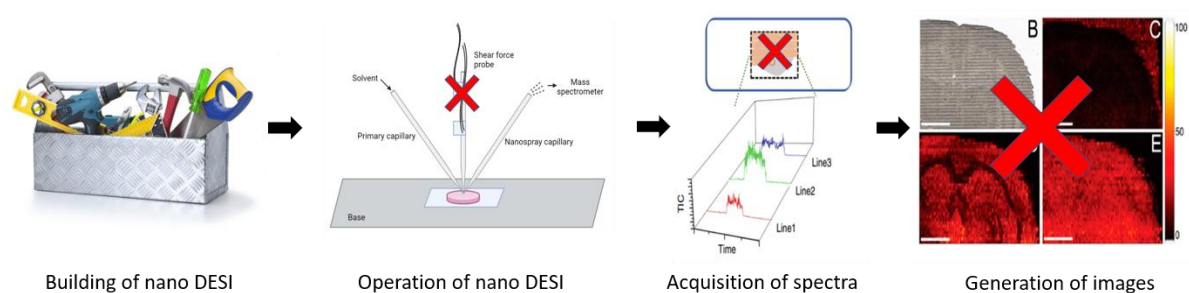


Figure 48. A graphical representation of the achieved and excluded parts of the project. The system was built using in-house produced emitters, but the shear force probe was not implemented. Spectra were acquired, but systematic scanning was omitted. Hence the red crosses on only parts of the figure.

Future work

One suggestion is thorough high-magnification inspection using scanning electron microscopy to assess the emitters' tips. This may disclose irregularities in symmetry and give further insight into what factors give the best emitters.

An automatic steering mechanism for the desorption probe should be implemented, as the very small distances are hard to control using manual steering. Also, if the amount of desorbed analytes from cell samples is below the LOD, having a higher flowrate lets more molecules be desorbed. These are also aspects of further development.

A height adjusting mechanism should be implemented, where shear force microscopy is an alternative. Another height adjusting mechanism, triangulation, may also be implemented as a medium-term solution as this requires less instrumental resources.

Installing a device to help flow of solvent and nebulization of analytes should also be of interest. Such a device is used in pneumatically assisted desorption. This requires a longer nanospray emitter (5-6 cm), and therefore a larger spatial footprint, but has advantages of increased suction forces through the NCE, better nebulization leading to a higher number of ions for detection, increasing *S/N*, broadens alternatives and compositional options of solvents, and might also give a more stable TIC variation which is one of the problems to overcome with this instrument.

6 References

1. Richards, T.W., *Modern Chemistry and Science*, in *The Atlantic*. 1909, The Atlantic Monthly Company: Boston.
2. Philip Rhodes, D.J.G., Robert G. Richardson, William Archibald Robson Thomson, E. Ashworth Underwood, *History of medicine*, in *Encyclopaedia Britannica*, E. Britannica, Editor. 2022, Encyclopaedia Britannica.
3. Pandey, S., et al., *Bioanalysis in drug discovery and development*. Pharm Methods, 2010. **1**(1): p. 14-24.
4. Keçili, R., S. Büyüktiryaki, and C.M. Hussain, *Advancement in bioanalytical science through nanotechnology: Past, present and future*. TrAC Trends in Analytical Chemistry, 2019. **110**: p. 259-276.
5. Hopfgartner, G. and E. Bourgoigne, *Quantitative high-throughput analysis of drugs in biological matrices by mass spectrometry*. Mass Spectrometry Reviews, 2003. **22**(3): p. 195-214.
6. Moein, M.M., A. El Beqqali, and M. Abdel-Rehim, *Bioanalytical method development and validation: Critical concepts and strategies*. Journal of Chromatography B, 2017. **1043**: p. 3-11.
7. Londhe, V. and M. Rajadhyaksha, *Opportunities and obstacles for microsampling techniques in bioanalysis: Special focus on DBS and VAMS*. Journal of Pharmaceutical and Biomedical Analysis, 2020. **182**: p. 113102.
8. Gallaher, D.D., *Animal Models in Human Nutrition Research*. Nutrition in Clinical Practice, 1992. **7**(1): p. 37-39.
9. McMahon, M. *What is a Biological Model?* 2022 01.10.2022 [cited 2022 13.10]; Available from: <https://www.allthescience.org/what-is-a-biological-model.htm>.
10. Rubio-Aliaga, I., *Model organisms in molecular nutrition research*. Molecular Nutrition & Food Research, 2012. **56**(6): p. 844-853.
11. Nainu, F., et al., *Editorial: Model organisms in experimental pharmacology and drug discovery 2022*. Frontiers in Pharmacology, 2023. **14**.
12. Taelman, J., M. Diaz, and J. Guiu, *Human Intestinal Organoids: Promise and Challenge*. Frontiers in Cell and Developmental Biology, 2022. **10**.
13. Kim, J., B.-K. Koo, and J.A. Knoblich, *Human organoids: model systems for human biology and medicine*. Nature Reviews Molecular Cell Biology, 2020. **21**(10): p. 571-584.
14. *Mass Spectrometry in Bioanalysis*. 2019 [cited 2022 03.10]; Available from: <https://lubrizolcdmo.com/technical-briefs/mass-spectrometry-in-bioanalysis/>.
15. Gross, J.H., *Mass Spectrometry*. 3 ed. 2017, Heidelberg: Springer.
16. Biosoft, P. *Mass spectrometry*. [cited 2023 10.04.23]; Available from: http://www.premierbiosoft.com/tech_notes/mass-spectrometry.html.
17. Klont, F. and G. Hopfgartner, *Mass spectrometry based approaches and strategies in bioanalysis for qualitative and quantitative analysis of pharmaceutically relevant molecules*. Drug Discovery Today: Technologies, 2021. **40**: p. 64-68.
18. Perry, R.H., R.G. Cooks, and R.J. Noll, *Orbitrap mass spectrometry: Instrumentation, ion motion and applications*. Mass Spectrometry Reviews, 2008. **27**(6): p. 661-699.
19. Makarov, A., *Electrostatic Axially Harmonic Orbital Trapping: A High-Performance Technique of Mass Analysis*. Analytical Chemistry, 2000. **72**(6): p. 1156-1162.
20. Eliuk, S. and A. Makarov, *Evolution of Orbitrap Mass Spectrometry Instrumentation*. Annual Review of Analytical Chemistry, 2015. **8**(1): p. 61-80.

21. Scigelova, M., et al., *Fourier Transform Mass Spectrometry*. Molecular & cellular proteomics : MCP, 2011. **10**: p. M111.009431.
22. Hu, Q., et al., *The Orbitrap: a new mass spectrometer*. Journal of Mass Spectrometry, 2005. **40**(4): p. 430-443.
23. Scigelova, M. and A. Makarov, *Orbitrap Mass Analyzer – Overview and Applications in Proteomics*. PROTEOMICS, 2006. **6**(S2): p. 16-21.
24. Savaryn, J., T. Toby, and N. Kelleher, *A researcher's guide to mass spectrometry - based proteomics*. PROTEOMICS, 2016. **16**.
25. Mcnaught, A.D. and A. Wilkinson, *The IUPAC Gold Book*. 1997, Blackwell Scientific Publications: Oxford.
26. Waters. *Select Series MRT*. 2023 [cited 2023 16.06]; Available from: https://www.waters.com/waters/en_US/SELECT-SERIES-MRT/nav.htm?locale=en_US&cid=135082877.
27. Makarov, A., et al., *Performance Evaluation of a Hybrid Linear Ion Trap/Orbitrap Mass Spectrometer*. Analytical Chemistry, 2006. **78**(7): p. 2113-2120.
28. Scientific, T. *Q Exactive Plus Hybrid Quadrupole-Orbitrap Mass Spectrometer Support – Getting Started*. [cited 2023 26.01]; Available from: <https://www.thermofisher.com/no/en/home/technical-resources/technical-reference-library/mass-spectrometry-support-center/liquid-chromatography-mass-spectrometry-instruments-support/q-exactive-plus-hybrid-quadrupole-orbitrap-mass-spectrometer-support/q-exactive-plus-hybrid-quadrupole-orbitrap-mass-spectrometer-support-getting-started.html>.
29. Skogvold, H.B., *Laboratory diagnostics: Maximizing sensitivity of a Q-Exactive Orbitrap mass spectrometer for untargeted metabolomics of dried blood spots*, in *Department of Chemistry*. 2017, University of Oslo: Oslo.
30. Lundanes, E.R., Léon; Greibrokk, Tyge, *Chromatography: basic principles, sample preparations, and related methods*. 3 ed. 2019, Oslo: Wiley-VCH.
31. Banerjee, S. and S. Mazumdar, *Electrospray Ionization Mass Spectrometry: A Technique to Access the Information beyond the Molecular Weight of the Analyte*. International journal of analytical chemistry, 2012. **2012**: p. 282574.
32. Rayleigh, L., *XX. On the equilibrium of liquid conducting masses charged with electricity*. The London, Edinburgh, and Dublin Philosophical Magazine and Journal of Science, 1882. **14**(87): p. 184-186.
33. Kebarle, P. and L. Tang, *From ions in solution to ions in the gas phase - the mechanism of electrospray mass spectrometry*. Analytical Chemistry, 1993. **65**(22): p. 972A-986A.
34. Felitsyn, N., M. Peschke, and P. Kebarle, *Origin and number of charges observed on multiply-protonated native proteins produced by ESI*. International Journal of Mass Spectrometry, 2002. **219**(1): p. 39-62.
35. Iribarne, J.V. and B.A. Thomson, *On the evaporation of small ions from charged droplets*. The Journal of Chemical Physics, 1976. **64**(6): p. 2287-2294.
36. Karas, M., U. Bahr, and T. Dülcks, *Nano-electrospray ionization mass spectrometry: addressing analytical problems beyond routine*. Fresenius' Journal of Analytical Chemistry, 2000. **366**(6): p. 669-676.
37. Kebarle, P., *A brief overview of the present status of the mechanisms involved in electrospray mass spectrometry*. Journal of Mass Spectrometry, 2000. **35**(7): p. 804-817.
38. Cooks, R.G., et al., *Ambient Mass Spectrometry*. Science, 2006. **311**(5767): p. 1566-1570.

39. Huang, M.-Z., et al., *Ambient Ionization Mass Spectrometry*. Annual Review of Analytical Chemistry, 2010. **3**(1): p. 43-65.
40. Takáts, Z., J.M. Wiseman, and R.G. Cooks, *Ambient mass spectrometry using desorption electrospray ionization (DESI): instrumentation, mechanisms and applications in forensics, chemistry, and biology*. Journal of Mass Spectrometry, 2005. **40**(10): p. 1261-1275.
41. Manikandan, M., et al., *Biological Desorption Electrospray Ionization Mass Spectrometry (DESI MS) – unequivocal role of crucial ionization factors, solvent system and substrates*. TrAC Trends in Analytical Chemistry, 2016. **78**: p. 109-119.
42. Weston, D.J., *Ambient ionization mass spectrometry: current understanding of mechanistic theory; analytical performance and application areas*. Analyst, 2010. **135**(4): p. 661-668.
43. Bodzon-Kulakowska, A., et al., *Desorption electrospray ionisation (DESI) for beginners – how to adjust settings for tissue imaging*. Rapid Communications in Mass Spectrometry, 2014. **28**(1): p. 1-9.
44. Takáts, Z., et al., *Direct, trace level detection of explosives on ambient surfaces by desorption electrospray ionization mass spectrometry*. Chemical Communications, 2005(15): p. 1950-1952.
45. Chen, H., et al., *Desorption electrospray ionization mass spectrometry for high-throughput analysis of pharmaceutical samples in the ambient environment*. Anal Chem, 2005. **77**(21): p. 6915-27.
46. Pan, Z., et al., *Principal component analysis of urine metabolites detected by NMR and DESI-MS in patients with inborn errors of metabolism*. Analytical and Bioanalytical Chemistry, 2007. **387**(2): p. 539-549.
47. Talaty, N., Z. Takáts, and R.G. Cooks, *Rapid in situ detection of alkaloids in plant tissue under ambient conditions using desorption electrospray ionization*. Analyst, 2005. **130**(12): p. 1624-1633.
48. Wiseman, J.M., et al., *Mass Spectrometric Profiling of Intact Biological Tissue by Using Desorption Electrospray Ionization*. Angewandte Chemie International Edition, 2005. **44**(43): p. 7094-7097.
49. Bodzon-Kulakowska, A., et al., *DESI-MS as a tool for direct lipid analysis in cultured cells*. Cytotechnology, 2015. **67**(6): p. 1085-91.
50. Yin, R., et al., *High spatial resolution imaging of biological tissues using nanospray desorption electrospray ionization mass spectrometry*. Nature Protocols, 2019. **14**(12): p. 3445-3470.
51. Murphy, S.E. and J.V. Sweedler, *Metabolomics-based mass spectrometry methods to analyze the chemical content of 3D organoid models*. Analyst, 2022. **147**(13): p. 2918-2929.
52. Bodzon-Kulakowska, A. and P. Suder, *Imaging mass spectrometry: Instrumentation, applications, and combination with other visualization techniques*. Mass Spectrometry Reviews, 2016. **35**(1): p. 147-169.
53. Caprioli, R.M., T.B. Farmer, and J. Gile, *Molecular Imaging of Biological Samples: Localization of Peptides and Proteins Using MALDI-TOF MS*. Analytical Chemistry, 1997. **69**(23): p. 4751-4760.
54. Kompauer, M., S. Heiles, and B. Spengler, *Atmospheric pressure MALDI mass spectrometry imaging of tissues and cells at 1.4- μ m lateral resolution*. Nat Methods, 2017. **14**(1): p. 90-96.
55. Lanekoff, I., et al., *Automated Platform for High-Resolution Tissue Imaging Using Nanospray Desorption Electrospray Ionization Mass Spectrometry*. Analytical Chemistry, 2012. **84**(19): p. 8351-8356.

56. SINTEF. *Piezoelectric materials for sensors, actuators and ultrasound transducers*. 2022 [cited 2022 07.02.2022]; Available from: <https://www.sintef.no/en/expertise/sintef-industry/materials-and-nanotechnology/piezoelectric-materials-for-sensors-actuators-and-ultrasound-transducers/>.
57. Kelly, R.T., et al., *Chemically Etched Open Tubular and Monolithic Emitters for Nanoelectrospray Ionization Mass Spectrometry*. *Analytical Chemistry*, 2006. **78**(22): p. 7796-7801.
58. Bergman, H.-M. and I. Lanekoff, *Profiling and quantifying endogenous molecules in single cells using nano-DESI MS*. *Analyst*, 2017. **142**(19): p. 3639-3647.
59. Laiko, V.V., S.C. Moyer, and R.J. Cotter, *Atmospheric Pressure MALDI/Ion Trap Mass Spectrometry*. *Analytical Chemistry*, 2000. **72**(21): p. 5239-5243.
60. Laskin, J. and I. Lanekoff, *Ambient Mass Spectrometry Imaging Using Direct Liquid Extraction Techniques*. *Analytical Chemistry*, 2016. **88**(1): p. 52-73.
61. Mueller, P. and J. Vervoort. *Secondary Ion Mass Spectrometer (SIMS)*. 2022 24.10.2022 [cited 2022 31.10]; Available from: https://serc.carleton.edu/msu_nanotech/methods/SIMS.html.
62. Nemes, P. and A. Vertes, *Laser Ablation Electrospray Ionization for Atmospheric Pressure, in Vivo, and Imaging Mass Spectrometry*. *Analytical Chemistry*, 2007. **79**(21): p. 8098-8106.
63. PepSep. [cited 2022 06.09]; Available from: <https://www.mswil.com/nano-cap-micro-ic/spray-emitters/tapered-emitters/pepsep-nesi-emitters/>.
64. FossilIonTech. [cited 2022 06.09]; Available from: <https://www.fossiliontech.com/nanoesi-emitters>.
65. Reschke, B.R. and A.T. Timperman, *A Study of Electrospray Ionization Emitters with Differing Geometries with Respect to Flow Rate and Electrospray Voltage*. *Journal of The American Society for Mass Spectrometry*, 2011. **22**(12): p. 2115-2124.
66. Guo, X., et al., *Capillary Electrophoresis-Nanoelectrospray Ionization-Selected Reaction Monitoring Mass Spectrometry via a True Sheathless Metal-Coated Emitter Interface for Robust and High-Sensitivity Sample Quantification*. *Anal Chem*, 2016. **88**(8): p. 4418-25.
67. Zhu, X., et al., *Gold-Coated Nanoelectrospray Emitters Fabricated by Gravity-Assisted Etching Self-Termination and Electroless Deposition*. *Anal Chem*, 2016. **88**(23): p. 11347-11351.
68. Kogler, S., *Evaluation of methods for etching and coating of nanoelectrospray emitters*, in *Department of Chemistry*. 2017, University of Oslo: Oslo, Norway. p. 45.
69. Kogler, S., *On-line "Organ-in-a-Column" Liquid Chromatography Electrospray Ionization Mass Spectrometry for Drug Metabolism Studies*, in *Department of Chemistry*. 2019, University of Oslo: Oslo. p. 107.
70. Selte, K., *Lærebok i Uorganisk Kjemi*. 1982, Oslo: Tanum-Norli.
71. Emmett, M.R. and R.M. Caprioli, *Micro-electrospray mass spectrometry: ultra-high-sensitivity analysis of peptides and proteins*. *Journal of the American Society for Mass Spectrometry*, 1994. **5**(7): p. 605-613.
72. M. Moini, P.U.S.C., *Patent 6,863,790*. 2005.
73. Midtøy, L., *An evaluation of in-house produced nanoelectrospray emitters regarding preparation and performance*, in *Department of Chemistry*. 2021, University of OSlo: Oslo. p. 50.
74. Richey, N.E., C.d. Paula, and S.F. Bent, *Understanding chemical and physical mechanisms in atomic layer deposition*. *The Journal of Chemical Physics*, 2020. **152**(4): p. 040902.

75. Cheng, H.-E., D.-C. Tian, and K.-C. Huang, *Properties of SnO₂ Films Grown by Atomic Layer Deposition*. Procedia Engineering, 2012. **36**: p. 510–515.
76. Nazarov, D., et al., *Atomic layer deposition of tin dioxide nanofilms: A review*. Reviews on advanced materials science, 2015. **40**: p. 262-275.
77. Maden, M., *Retinoid signalling in the development of the central nervous system*. Nature Reviews Neuroscience, 2002. **3**(11): p. 843-853.
78. *Vitamin A: foods, functions, how much do you need & more*. 2021 [cited 2023 17.01]; Available from: <https://www.eufic.org/en/vitamins-and-minerals/article/vitamin-a-foods-functions-how-much-do-you-need-and-more>.
79. Niederreither, K. and P. Dollé, *Retinoic acid in development: towards an integrated view*. Nature Reviews Genetics, 2008. **9**(7): p. 541-553.
80. Carazo, A., et al., *Vitamin A Update: Forms, Sources, Kinetics, Detection, Function, Deficiency, Therapeutic Use and Toxicity*. Nutrients, 2021. **13**(5).
81. Ross, A.C., *Vitamin A*, in *Bioactive Compounds and Cancer*, J.A. Milner and D.F. Romagnolo, Editors. 2010, Humana Press: Totowa, NJ. p. 335-356.
82. Alberts B, J.A., Lewis J, *Molecular biology of the Cell*. 4th ed. 2002, New York: Garland Science.
83. van der Veen, J.N., et al., *The critical role of phosphatidylcholine and phosphatidylethanolamine metabolism in health and disease*. Biochimica et Biophysica Acta (BBA) - Biomembranes, 2017. **1859**(9, Part B): p. 1558-1572.
84. Milo, R. and R. Phillips, *Cell biology by the numbers, in What lipids are the most abundant in membranes?*
85. Jonas, A. and M.C. Phillips, *CHAPTER 17 - Lipoprotein structure*, in *Biochemistry of Lipids, Lipoproteins and Membranes (Fifth Edition)*, D.E. Vance and J.E. Vance, Editors. 2008, Elsevier: San Diego. p. 485-506.
86. Zhao, W., et al., *Role of phosphatidylglycerols in the stability of bacterial membranes*. Biochimie, 2008. **90**(6): p. 930-8.
87. Christie, W.W. *Phosphatidylglycerol and Related Lipids*. 2022 [cited 2023 19.01]; Available from: https://www.lipidmaps.org/resources/lipidweb/lipidweb_html/lipids/complex/pg/index.htm.
88. King, R.J. and M.C. MacBeth, *Interaction of the lipid and protein components of pulmonary surfactant Role of phosphatidylglycerol and calcium*. Biochimica et Biophysica Acta (BBA) - Biomembranes, 1981. **647**(2): p. 159-168.
89. Muller, M.P., et al., *Characterization of Lipid-Protein Interactions and Lipid-Mediated Modulation of Membrane Protein Function through Molecular Simulation*. Chem Rev, 2019. **119**(9): p. 6086-6161.
90. McCaffery, P., et al., *Retinoid quantification by HPLC/MSn*. Journal of Lipid Research, 2002. **43**(7): p. 1143-1149.
91. Van Breemen, R.B. and C.-R. Huang, *High-performance liquid chromatography–electrospray mass spectrometry of retinoids*. The FASEB Journal, 1996. **10**(9): p. 1098-1101.
92. Peng, J.-B., et al., *Validation of a Liquid Chromatography-Electrospray Ionization-Tandem Mass Spectrometry Method for Determination of All-Trans Retinoic Acid in Human Plasma and Its Application to a Bioequivalence Study*. Molecules, 2014. **19**(1): p. 1189-1200.
93. Szuhaj, B.F., *PHOSPHOLIPIDS | Properties and Occurrence*, in *Encyclopedia of Food Sciences and Nutrition (Second Edition)*, B. Caballero, Editor. 2003, Academic Press: Oxford. p. 4514-4519.

94. Okano, G. and T. Akino, *Variations in the molecular species of lung phosphatidylglycerol*. *Lipids*, 1979. **14**(6): p. 541-546.
95. Hsu, F.-F. and J. Turk, *Studies on phosphatidylglycerol with triple quadrupole tandem mass spectrometry with electrospray ionization: fragmentation processes and structural characterization*. *Journal of the American Society for Mass Spectrometry*, 2001. **12**(9): p. 1036-1043.
96. Yin, C., et al., *Hepatic stellate cells in liver development, regeneration, and cancer*. *J Clin Invest*, 2013. **123**(5): p. 1902-10.
97. Haavaag, J.E., *Questions about TGF beta*, I. Wilhelmson, Editor. 2023.
98. Rossi, G., et al., *Gastruloids as in vitro models of embryonic blood development with spatial and temporal resolution*. *Scientific Reports*, 2022. **12**(1): p. 13380.
99. Rossi, G., A. Manfrin, and M.P. Lutolf, *Progress and potential in organoid research*. *Nature Reviews Genetics*, 2018. **19**(11): p. 671-687.
100. Yin, R., et al., *High Spatial Resolution Imaging of Mouse Pancreatic Islets Using Nanospray Desorption Electrospray Ionization Mass Spectrometry*. *Analytical Chemistry*, 2018. **90**(11): p. 6548-6555.
101. Patiny, L. and A. Borel, *ChemCalc: A Building Block for Tomorrow's Chemical Infrastructure*. *Journal of Chemical Information and Modeling*, 2013. **53**(5): p. 1223-1228.
102. Lipids, A.P., *Soy PG*, F.a. distribution, Editor.
103. Merck, *LC-MS Contaminants*. 2017, Merck KGaA: Darmstadt.
104. Duncan, K.D., H.-M. Bergman, and I. Lanekoff, *A pneumatically assisted nanospray desorption electrospray ionization source for increased solvent versatility and enhanced metabolite detection from tissue*. *Analyst*, 2017. **142**(18): p. 3424-3431.
105. Marín, Á.G. and D. Lohse, *Building water bridges in air: Electrohydrodynamics of the floating water bridge*. *Physics of Fluids*, 2010. **22**(12): p. 122104.
106. Fuchs, E.C., et al., *The floating water bridge*. *Journal of Physics D: Applied Physics*, 2007. **40**(19): p. 6112.
107. Donahue, S.W., *Krogh's principle for musculoskeletal physiology and pathology*. *J Musculoskelet Neuronal Interact*, 2018. **18**(3): p. 284-291.
108. Daniel, H., et al., *The challenges for molecular nutrition research 3: comparative nutrigenomics research as a basis for entering the systems level*. *Genes & Nutrition*, 2008. **3**(3): p. 101-106.
109. *Krogh's principle for a new era*. *Nature Genetics*, 2003. **34**(4): p. 345-346.
110. Huch, M. and B.-K. Koo, *Modeling mouse and human development using organoid cultures*. *Development*, 2015. **142**(18): p. 3113-3125.
111. Evans, M.J. and M.H. Kaufman, *Establishment in culture of pluripotential cells from mouse embryos*. *Nature*, 1981. **292**(5819): p. 154-156.
112. Martin, G.R., *Isolation of a pluripotent cell line from early mouse embryos cultured in medium conditioned by teratocarcinoma stem cells*. *Proceedings of the National Academy of Sciences*, 1981. **78**(12): p. 7634-7638.
113. Blau, H.M., C.-P. Chiu, and C. Webster, *Cytoplasmic activation of human nuclear genes in stable heterocaryons*. *Cell*, 1983. **32**(4): p. 1171-1180.
114. Chung, Young G., et al., *Human Somatic Cell Nuclear Transfer Using Adult Cells*. *Cell Stem Cell*, 2014. **14**(6): p. 777-780.
115. Xu, H., et al., *Organoid technology and applications in cancer research*. *Journal of Hematology & Oncology*, 2018. **11**(1): p. 116.
116. Xu, H., et al., *Organoid technology in disease modelling, drug development, personalized treatment and regeneration medicine*. *Exp Hematol Oncol*, 2018. **7**: p. 30.

117. [cited 2022 25.10]; Available from: <https://www.nc3rs.org.uk/who-we-are/3rs>.
118. Au - Gabriel, E. and J. Au - Gopalakrishnan, *Generation of iPSC-derived Human Brain Organoids to Model Early Neurodevelopmental Disorders*. JoVE, 2017(122): p. e55372.
119. Au - Bartfeld, S. and H. Au - Clevers, *Organoids as Model for Infectious Diseases: Culture of Human and Murine Stomach Organoids and Microinjection of Helicobacter Pylori*. JoVE, 2015(105): p. e53359.
120. Liu, J., et al., *Organoid: Next-Generation Modeling of Cancer Research and Drug Development*. Frontiers in Oncology, 2022. **11**.
121. Li, H. and A.B. Hummon, *Imaging Mass Spectrometry of Three-Dimensional Cell Culture Systems*. Analytical Chemistry, 2011. **83**(22): p. 8794-8801.
122. Flint, L.E., et al., *Characterization of an Aggregated Three-Dimensional Cell Culture Model by Multimodal Mass Spectrometry Imaging*. Analytical Chemistry, 2020. **92**(18): p. 12538-12547.
123. Harvey, A., et al., *MALDI-MSI for the analysis of a 3D tissue-engineered psoriatic skin model*. PROTEOMICS, 2016. **16**(11-12): p. 1718-1725.
124. Kessner, D., et al., *ProteoWizard: open source software for rapid proteomics tools development*. Bioinformatics, 2008. **24**(21): p. 2534-6.
125. Race, A.M., I.B. Styles, and J. Bunch, *Inclusive sharing of mass spectrometry imaging data requires a converter for all*. Journal of Proteomics, 2012. **75**(16): p. 5111-5112.
126. Bokhart, M.T., et al., *MSiReader v1.0: Evolving Open-Source Mass Spectrometry Imaging Software for Targeted and Untargeted Analyses*. J Am Soc Mass Spectrom, 2018. **29**(1): p. 8-16.
127. Nguyen, S.N., et al., *Towards High-Resolution Tissue Imaging Using Nanospray Desorption Electrospray Ionization Mass Spectrometry Coupled to Shear Force Microscopy*. Journal of the American Society for Mass Spectrometry, 2018. **29**(2): p. 316-322.

7 Appendix

7.1 Elaborating on bioanalytical method development

A process where the procedure given in **Figure 1** is often followed is drug development. In these cases, the studies aim towards undergoing clinical testing involving humans. Therefore, the evaluation of the toxicological, pharmacokinetic, and pharmacodynamic properties of the drug in question and its related metabolites is vital for the drug development process to proceed to clinical testing. There are however still instances where all the steps in the procedure do not always have to be rigorously followed. For instance, if a sample is taken at the laboratory as is the case for blood samples taken from animals, following the step for field pre-treatment (step 2) is irrelevant as one can go directly to laboratory treatment (step 3).

7.2 Expanding on the versatility of model organisms

In 1929, physician August Krogh postulated that: “For a large number of [physiological] problems there will be some animal of choice, or a few such animals, on which it can be most conveniently studied”. This was later termed the Krogh principle by Hans Krebs [107]. However, even if a fitting animal model would exist, finding it and making it a suitable model organism is nevertheless a challenge. In functional genomics studies for instance, this mission becomes more difficult with regards to applicability, feasibility, and cost with increasing genetic, morphological, functional, and nutritional complexity [108].

Two or more models might in some cases be used in parallel or as complementation to each other. Because of evolutionary conservation, geneticists easily move on from organism to organism within the same line of work, and it has in recent times been thought that a combination of two or more models will be more beneficial. In some cases, the more organisms involved, the better in supporting the converging line of evidence. To illustrate, Ewart-Toland et.al. studied the gene encoding Aurora2, which was identified as a candidate for tumor-

susceptibility for mice and humans. Linkage analysis, haplotype mapping, and expression analysis in mice narrowed the region down to a single gene, and subsequent functional analysis of the human locus jointly suggested that a specific isoleucine variant of Aurora2 was active in cancer susceptibility [109]. In this way, mice and human cells were both used to explore the gene types responsible for Aurora2.

7.3 The development of organoids and its uses in science

Organoids are mostly derived from either embryonic stem cells (ESC), induced pluripotent stem cells, or adult stem cells (AdSC), and from the year of 2000 extensive research has been conducted to develop organoids mimicking different types of tissues and organs [110]. The stem cells have different origins, with ESCs being isolated from the inner cell mass of blastocysts and cultured, as have been done with mice since the 80's [111, 112]. The use of somatic cells in making iPSC have been demonstrated for many decades, with different techniques being implemented with time. In 1983, Blau et.al. used cell fusion to give non-muscle cells a stable expression of muscle-specific genes [113], and in 2014 Chung et.al. published an article showing their success in using nuclear transfer to generate human iPSC from dermal fibroblasts from 35 and 75 year old males [114]. Whether the cells have been grown in vitro from ESC, iPSC, or AdSC, the cells can be differentiated back into somatic cells in vitro and grown as organoids given right growth medium [110]. **Figure 49** shows the general flow of organoid production and growth.

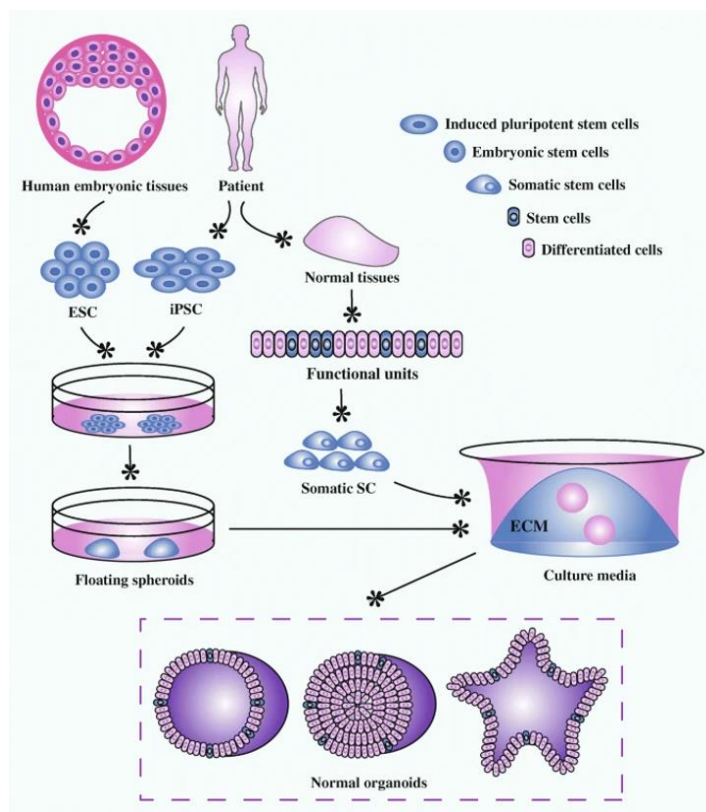
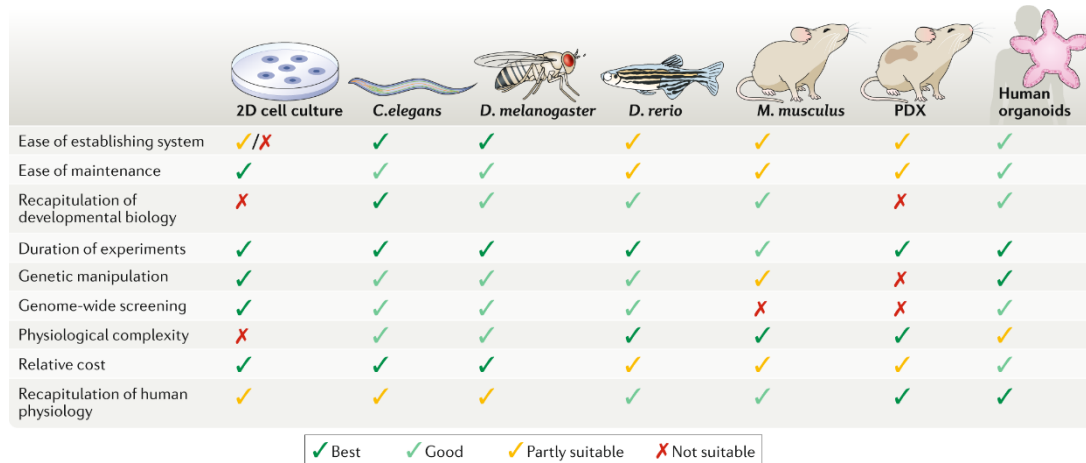


Figure 49. The different pathways of organoid development. Different types of human cells can be used to make organoids, using diverse methods. Figure is adapted from “Organoid technology and applications in cancer research” [115].

This scientific field as a whole has an enormous amount of unearthed potential linked to research on organ and tissue development, modeling and predictions of disease development, drug efficiency studies, personalized and regeneration medicine, and organ transplantations [116]. In animal testing, there is focus on replacement, reduction, and refinement of these animals, often referred to as the 3 R’s which sheds light upon the need for improvement when doing tests. One wishes to avoid the use of animals where possible or replace them with better and more sustainable models, reduce the total number of animals used, and minimize the effect inflicted upon the animals during testing [117]. Because organoids are generally well-suited models, they can also be used to fulfill these 3 R’s. A comparison of organoids versus other model organisms can be seen in **Figure 50**.



	2D cell culture	C. elegans	D. melanogaster	D. rerio	M. musculus	PDX	Human organoids
Ease of establishing system	✓/✗	✓	✓	✓	✓	✓	✓
Ease of maintenance	✓	✓	✓	✓	✓	✓	✓
Recapitulation of developmental biology	✗	✓	✓	✓	✓	✗	✓
Duration of experiments	✓	✓	✓	✓	✓	✓	✓
Genetic manipulation	✓	✓	✓	✓	✓	✗	✓
Genome-wide screening	✓	✓	✓	✓	✗	✗	✓
Physiological complexity	✗	✓	✓	✓	✓	✓	✓
Relative cost	✓	✓	✓	✓	✓	✓	✓
Recapitulation of human physiology	✓	✓	✓	✓	✓	✓	✓

✓ Best ✓ Good ✓ Partly suitable ✗ Not suitable

Figure 50. The figure compares the suitability of different model organisms, with respect to some of the most important parameters. From “Human organoids: model systems for human biology and medicine” [13]

To exemplify the use of organoids in science, Gabriel et. al. generated iPSC-derived human brain organoids to study the human neurodevelopmental disorder autosomal recessive primary microcephaly (MCPH) which causes brain malformation during early fetal development. The recreation of MCPH in vitro is difficult to carry out, but through the use of 3D brain organoids stemming from iPSC carrying a genetic mutation in a centrosomal gene relevant for development of MCPH they were nevertheless successful in proving premature cell differentiation. They are confident that brain organoids will be important tools in modelling brain disorders in the future [118].

Host-pathogen interactions were also studied by Bartfeld et. al., using AdSC to culture human and mouse gastric organoids. These were then injected with the pathogenic bacteria *Helicobacter pylori*, which is sometimes related to gastric cancer. Current cellular models lack a complete representation of infection and cancer development, especially when using cancer cell lines, as these are already at the endpoint of disease development. Gastric organoids are therefore better models, as they are non-transformed cells through which the complete transformation can be monitored [119].

Organoids are still not always the best of models or tools, as their development lack some of the factors contributing the intricacy of an endogenous biologic system. Liu et. al. confirms this through their work on development of colorectal cancer organoids and points out challenges related to the complexity of the hard-to-replicate extracellular matrix and its composition, and a low degree of controllability in this environment. They also recognize that the lack of different

cell types in the growth milieu, such as mesenchymal cells and immune cells, affect the organoid's development due to the absence of their influence. They thus don't have the same growth conditions as endogenous cancer cells have, and will therefore not be identical to regular colorectal cancer cells [120].

With respect to imaging studies, studies have been done on organoids or similar 3D cell culture systems. Of interest, Li and Hummon's pioneering 2011-study characterizing the spatial distribution of the protein HCT116 in colon carcinoma models using MALDI mass spectrometric imaging for the first time [121], as well as the more recent work of Flint et al. to map metabolites of the TCA cycle (e.g., lactate, glutamine, and citrate) in the hypoxic environment of HCC827 aggregoids using DESI mass spectrometric imaging [122] can be mentioned. Also, an imaging study was conducted by Harvey et al. on living skin equivalents (LSE), developed through self-assembling of human skin cells into stratified layers. This 3D-model is developed following much the same principles as development of organoids. After induction of psoriasis through addition of interleukin-22, MALDI-imaging was used to model the treatment with the drug acetrein through spatial mapping following 48 hours after treatment [123].

With respect to Krogh's principle, organoids can fulfill this not only by being a model on which several conditions can be most conveniently studied, but also most accurately. The principle would also have to be restated, as animals are no longer what is required to do studies, emphasizing again organoids' fulfillment of the three R's.

7.4 A data processing procedure can be used to graphically represent spectra as images

After having acquired mass spectra from imaging experiments, the data files can be fed into a sequence of different software to produce the images. Using a Thermo QExactive instrument, as in this thesis, the files come out in the RAW format. These files can be converted mzML format using the msConvert tool from Proteowizard [124], before being converted to imzML format using imzMLConverter [125]. The imzML files can be loaded into MSiReader for graphical representation of the spectra [126].

7.5 Parameters to determine before using shear force microscopy

Determination of the frequency with which the SFP ought to oscillate can be done by acquiring a probe excitation spectrum for the SFP in air and in contact with the sample surface. The difference in amplitude in the two mediums can be calculated, and the frequency value where the difference is largest can be chosen as the oscillation frequency for the SFP. After determination of the frequency, a plot can be made with amplitude as a function of probe-to-sample distance. To do this, the SFP is slowly moved towards the sample surface, oscillating at the frequency previously obtained, and an increase in voltage, that is amplitude, is detected. There will be an increase in oscillation amplitude as the probe nears the sample, which is a result of the induced resistance in the needle due to contact with the sample surface. The amplitude is then forced to increase, to keep the frequency constant. The amplitude to be used in the experiment can be set to 80% of the maximum achieved value, with its corresponding distance from the sample. This is to ensure that the needle is as close to the sample as possible for more precise topographic measurement, but still have a margin of movement [50, 127]. **Figure 51** shows an excitation and probe-to-sample spectrum obtained by Yin et. al. [100].

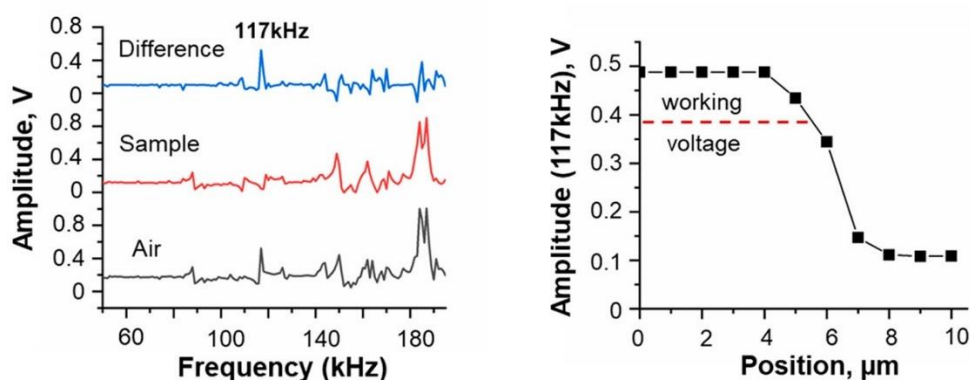


Figure 51. **Left:** an excitation spectrum with the SFP in air and on the sample. The difference in amplitude is greatest at 117 kHz. **Right:** the frequency is set to 117 kHz as previously determined, and the amplitude is measured as a function of probe-to-sample distance. The maximum value is to 0,49 V. Therefore, an amplitude value of 0,39 V (80% of 0,49 V). Adapted from “High spatial resolution imaging of mouse pancreatic islets using nanospray desorption electrospray ionization mass spectrometry” [100].

7.6 Analyte standards dilution table

Table 22. Standards of retinol, retinoic acid, phosphatidylcholine, and phosphatidylglycerol were made and analyzed with direct injection in a QExactive Orbitrap MS to predict the signal that may arise from organoid analysis of these compounds. Retinol had a hard time being dissolved, and was therefore prepared different from the others. End concentrations was in all cases 300 ng/mL.

Substance	First dilution	Second dilution	Third dilution	Fourth dilution	Fifth dilution	Sixth dilution
Retinol	25 mg in 1 mL methanol	100 μ L dissolved in 900 μ L methanol for 2.5 mg/mL	100 μ L dissolved in 900 μ L methanol for 0.25 mg/mL	100 μ L dissolved in 900 μ L methanol for 0.025 mg/mL	100 μ L dissolved in 900 μ L methanol for 0.0025 mg/mL	120 μ L dissolved in 780 μ L methanol and 100 μ L water for 300 ng/mL
Retinoic acid	50 mg in 1 mL methanol for 50 mg/mL	50 μ L dissolved in 950 μ L methanol for 2.5 mg/mL	100 μ L dissolved in 900 μ L methanol for 0.25 mg/mL	100 μ L dissolved in 900 μ L methanol for 0.025 mg/mL	100 μ L dissolved in 900 μ L methanol for 0.0025 mg/mL	120 μ L dissolved in 780 μ L methanol and 100 μ L water for 300 ng/mL
Phosphatidylcholine	25 mg in 1 mL methanol	100 μ L dissolved in 900 μ L methanol for 2.5 mg/mL	100 μ L dissolved in 900 μ L methanol for 0.25 mg/mL	100 μ L dissolved in 900 μ L methanol for 0.025 mg/mL	100 μ L dissolved in 900 μ L methanol for 0.0025 mg/mL	120 μ L dissolved in 780 μ L methanol and 100 μ L water for 300 ng/mL
Phosphatidylglycerol	25 mg in 1 mL water	100 μ L dissolved in 900 μ L water for 2.5 mg/mL	100 μ L dissolved in 900 μ L water for 0.25 mg/mL	100 μ L dissolved in 900 μ L water for 0.025 mg/mL	100 μ L dissolved in 900 μ L water for 0.0025 mg/mL	120 μ L dissolved in 1080 μ L methanol for 250 ng/mL

7.7 Elaborating on the suboptimal making of analyte solutions

The analyte solutions were made in a suboptimal manner. The target concentrations of the prepared analyte standards of retinol, retinoic acid, phosphatidylcholine was 300 ng/mL, while for phosphatidylglycerol it was 250 ng/mL. However, in every powder container, a very small amount of substance was left and couldn't be fully transferred to the solution container making the concentration lower than the calculated value.

In the case of retinoic acid, the reliability was even lower. A miscalculation was made, which made the end concentration 600 ng/mL. Also, it was expected that retinoic acid would have about the same solubility as retinol. This was not the case. After attempting to dissolve 50 mg in 2 mL methanol and relying on a solubility of at least 25 mg/mL, it was quickly discovered

that retinol would require more solvent. The solution was therefore transferred from a 2 mL PCR-tube to a 15 mL falcon tube to try using more methanol. Eventually, after adding methanol up to 15 mL, the solution was transferred to a 40 mL falcon tube. The powder was fully dissolved when a total of 25 mL of methanol was used. Because of these unfortunate transfers, much of the substance was lost on the way, especially from the 2 mL PCR-tube to the 15 mL falcon tube. The exact loss was not determined. The end concentration of 600 ng/mL was not taken to be reliable but will nevertheless be labeled a 600 ng/mL solution in later experiments.

7.8 Table showing signal intensity, TIC variation, and AGC target value for 14 tested emitters

Table 23 shows the signal intensity, TIC variation, and AGC target value achieved for the 14 emitters that could successfully produce an electrospray.

Table 23. The table shows the identifier of the emitters where a spray was achieved. The identifier includes the date of etching, the inner diameter, and an identification number to separate emitters etched on the same date with the same inner diameter. The signal intensity, TIC variation, and AGC target are also given for each emitter.

Emitter identifier	Signal intensity	TIC variation	AGC Target
14.09 5 µm ID1	10 ⁷	20-70%	100%
14.09 5 µm ID2	5*10 ⁷	10-70%	100%
14.09 10 µm ID2	10 ⁷	20-50%	100%
14.09 10 µm ID3	5*10 ⁶	90%	100%
14.09 10 µm ID4	10 ⁶ -10 ⁷	15-20%	100%
04.10 5 µm ID1	2*10 ⁷	7-12%	100%
04.10 5 µm ID2	2*10 ⁸	4-6%	100%
04.10 5 µm ID3	10 ⁸	4-20%	100%
04.10 5 µm ID4	6*10 ⁷	6-11%	100%
04.10 5 µm ID5	2*10 ⁷	25-40%	100%
04.10 10 µm ID1	2*10 ⁷	10-20%	100%
04.10 10 µm ID2	3*10 ⁷	10-20%	100%
04.10 10 µm ID3	2*10 ⁷	5-30%	100%
04.10 10 µm ID5	10 ⁷	15-40%	100%

7.9 Analysis of higher concentration phosphatidylglycerol solutions using the commercial heated electrospray ionization source

Analyses of four PG solutions were done using HESI direct infusion. Their spectra are given in **Figure 52**, **Figure 53**, and **Figure 54**.

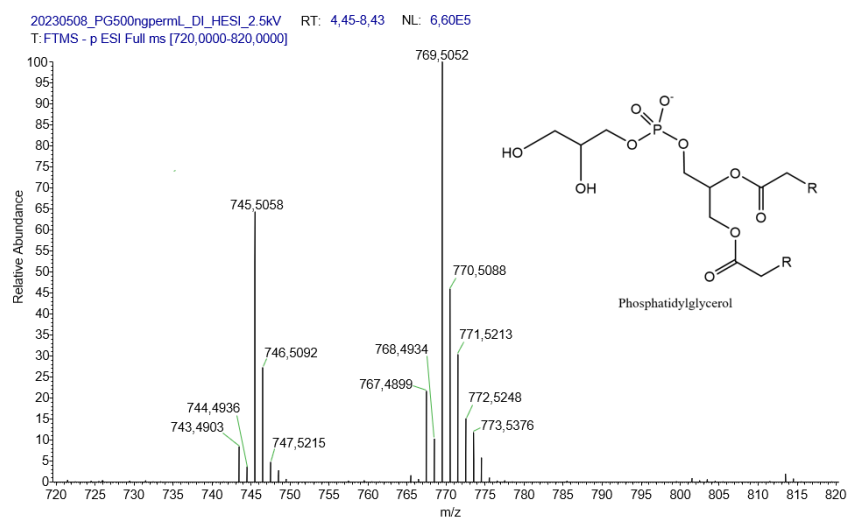


Figure 52. Mass spectrum of a 500 ng/mL PG solution.

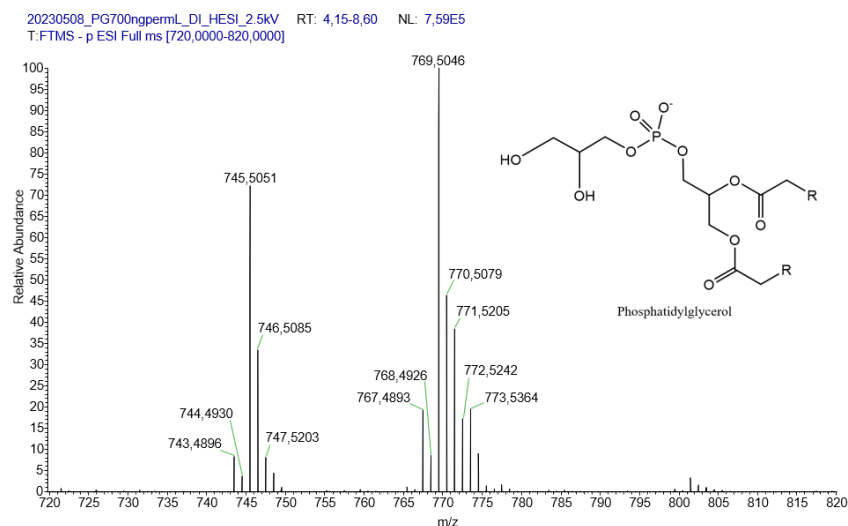


Figure 53. The mass spectrum of a 700 ng/mL solution.

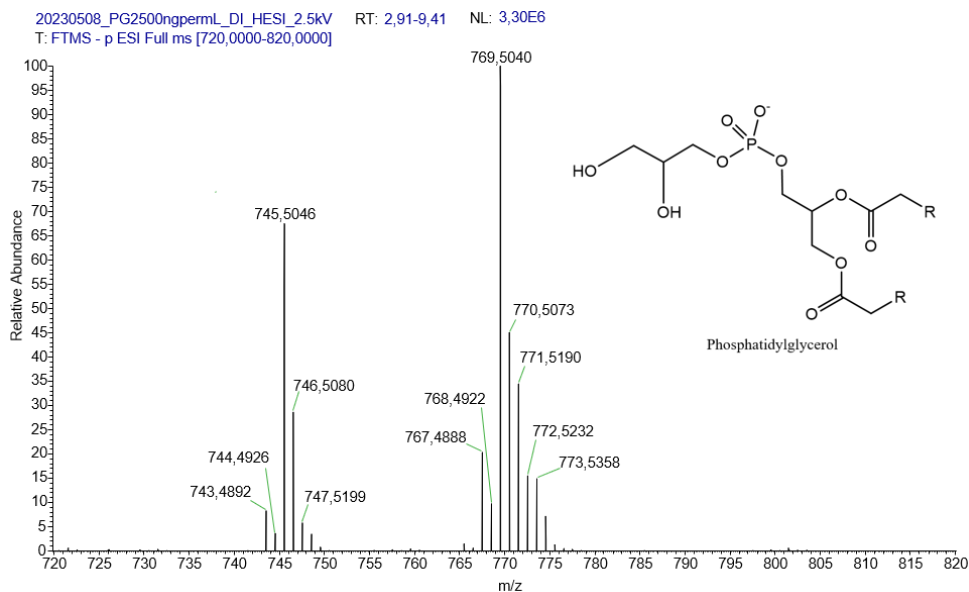


Figure 54. The mass spectrum of a 2500 ng/mL solution.

These four spectra are almost exact copies except for their peak intensities. The increasing base peak intensity increases proportionally with concentration, in the relationship given in **Figure 55**.

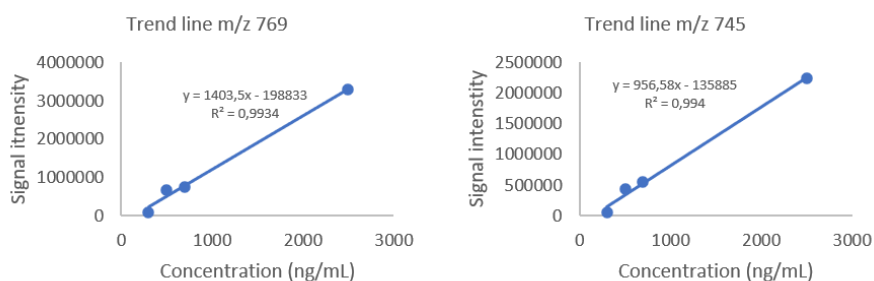


Figure 55. The figure shows the correlation of the signal intensity of two chosen ions across the different concentrations. The analyses show a consistent relationship with good linearity. **Left:** PG(18:2/18:2), **right:** PG(16:0/18:2).

7.10 Gastruloids were analyzed using MALDI imaging

The chemicals used in this section are carboxymethyl cellulose (2%) and 2,5-dihydroxybenzoic acid. The analyses were done in a different lab, and due to summer holiday, the exact purity, manufacturer, and supplier was not obtained.

Gastruloids were analyzed as a complementary experiment by MALDI imaging, to establish the expected results when using the nano DESI-MS at a later point. The cells were fixed in blocks of 2% carboxymethyl cellulose and cut to 10 μm thick slides using a Leica CM1860UV cryostat, dried in the cryostat chamber at $-20\text{ }^{\circ}\text{C}$, further dried for five minutes in a dessicator chamber for five minutes, and then sealed using food vacuum sealers. The cells were stored at $-20\text{ }^{\circ}\text{C}$ until analysis.

For application of the MALDI matrix, a HTX M3+ sprayer was used. Ten layers of spray using 20 mg/mL DHB in 70% methanol, 0.1% TFA were laid. The parameters used are given in **Table 24**.

Table 24. The table provides the parameters and their numerical value used in application of MALDI matrix on gastruloids samples.

Parameter	Value
Spray temperature	85 $^{\circ}\text{C}$
Number of layers	10
Solvent flow rate	110 $\mu\text{L}/\text{min}$
Spray nozzle velocity	1200 mm/min
Track spacing	3 mm
Spray movement pattern	CC
Pressure	10 psi
Gas flow rate	3 L/min
Drying time	0 min
Nozzle Ht	40 mm

A TIMS-TOF flex from Bruker instruments were used to do the imaging. Acquisition was done in positive mode.

Images were acquired for 18 different analytes from a single gastruloids. The images are shown in **Figure 56**.

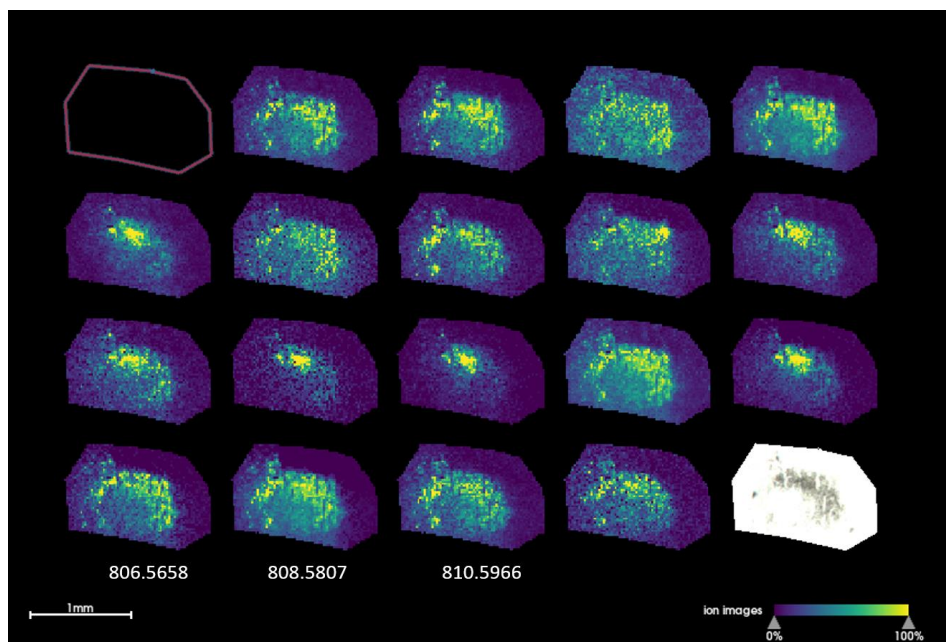


Figure 56. The figure shows the molecular images for 18 different analytes obtained after MALDI imaging. Their localization and quantitative occurrence are variable, and different regions display diverse abundance.

One of the analytes found had m/z -value 808.5807. This corresponds to the $[M+H]^+$ protonated specie of PC(38:5) with a -5.42 ppm mass accuracy value, which is acceptable for this MS technique. **Figure 57** shows a closer look at the distribution of this analyte, as well as its mass spectrum peak.

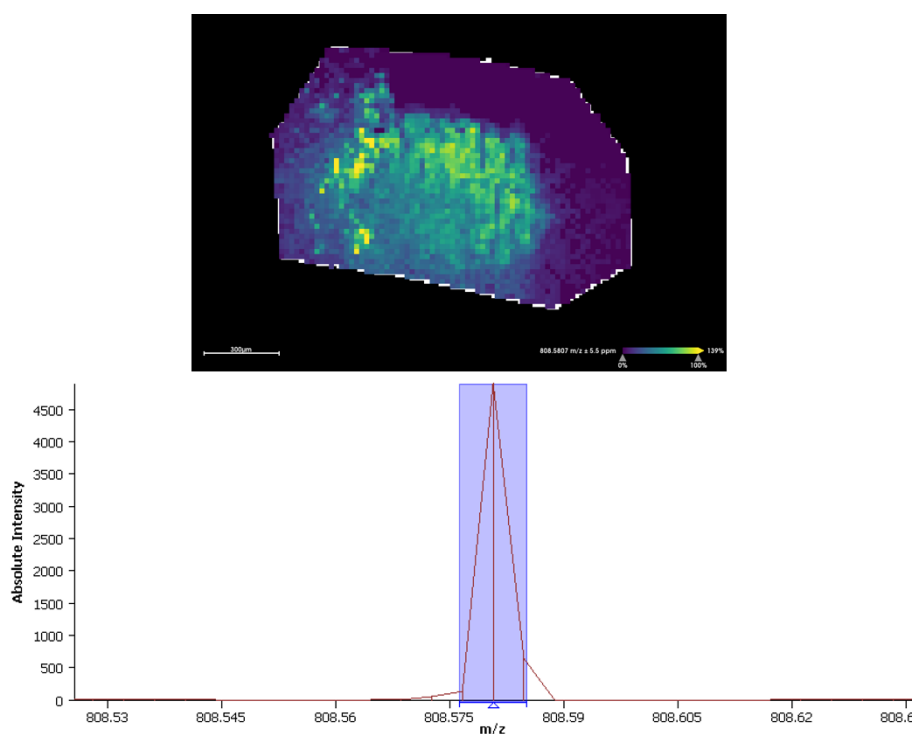


Figure 57. The spatial distribution of the $[M+H]^+$ ion of PC(38:4) in a gastruloids. Imaging was done using MALDI-TOF.

Of other analytes of interest found were the $[M+H]^+$ of PC(38:4) at m/z 810.5966 (-5.10 ppm), as well as the $[M+H]^+$ of PC(38:6) at m/z 806.5658 (-4.50 ppm). However, these two other PC compounds were at only 37% and 13% of the abundance of PC(38:5), respectively.